THESIS

FREQUENCY DIVERSITY WIDEBAND DIGITAL RECEIVER AND SIGNAL PROCESSOR FOR SOLID-STATE DUAL-POLARIMETRIC WEATHER RADARS

Submitted by

Kumar Vijay Mishra

Department of Electrical and Computer Engineering

In partial fulfillment of the requirements

for the Degree of Master of Science

Colorado State University

Fort Collins, Colorado

Summer 2012

Master's Committee:

Advisor: Chandrasekar V. Chandra

Anura P. Jayasumana

Paul W. Mielke Jr.

ABSTRACT

FREQUENCY DIVERSITY WIDEBAND DIGITAL RECEIVER AND SIGNAL PROCESSOR FOR SOLID-STATE DUAL-POLARIMETRIC WEATHER RADARS

The recent spate in the use of solid-state transmitters for weather radar systems has unexceptionably revolutionized the research in meteorology. The solid-state transmitters allow transmission of low peak powers without losing the radar range resolution by allowing the use of pulse compression waveforms. In this research, a novel frequency-diversity wideband waveform is proposed and realized to extenuate the low sensitivity of solid-state radars and mitigate the blind range problem tied with the longer pulse compression waveforms. The latest developments in the computing landscape have permitted the design of wideband digital receivers which can process this novel waveform on Field Programmable Gate Array (FPGA) chips.

In terms of signal processing, wideband systems are generally characterized by the fact that the bandwidth of the signal of interest is comparable to the sampled bandwidth; that is, a band of frequencies must be selected and filtered out from a comparable spectral window in which the signal might occur. The development of such a wideband digital receiver opens a window for exciting research opportunities for improved estimation of precipitation measurements for higher frequency systems such as X, Ku and Ka bands, satellite-borne radars and other solid-state ground-based radars.

This research describes various unique challenges associated with the design of a multi-channel wideband receiver. The receiver consists of twelve channels which simultaneously downconvert and filter the digitized intermediate-frequency (IF) signal for radar data processing. The product processing for the multi-channel digital

receiver mandates a software and network architecture which provides for generating and archiving a single meteorological product profile culled from multi-pulse profiles at an increased data date. The multi-channel digital receiver also continuously samples the transmit pulse for calibration of radar receiver gain and transmit power.

The multi-channel digital receiver has been successfully deployed as a key component in the recently developed National Aeronautical and Space Administration (NASA) Global Precipitation Measurement (GPM) Dual-Frequency Dual-Polarization Doppler Radar (D3R). The D3R is the principal ground validation instrument for the precipitation measurements of the Dual Precipitation Radar (DPR) onboard the GPM Core Observatory satellite scheduled for launch in 2014. The D3R system employs two broadly separated frequencies at Ku- and Ka-bands that together make measurements for precipitation types which need higher sensitivity such as light rain, drizzle and snow. This research describes unique design space to configure the digital receiver for D3R at several processing levels. At length, this research presents analysis and results obtained by employing the multi-carrier waveforms for D3R during the 2012 GPM Cold-Season Precipitation Experiment (GCPEx) campaign in Canada.

ACKNOWLEDGEMENTS

My debts are manifold and various: first, Colorado State University which provided a serene environment conducive to my research and studies. I am sincerely grateful to my thesis advisor Dr V. Chandrasekar for introducing me to radar meteorology and entrusting me with an opportunity to work in D3R project. I am thankful to Dr Anura Jayasumana and Dr Paul Mielke Jr. for their role as members of my defense examination committee.

I wish to thank Mathew Schwaller, Project Manager, NASA Goddard Space Flight Center for his continuous appreciation of my engagements in the project. A special note of thanks goes to Patrick Kennedy and David Brunkow of CSU-CHILL National Weather Radar Facility for their kind help during various stages of my graduate program. I also greatly appreciate the generous support I received from all the former and current members of the CSU Radar and Communication Lab.

A bit of fragrance always clings to the hand that gives the rose. I, therefore, also owe it to my mentors and colleagues in the great institutions where I have studied and worked in the past: my undergraduate alma mater National Institute of Technology (NIT), Hamirpur and my former research lab Electronics and Radar Development Establishment (LRDE), Defence Research and Development Organization (DRDO), Bangalore.

I am indebted to my family for their love and unconditional support during my stay at Colorado State University. This work is my tribute to the great sacrifices they made to ensure my success.

Jehi keṃ jehi para satya sanehū| So tehi milai na kachu saṃdehū||

("One accomplishes without doubt what one holds a true committment for.")

Tulasīdāsa, *Śrīrāmacaritamānasa* (Bāla Kāṇḍa, 259:3)

DEDICATION

To my Mom Shraddha Mishra, brothers Kumar Digvijay Mishra and Kumar Jay Mishra and the memories of my Grandma Rajrani Dubey and Dad Shyam Bihari Mishra

TABLE OF CONTENTS

LIST OF FIGURES

LIST OF TABLES

CHAPTER 1

INTRODUCTION

> *"See how that one little cloud floats like a pink feather from some gigantic flamingo. Now the red rim of the sun pushes itself over the London cloud-bank."* (Sherlock Holmes, *The Sign of Four* [Doyle, 1986])

The understanding of climate and precipitation structures has a profound influence and long tradition in several walks of science, economy, public policy and human culture. The practice of classifying clouds in discernible regimes and analyzing their respective properties has been employed by scientists, artists, philosophers and writers for centuries (Stephens, 2003). This is one way to observe and study precipitation.

The other method - technologically advanced and more accurate - is remote sensing by meteorological radars. This chapter gives an overview of the context of this thesis in weather radars.

1.1 Context of solid-state transmitters in weather radars

Over the last two decades, weather radar has proven to be a greatly valuable technology in remotely sensing the three-dimensional structure of precipitation, real-time monitoring and quantitatively estimating critical meteorological variables such as rainfall on a spatiotemporal scale and understanding the evolution of mesoscale phenomena such as clouds, tornadoes and floods (Bringi and Hendry, 1990; Doviak and Zrnić, 1993; Bringi and Chandrasekar, 2001; Cifelli and Chandrasekar, 2010).

The use of radars to detect weather returns originated soon after the end of Second World War when weather was identified as clutter for military radar applications (Atlas and Ulbrich, 1990). The suggestions to obtain meaningful meteorological data from the backscatter emanated in 1970s (Ulbrich and Atlas, 1975). During the early-to-mid 1990s, the operational deployment of 160 scanning ground-based S-band Weather Surveillance Radars -1988 Doppler (WSR-88D) across the United States revolutionized the meteorological observation and forecasting (Klazura and Imy, 1993). Apart from these scanning weather radars, in the mid-1990s the U.S. Department of Energy (DOE) Atmospheric Radiation Measurement (ARM) program deployed vertically pointing 35-GHz Doppler radars as an important tool to continuously monitor and study all radiatively important clouds at several climatologically distinct locations (Ackerman and Stokes, 2003; Kollias et al., 2007). In 1997, with the launch of Tropical Rainfall Measuring Mission (TRMM) satellite, weather radars were successfully introduced to space-borne platforms enabling the global observation of precipitation (Kummerow et al., 2000). Since mid-seventies up to mid-eighties, a period of rapid advances in radar polarimetry occurred leading to use of polarization diversity in weather radars (Seliga and Bringi, 1976, 1978; Seliga et al., 1990). The measurement of differential reflectivity in rainfall and its theoretical range was first shown conclusively using data from University of Chicago/Illinois State Water Survey (CHILL) radar (Seliga et al., 1979). Recently, the application and deployment of dual-polarization radars have transitioned from research domain to operational environments with the ongoing upgrade of Next Generation Weather Radar (NEXRAD) systems to dual-polarization capabilities.

Beginning with the centimeter-wavelength (S- and C-bands) scanning radars, the remote sensing of precipitation has gradually moved to the attenuating frequencies (X- and Ku-bands) and millimeter wavelengths (Ka- and W-bands). As demonstrated by the recent introduction of the Center for Collaborative Adaptive Sensing of the Atmosphere (CASA) Integrated Project 1(IP1), the network of X-band of radars

is more economically feasible and operationally useful for distributive collaborative sensing (Chandrasekar and Jayasumana, 2001). For radars with the same resolution volume and transmitted power, as the operating wavelength gets in the millimeter range, the radar is capable of detecting smaller cloud particles (Lhermitte, 1987). These two physical realities - attenuation at high frequencies and better detection of micro-structure of precipitation at millimeter wavelengths - mandate novel engineering realizations in weather radar systems.

One of the significant and recent hardware developments in weather radar systems has been the increasing use of solid-state transmitters, relatively uncommon in long-range weather radars. The lower peak-power of higher duty cycle solid-state transmitters makes them an attractive option for short-range, urban-restricted and space-borne weather radars. Coupled with higher reliability, extremely wide bandwidth and digital control, the higher procurement initial of the solid-state transmitters far outweighs the economical and operational benefits realized over its longer lifetime (Skolnik, 1990, 5.1-33). However, the usage of solid state transmitters precipitates innovations in waveform diversity and design (Chandrasekar and Bharadwaj, 2010) along with implementation of a new generation of weather radar receivers. This chapter describes the foundations and the challenges of this problem.

1.2 Signal theory of weather radar

The principle of a ground-based scanning weather radar is to transmit the electromagnetic waves at a wavelength λ of near-constant power P_t in very short pulses of width T_0, concentrated into a narrow beam defined by its radiating antenna, at predetermined azimuthal and elevation angles at periodic intervals of pulse repetition time (PRT) T_s. As each transmit pulse travels away from the radar, the returned voltage $V_r(t)$ at time t of the electromagnetic waves backscattered from the targets within the sampling volume is measured by the radar. The difference between the times of transmitted and received pulses can be translated into distance or range to

map the returned echo within the three-dimensional space comprising all sampling volumes (Doviak and Zrnić, 1993, p. 64).

1.2.1 Received signal and its statistics

In radar meteorology, the weather signals are defined as the composite of echoes from individual scatterers. These individual echoes constructively or destructively to produce a complex composite phasor sample. The received voltage can, therefore, be expressed as (Bringi and Chandrasekar, 2001, p. 221)

$$V_r(t) = \sum_k A_k(\tau; t) e^{-j2\pi f_0 \tau_k} U_{tr}(t - \tau_k) \tag{1.1}$$

where A_k is the scattering amplitude of the kth particle at range $r_k = c\tau_k/2$, $f_0 = c/\lambda$ is the frequency of the radar, c is the speed of light and U_{tr} is the transmitted waveform. Further, the complex voltage sample can be expressed in terms of two real information-bearing signals as $V_r(t) = I(t) + jQ(t)$, where I(t) and Q(t) are the in-phase and quadrature(-phase) components. The term "quadrature component" refers to the fact that it is in phase quadrature ($+\pi/2$) with respect to the in-phase component (Scherier and Scharf, 2010, p. 9).

The range r_k of the independent scatterer being random, $V_r(t)$ is a complex sum of independent random variables. The central limit theorem (Papoulis and Pillai, 2002) applies since, for the hydrometeor echoes, the number of scatterers is large and none of the variables is dominant. Therefore, the samples of V_r form a Gaussian distribution with zero mean. If $V_1, V_2, \cdots, V_N$ form a set of N complex received voltage samples corresponding to N consecutive transmitted pulses, then the probability density function of the signal vector $\mathbf{V} = [V_1 \;\; V_2 \;\; \cdots \;\; V_N]$ is a circular (Fjørtoft and Lopès, 2001) or proper (Scherier and Scharf, 2010, p. 53) complex Gaussian distribution with zero mean:

$$p(\mathbf{V}) = \frac{1}{\pi^N |\mathbf{R}_{vv}|} \exp(-\mathbf{V}^H \mathbf{R}_{vv}^{-1} \mathbf{V}) \tag{1.2}$$

where $\mathbf{R}_{vv}$ is the $N \times N$ complex covariance matrix corresponding to the signal vector $\mathbf{V}$. Since the I and Q components are independent Gaussian random variables, it follows that the amplitude $|V| = (I^2 + Q^2)^{1/2}$ is Rayleigh distributed while the phase $\theta = \tan^{-1}\left(\frac{Q}{I}\right)$ has a uniform distribution:

$$p(|V|) = \frac{|V|}{\sigma^2} \exp\left(-\frac{|V|^2}{2\sigma^2}\right) \tag{1.3}$$

$$p(\theta) = \frac{1}{2\pi} \tag{1.4}$$

where σ^2 is the mean square value of I (equal to that of Q). Since the power P is proportional to $I^2 + Q^2$, it follows that P is exponentially distributed with a mean value $\bar{P} = E(P) = E(|V|^2) = 2\sigma^2$:

$$p(P) = \frac{1}{2\sigma^2} \exp\left(-\frac{P}{2\sigma^2}\right) \tag{1.5}$$

1.2.2 Weather radar equation

Apart from the precipitation and clouds, meteorological radars respond to a wide variety of scattering targets including insects and birds, smoke and aerosol particles, refractive index variations, chaff and ground targets. Probert-Jones (1962) derived the weather radar equation for precipitation scattering which relates the average received power $\bar{P}_r$ (W) to the transmitted power P_t (W) as a function of the range r_0 (m) of the scatterer:

$$\bar{P}_r(r_0) = \left(\frac{cT_0}{2}\right)\left[\frac{P_t G_0^2}{\lambda^2 (4\pi)^3}\right]\left[\frac{\pi\theta_1\phi_1}{8\ln 2}\right]\frac{\pi^5 |K_p|^2 Z_e(r_0)}{r_0^2} \tag{1.6}$$

where G_0 denotes the peak antenna gain (dimensionless), θ_1 and ϕ_1 are the conventional half-power beam widths (rad), T_0 is the pulse width (m) and λ is the wavelength of the radar (m). K_p is the complex dielectric factor (dimensionless) of the target (conventionally, water) so that $|K_p|^2 = |(\varepsilon_r - 1)/(\varepsilon_r + 2)|^2$ where ε_r is the relative permittivity. Z_e is the equivalent reflectivity factor ($\mathrm{mm^6 m^{-3}}$) defined as

$$Z_e(r_0) = \frac{\lambda^4}{\pi^5 |K_p|^2}\eta(r_0) \tag{1.7}$$

where η is the back-scatter cross-section per unit volume (m^2m^{-3}).

In arriving at equation 1.6, it is assumed that the targets are Rayleigh scatterers that completely and uniformly fill the resolution volume. Further, the beam is Gaussian-shaped and multiple scattering is ignored. This equation also ignores the attenuation of the signal as it propagates through gases, particles and precipitation as is usually observed in radars operating at X-band and, to a lesser extent, C-band. However, the effect of attenuation can be incorporated in equation 1.6 by multiplying Z_e with an attenuation factor. The equivalent reflectivity factor Z_e is, by definition, proportional to the 6th moment of the raindrop diameter:

$$Z_e = \int_0^\infty N(D) D^6 dD \tag{1.8}$$

where $N(D)$ ($mm^{-1}m^{-3}$) denotes the raindrop size distribution (DSD) in a unit volume (m^3) and D is the diameter of the raindrop (mm). Rainfall rate R (mm/h) being proportional the raindrop size, forms an empirical relationship with Z_e. The measurement of the received power P_r in weather radar, therefore, is key to extract provide useful meteorological information.

From equation 1.6, if $\bar{P}_{ref}$ (dBm) is the received power at the reference antenna port and R (km) is the radar range to the resolution volume of the observation, then equivalent reflectivity factor Z_e (dBZ) is given by,

$$Z_e = \bar{P}_{ref} + C + 20 \log_{10} R \tag{1.9}$$

where C (dB) is the radar constant given by (Bringi and Chandrasekar, 2001, p. 334)

$$C = 10 \log_{10} \left\{ \frac{1}{\pi^5 |K_p|^2} \left(\frac{2}{cT_0} \right) \left[\frac{4\pi^3 l_{wg}^2}{P_t G_0^2} \right] \left(\frac{8 \ln 2}{\pi \theta_1 \phi_1} \right) \lambda^2 10^{21} \right\} \tag{1.10}$$

where l_{wg} is the waveguide loss to compensate measurement at the reference plane. The minimum detectable reflectivity Z_{min} (dBZ) at a particular range is usually defined for signal-to-noise ratio (SNR) of 0 dB. Therefore, the sensitivity of the radar is measured in terms of Z_{min}.

Table 1.1: Polarization algebra

Polarization state	Jones vector[a]	Stokes vector
Horizontal linear	[1, 0]	[1, 1, 0, 0]
Vertical linear	[0, 1]	[1, -1, 0, 0]
Linear at 45°	$[\frac{1}{2}, \frac{1}{2}]$	[1, 0, 1, 0]
Right-hand (CW) circular	$[\frac{1}{2}, \frac{-j}{2}]$	[1, 0, 0, -1]
Left-hand (CCW) circular	$[\frac{1}{2}, \frac{j}{2}]$	[1, 0, 0, 1]

[a] Jones vectors cannot describe partially polarized or unpolarized signals.

1.2.3 Scattering polarimetry

In contrast to conventional meteorological radars, the polarization diversity systems provide either for the variation of one or both of transmitted and received wave polarizations, or provide for dual-channel reception of orthogonally polarized waves. These polarimetric techniques permit measurement of additional precipitation echo characteristics such as mean values and distributions of size, shape, spatial orientation and thermodynamic phase state of the scatterers.

Wave polarimetry descriptors

There are several descriptors of wave polarimetry (Cloude, 2010). As the electric field evolves in three-dimensional space and time, it traces out a geometrical structure. If we look at the time variation of this structure in a fixed plan transverse to the direction of propagation and, without the loss of generality restrict attention to harmonic plane waves, then this locus is always elliptical. The sense of this polarization ellipse can be described in complex domain by Jones vectors for the completely polarized waves (such as in the case of deterministic scattering from hard targets). The polarization algebra which describes the effect of optical elements on polarization for completely polarized waves by manipulating Jones vectors using complex-values 2×2 Jones matrices is called Jones calculus (Scherier and Scharf, 2010, p. 214). The partially polarized or unpolarized waves (in case of random scattering by precipitation) are described by real-valued Stokes vectors. In 1892, Poincaŕe introduced a

spherical visualization of the different states of polarization with the representation of equator as linear polarization, the North Pole as the right-circular polarization and the South pole as left-circular polarization. The Stokes parameters are the Cartesian coordinates of the points on the sphere or, alternatively, of the parameters of the polarization ellipse. The analog calculus for the manipulation of Stokes vectors using real-valued 4×4 matrix is called the Mueller calculus (Scherier and Scharf, 2010, p. 214). Table 1.1 shows how Jones and Stokes vectors are alternate forms of wave polarimetric descriptors.

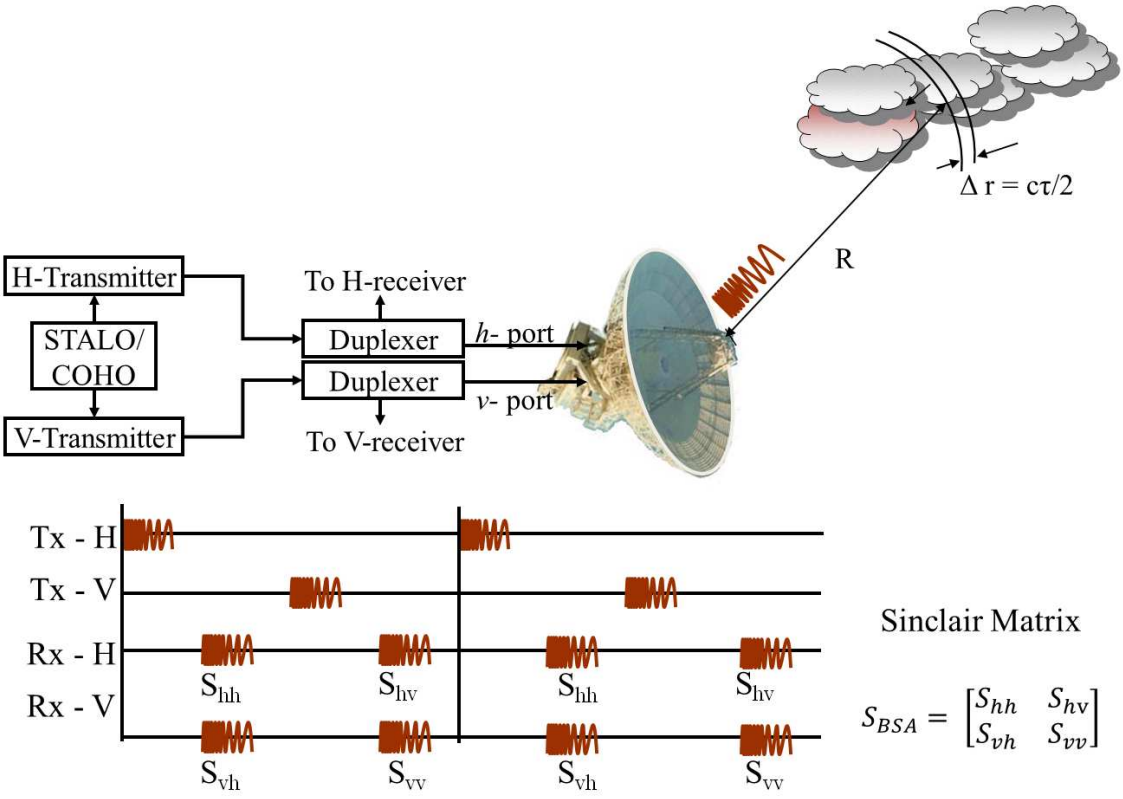

Figure 1.1: Dual-polarized antenna with two ports fed by two separate transmitters synchronized using STAble Local Oscillator (STALO) or COHerent Oscillator (COHO). The sequence of alternate transmission depicts the scattering polarimetry.

The scattering polarimetry i.e., the relationship between the incident wave and response of the target to the electromagnetic excitation, is described through the scattering matrix representation. Sinclair matrix relates the scattered wave fields to the incident wave fields. In the radar community, the early application of matrix algebra

to scattering is due to Edward Kennaugh (Cloude, 2010, p. 2). In radar and antenna studies, the Sinclair matrix (Figure 1.1) is described in backscatter alignment or BSA system as $\mathbf{S}_{BSA}$.

Transmission matrix and radar range equation

Apart from the backscatter matrix description of the target, the other radar polarimetry concept is based on the network theory and depends on the polarization transformation properties of the receiving antenna. The voltage induced in the horizontal h and vertical (v) ports radar antenna by the back scattered wave can be described in terms of the transmission matrix $\mathbf{T}$ in linear polarization basis as (Bringi and Chandrasekar, 2001, p. 178),

$$\begin{bmatrix} V_h \\ V_v \end{bmatrix} = \frac{\lambda G}{4\pi r^2}[\mathbf{T}][\mathbf{S}_{BSA}][\mathbf{T}] \begin{bmatrix} M_h \\ M_v \end{bmatrix} \tag{1.11}$$

where

$$\mathbf{S}_{BSA} = \begin{bmatrix} S_{hh} & S_{hv} \\ S_{vh} & S_{vv} \end{bmatrix}, \tag{1.12}$$

r is the propagation path distance to the fixed scatterer,

G is the antenna gain (assumed to be same for both horizontal and vertical polarization ports), and

$\mathbf{M} = \begin{bmatrix} M_h & M_v \end{bmatrix}^T$ represents the state of transmit polarization ($[M_h = 1,\, M_v = 0]$ for horizontal and $[M_h = 0,\, M_v = 1]$ for vertical polarization).

Covariance and coherency matrices

Corresponding to the two states of polarization as given by $\mathbf{M}$, the received voltage is a vector of four random variables:

$$\mathbf{v} = \begin{bmatrix} v_{hh} & v_{hv} & v_{vh} & v_{vv} \end{bmatrix} \tag{1.13}$$

where the subscript hv denotes vertical transmit state and horizontal receive state and so forth. The statistical properties of this random vector are expressed by its

covariance matrix:

$$E(\mathbf{v}\mathbf{v}^H) = E\begin{bmatrix} |v_{hh}|^2 & v_{hh}v_{hv}^* & v_{hh}v_{vh}^* & v_{hh}v_{vv}^* \\ v_{hv}v_{hh}^* & |v_{hv}|^2 & v_{hv}v_{vh}^* & v_{hv}v_{vv}^* \\ v_{vh}v_{hh}^* & v_{vh}v_{hv}^* & |v_{vh}|^2 & v_{vh}v_{vv}^* \\ v_{vv}v_{hh}^* & v_{vv}v_{hv}^* & v_{vv}v_{vh}^* & |v_{vv}|^2 \end{bmatrix} \tag{1.14}$$

This vectorial formulation of voltage measurements can also be expressed in terms of two other scattering vectors: Pauli scattering vector $\underline{\mathbf{k}}$ and Lexicographic scattering vector $\underline{\mathbf{\Omega}}$ (Lee and Pottier, 2009). While $\underline{k}$ representation is closely related to the physical properties of the scatterer $\underline{\Omega}$ is directly related to the system measurables.

$$\underline{\mathbf{k}} = \frac{1}{\sqrt{2}}\begin{bmatrix} S_{hh} + S_{vv} & S_{hh} - S_{vv} & S_{hv} + S_{vh} & j(S_{hv} - S_{vh}) \end{bmatrix}^T \tag{1.15}$$

$$\underline{\mathbf{\Omega}} = \begin{bmatrix} S_{hh} & S_{hv} & S_{vh} & S_{vv} \end{bmatrix}^T \tag{1.16}$$

In case of backscattering from reciprocal scatterers, $S_{hv} = S_{vh}$ and the vectors can be represented as:

$$\underline{\mathbf{k}} = \frac{1}{\sqrt{2}}\begin{bmatrix} S_{hh} + S_{vv} & S_{hh} - S_{vv} & 2S_{hv} \end{bmatrix}^T \tag{1.17}$$

$$\underline{\mathbf{\Omega}} = \begin{bmatrix} S_{hh} & \sqrt{2}S_{hv} & S_{vv} \end{bmatrix}^T \tag{1.18}$$

The statistical description of partial scattering polarimetry can then be represented as either coherency matrix $\mathbf{J} = \underline{k}\cdot\underline{k}^H$ or the covariance matrix $\mathbf{\Sigma} = \underline{\Omega}\cdot\underline{\Omega}^H$. Coherence is a synonymous term for correlation coefficient, but, in the frequency domain, coherence is more commonly used than correlation coefficient (Scherier and Scharf, 2010, p. 211). However, radar observables are directly expressed in terms of the elements of the covariance matrix. For meteorological radars, since the individual scatterers are not only in relative motion but also fluctuate in the shape or orientation aspects, ensemble averaging should also be included in the statistical description. The backscatter covariance matrix is then given by (Bringi and Chandrasekar, 2001, p. 137),

$$\mathbf{\Sigma} = \left\langle \begin{bmatrix} |S_{hh}|^2 & \sqrt{2}S_{hh}S_{hv}^* & S_{hh}S_{vv}^* \\ \sqrt{2}S_{hv}S_{hh}^* & 2|S_{hv}|^2 & \sqrt{2}S_{hv}S_{vv}^* \\ S_{vv}S_{hh}^* & \sqrt{2}S_{vv}S_{hv}^* & |S_{vv}|^2 \end{bmatrix} \right\rangle \tag{1.19}$$

where the angle brackets denote ensemble averaging.

1.2.4 Dual-pol radar observables

For the dual-polarization radar systems, any arbitrary polarization state but they are usually either circular or linear. Though circular polarization has been used in the past for rainfall estimation and hydrometeor classification (Hendry and Antar, 1984), the linear horizontal and vertical polarizations have become prevalent recently. This is because the linear polarization states do not change as a function of propagation or, alternatively, they are the eigen polarization states of the precipitation medium for electromagnetic wave propagation (Bringi and Chandrasekar, 2001, p. 186). The dual-polarization system discussed here and later is therefore confined to linear polarization systems. Hence, references to radar observables like circular depolarization ratio (CDR) (Bringi and Chandrasekar, 2001, p. 112) have been avoided here.

Once all the elements of the backscatter covariance matrix have been estimated in a so-called fully polarimetric system, several radar observables, which provide useful information about hydrometeor size, shape orientation, spatial distribution and thermodynamic state, can be defined. Following are some of the common dual-polarization radar observables expressed in terms of the scattering matrix parameters. Chapter 5 discusses their physical meaning and computation from the measured data.

Copolar backscattering cross-section per unit volume ($\mathrm{m^2 m^{-3}}$):

$$\textbf{Horizontal}: \quad \eta_{hh} = \langle n4\pi |S_{hh}|^2 \rangle \tag{1.20}$$

$$\textbf{Vertical}: \quad \eta_{vv} = \langle n4\pi |S_{vv}|^2 \rangle \tag{1.21}$$

where n is the number concentration of the particles ($\mathrm{m^{-3}}$).

Cross-polar backscattering cross-section per unit volume ($\mathrm{m^2 m^{-3}}$):

$$\eta_{hv} = \langle n4\pi |S_{hv}|^2 \rangle \tag{1.22}$$

$$\eta_{vh} = \langle n4\pi |S_{vh}|^2 \rangle \tag{1.23}$$

$$\eta_{hv} = \eta_{vh} \text{ (Tragl, 1990)} \tag{1.24}$$

Copolar reflectivity ($\mathrm{mm^6 m^{-3}}$ or dBZ):

$$Z_h = \frac{\lambda^4}{\pi^5 |K_p|^2} \eta_{hh} \tag{1.25}$$

$$Z_v = \frac{\lambda^4}{\pi^5 |K_p|^2} \eta_{vv} \tag{1.26}$$

Cross-polar reflectivity ($\mathrm{mm^6 m^{-3}}$ or dBZ):

$$Z_{hv} = \frac{\lambda^4}{\pi^5 |K_p|^2} \eta_{hv} \tag{1.27}$$

$$Z_{vh} = \frac{\lambda^4}{\pi^5 |K_p|^2} \eta_{vh} \tag{1.28}$$

Differential reflectivity (dB):

$$Z_{dr} = 10 \log_{10} \left(\frac{\eta_{hh}}{\eta_{vv}} \right) \tag{1.29}$$

Linear depolarization ratio (dB):

$$LDR_{vh} = 10 \log_{10} \left(\frac{\eta_{vh}}{\eta_{hh}} \right) \tag{1.30}$$

$$LDR_{hv} = 10 \log_{10} \left(\frac{\eta_{hv}}{\eta_{vv}} \right) \tag{1.31}$$

Copolar correlation coefficient (dimensionless):

$$\rho_{co} = \frac{|\langle S_{hh} S_{vv}^* \rangle|}{\sqrt{\langle |S_{hh}|^2 |S_{vv}|^2 \rangle}} \tag{1.32}$$

Backscatter differential phase (°):

$$\delta = \angle(\langle S_{vv} S_{hh}^* \rangle) \tag{1.33}$$

Co-cross-polar correlation coefficient (dimensionless):

$$\rho_{cx}^h = \frac{|\langle S_{hh}^* S_{hv} \rangle|}{\sqrt{\langle |S_{hh}|^2 |S_{hv}|^2 \rangle}} \tag{1.34}$$

$$\rho_{cx}^v = \frac{|\langle S_{vv}^* S_{hv} \rangle|}{\sqrt{\langle |S_{vv}|^2 |S_{hv}|^2 \rangle}} \tag{1.35}$$

1.3 Aspects of solid-state weather radar systems

As remarked in Section 1.1, solid-state transmitters are increasingly being deployed in weather radars. Solid-state transmitters operate at much lower volatges compared to high-power klystrons, traveling-wave tubes (TWTs) and magnetrons. Apart from extremely wide bandwidth, they also offer better efficiency, longer operating life and higher reliability. Due to lower voltage operation, solid-state transmitters are also attractive for spaceborne, airborne and phased-array applications. However, the power output of individual solid-state devices is very limited which degrades the sensitivity of weather radars. This is because the sensitivity of a weather radar is inversely proportional to the product of the pulse width and peak power and directly proportional to the receiver bandwidth (equations 1.9-1.10). However, solid-state transmitters can be operated at high duty cycles compared to the conventional transmitters which generally requires the use of pulse-compression waveforms.

1.3.1 Pulse compression waveforms

Pulse compression processing is employed to increase the signal energy transmitted without increasing the peak transmit powers nor sacrificing the range resolution. These techniques divorce the useful signal bandwidth (and, thereby, range resolution) from the transmitted pulse length. The radar signal bandwidth to be transmitted is increased by modulating the signal within the transmitted pulse resulting in a *wideband* waveform. Target echo signals are then passed through filters matched to the transmitted signal and hence the echo energy is *compressed* into a pulse having the time duration τ_c, which is approximately equal to the reciprocal of the transmitted bandwidth B_t. The ratio of the transmitted to compressed pulse length is called the pulse compression ratio ρ

$$\rho = \frac{B_t}{\tau_t} = \frac{\tau_t}{\tau_c} \tag{1.36}$$

where τ_t is the transmitted pulse length.

The use of pulse compression leads to a few undesired consequences. The longer transmitted pulse compression waveform blinds the radar at short ranges and, therefore, a "fill-in" pulse(s) must also be transmitted and its returned echo must also be processed. Further, the compressor does not form only a single pulse in time but has undesired precursors and followers of reduced amplitude called range-time sidelobes. These sidelobes are objectionable since they may be mistaken as possible targets (Peebles, 1998, p. 287-289). Another advantage of solid-state transmitter design is

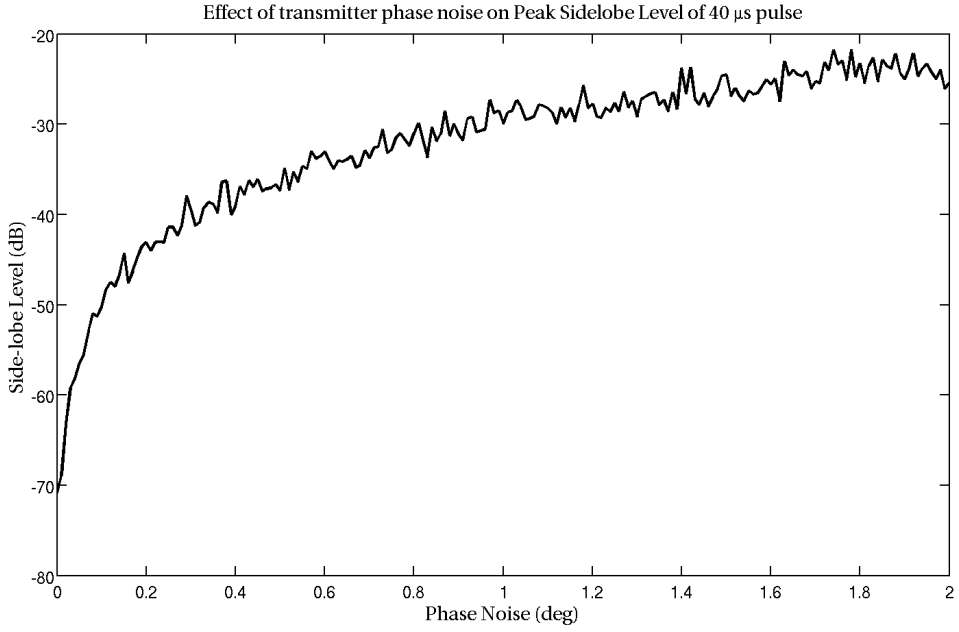

Figure 1.2: Peak sidelobe levels of the output of a pulse compression filter as a function of phase noise of the transmitter. The pulse compression waveform is a 3.6 MHz non-linear chirp of pulsewidth 45 μs. The filter design is based on the Lp-norm optimization.

low phase noise and high phase linearity. Phase noise is generated by the transient frequency variations in the COHO or STALO used in the transmitter stage. The stability in the oscillator outputs is desired in a fully coherent radar since this affects measurement of the phase-derived moments such as mean velocity and differential propagation phase. The effect of phase noise also decreases clutter suppression ratio

(CSR) provided by ground clutter filters. Also, the peak sidelobe level (PSL) of the pulse compression filter output is adversely affected because of phase noise as a result of increased mismatch (Figure 1.2).

Mitigation of blind range and range-velocity ambiguity

There are several ways to choose the sequence of transmitting the fill-in pulses. First, the transmission of short fill-in pulse and the long pulse can be alternated. This transmission scheme causes low maximum unambiguous velocity and longer dwell times (Skolnik, 1990). Another way is to transmit the short pulse, collect and process its return until the transmission of the long pulse (Lewis et al., 1986). This transmission scheme would, however, blank out the long range returns of the short pulse. To enable full-range processing of all the pulses, a frequency-diversity waveform can be transmitted where each pulse is transmitted one after the other at a slightly different frequency (Bharadwaj et al., 2009).

Range-time sidelobe suppression

For past few decades, pulse compression has been one of the common techniques successfully employed in hard target radars (Lewis et al., 1986) as well as lidars (Oliver, 1979), where the degrading effect of distributed clutter on range sidelobes has been well-documented (Nathanson, 1969, p. 67). The first use of pulse compression for atmospheric distributed targets was on the Arecibo ionospheric radar (Keeler and Passarelli, May 1989). The range sidelobes, being one of the major sources of error for estimating echoes from extended scatterers, limit the operational feasibility of pulse compression in weather radars (Mudukutore et al., 1998). One of the common design solutions to reduce the range sidelobes is to employ optimal modulating schemes such as nonlinear frequency modulation (NLFM) (Skolnik, 1990, 10.1-39). The compressor filter is then designed to minimize the integrated sidelobes (ISL) - a better measure for sidelobe contamination in the case of extended targets.

Implications of wider bandwidth

A third drawback of using pulse compression has been the unavailability of bandwidth. While research systems may not be constrained by a wider transmission bandwidth, the operational systems may not fit into the channelized frequency assignments. For example, the Ku-band Broadband Radar (BBR) designed by Osaka University, Japan employs pulse compression and has a maximum range of 15 km (Yoshikawa et al., 2010). The radar is intended for networked weather operation implying future deployment of several such radar systems. However, the radar has a bandwidth of 80 MHz which can be a potential problem in frequency assignments for several units of this radar. Further, wideband digital receivers which can simultaneously process data for a multi-pulse waveform at two polarizations would be computationally expensive.

1.3.2 Wideband digital receivers

Digital techniques have been used in radar systems for a long time (Galati, 1993, p. 515-519) (Tsui, 2001). Because of their ability to process high-speed data in real-time, programming flexibility and wider bandwidth of available analog-to-digital converters (ADCs), digital receivers are superseding the conventional analog receivers. A modern radar receiver now typically consists of both the analog and digital modules. Analog microwave components convert the received the Radio-Frequency signal from the antenna and translate it to the Intermediate-Frequency (IF). The digital receiver then digitizes this signal and processes it to provide a meaningful information to the user (Figure 1.3).

In terms of signal processing, the term *wideband* implies that the bandwidth of the signal of interest is comparable to the sampled bandwidth (Pace, 2000). In order to digitize signals in a wideband receiver, the ADCs must operate at a very high sampling speed. They must also have large number of bits to minimize quantization errors. Recent advances in ADC technology have made simultaneously achieving both these requirements possible (Tsui, 2001).

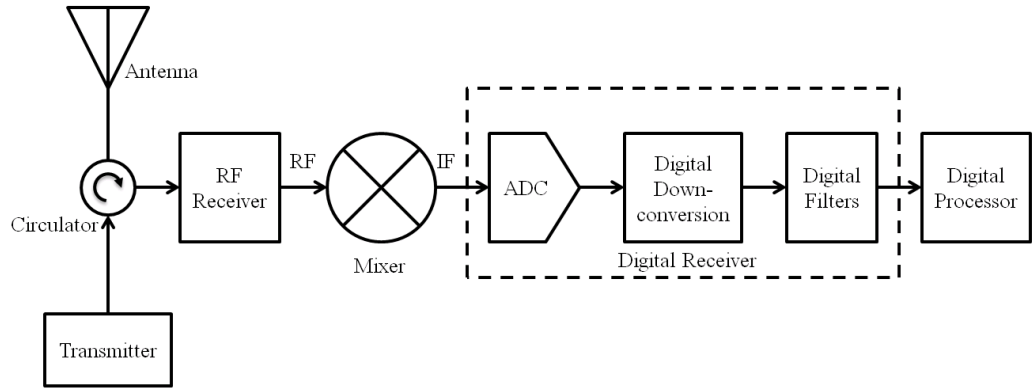

Figure 1.3: Context of a generic digital IF receiver in a radar system.

The high speed ADC outputs must be processed by high-speed digital circuits. In early designs of digital receivers, the downconversion of Intermediate-Frequency (IF) signal to I- and Q- channels was carried out prior to ADC sampling. However, the increased use of Field Programmable Gate Array (FPGA) technology has facilitated downconversion of the digitized IF signal as well as perform several advanced digital signal processing techniques on the the baseband signal. Digital downconversion completely eliminates image frequencies that result due to I/Q gain imbalances or imperfections in the hybrid circuits used in analog downconverters.

Digital IF receivers provide wide linear dynamic range without resorting to the use of complex and unweildy analog Automatic Gain Control (AGC) circuits. Several analog IF components can be eliminated and replaced by a programmable digital receiver thereby reducing the cost and real-estate. The remote monitoring of the received signal processing can now be extended to the IF level (Vaisala Inc., Sept 2009). For polarization diversity systems, two identical analog receiver channels can be replaced by a single digital receiver hardware.

1.3.3 Potential deployment of frequency-diverse waveforms

The frequency-diversity wideband waveforms for radars employing solid-state transmitters can avoid blind zones associated with pulse compression and still achieve

adequate sensitivity. These waveforms have been shown to be promising in theoretical simulations (Bharadwaj and Chandrasekar, 2012). Though these waveforms were conceptually proposed a while back (George et al., 2008), they were not realized or deployed on any radar system so far. This is because the transition from high peak-power transmitters to solid-state transmitters in an existing radar system is not seamless. Employing solid-state transmitters would require additional hardware and radical changes in several other existing subsystems chiefly a digital transmitter control, waveform generator, a wideband digital receiver and an enhanced moment processor. Further, the procurement initial for solid-state transmitters for the existing low-frequency S- and C-band radars is extremely high. The transition to solid-state transmitters in existing radar systems has therefore been more gradual than expected. Two solid-state transmitter radars with higher operational frequencies are now described which have been designed to use the frequency-diversity waveforms and a wideband digital receiver. Table 1.2 summarizes the parameters for waveform considerations for these two solid-state transmitter systems.

1.3.3.1 WiBEX

With the success of CASA network of X-band radars in providing rapid updates of hazardous weather, there has been tremendous interest in developing economically attractive X-band radars. Since 2008, Colorado State University has been developing a transportable, scanning, solid-state transmitter Wideband Experimental X-band (WiBEX) radar which is intended to be a test platform for various novel radar research waveforms (George et al., 2010). The radar employs dual 100W solid-state power amplifier modules, capable of 15% duty cycle, each driving the ports of a dual-polarization 2.4m X-band antenna. The transmitter is controlled by a programmable waveform and and timing generator which has been developed in-house.

Each sub-pulse of the frequency-diversity waveform requires approximately 10 MHz of bandwidth, including the guard band between sub-pulses. The digital baseband signal must, therefore, have a bandwidth greater than 30 MHz to accommodate

Table 1.2: Technical characteristics of the WiBEX and D3R systems

Parameter	**WiBEx**	**D3R**
Current status (Summer 2012)	Under development	Operational
Parabolic dual-polarized antenna		
Size	8ft/96in	6ft/72in (Ku) 28in (Ka)
Gain	44.5 dB	44.5 dB
3-dB Beamwidth	1 °	0.9 °
Dual-channel solid-state transmitter		
Peak power	100 W	200 W (Ku) 1 W (Ka)
Maximum duty cycle	15%	30%
Receiver		
RF central frequency	9.41 GHz (X)	13.91 GHz (Ku) 35.56 GHz (Ka)
Noise figure	2 dB	4.6 dB (Ku), 5.5 dB(Ka)
IF central frequency	140 MHz	140 MHz
1-dB Bandwidth	32 MHz	50 MHz
Minimum detectable signal	0 dBZ at 5 km	-10 dBZ at 15 km
Frequency-diversity waveform		
Long pulsewidth	45 μs	40 μs
Medium pulsewidth	20 μs	20 μs
Short pulsewidth	1 μs	1 μs

3 sub-pulses. The received signals from the antennas pass through the calibration switches and the Low Noise Amplifiers (LNAs). A single-conversion receiver, using a single-sideband downconvert mixer is used to shift the signals back to the 140 MHz IF.

The IF is digitized by the digital receiver ADCs for further processing. A multi-channel FPGA-based wideband receiver is designed for high configurability and flexibility in research. Based on the senstivity requirement and system parameters, a three-pulse frequency-diversity waveform has been employed in WiBEX radar. Figure 1.4 shows the complex envelope of the transmit pulse $g(t)$ and its spectrogram at a sampling frequency of 200 MHz. The corresponding sensitivity plot of this waveform is shown in Figure 1.5.

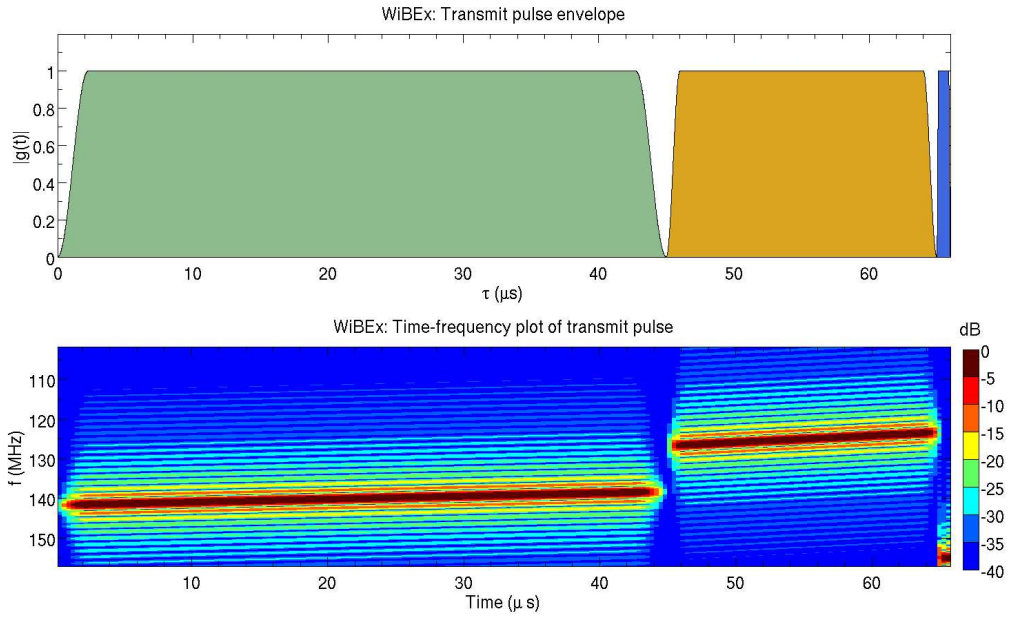

Figure 1.4: The transmit pulse envelope (top) and time-frequency plot (bottom) of the WiBEX waveform. 140 MHz is the central IF and the total pulsewidth is 66μs.

1.3.3.2 D3R

In 1997, the Ku-band weather radar on-board the TRMM satellite introduced advanced meteorological remote sensing via satellites. The National Aeronautical and

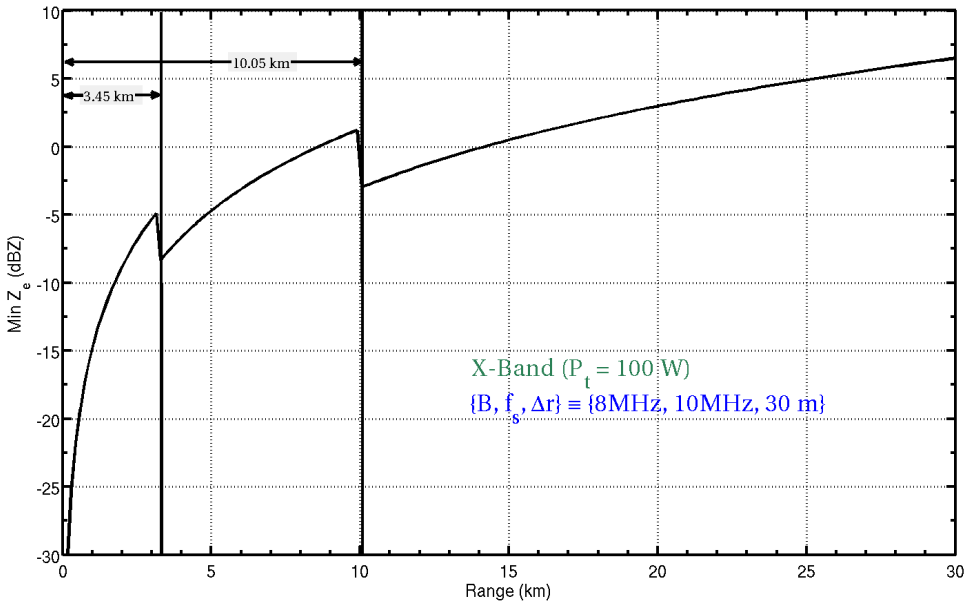

Figure 1.5: Minimum detectable reflectivity of the three-pulse WiBEX waveform.

Space Administration (NASA) Global Precipitation Measurement (GPM) satellite due to be launched in 2014 is the successor mission to TRMM. It plans to add even higher frequency (Ka-Band) to its on-board weather radar in order to obtain more accurate and detailed microphysical information. All satellite precipitation missions require ground validation radars which operate at identical frequencies (Chandrasekar et al., 2008). This is another potential application of solid-state transmitter and frequency-diversity waveforms. Since 2009, the ground validation radar for the GPM mission - Dual-frequency Dual-polarized Doppler Radar or D3R - has been developed as a collaboration among Colorado State University, NASA Goddard Space Flight Center (GSFC) and Remote Sensing Solutions (RSS) (Chandrasekar et al., 2010). The first generation D3R has two co-aligned separate Ku- and Ka-band antennas on a common pedestal with measured cross-polar isolation >-30 dB, pattern mismatch within 5% and Dual Frequency Ratio (DFR) error ≈ -0.5 dB. The radar employs solid-state transmitters to achieve higher sensitivity with lower peak transmit power and enhance system stability in extreme climatic conditions. A programmable multi-

channel pulse-compression digital receiver implements a novel multi-pulse frequency-diversity waveform (Figure 1.6) used in D3R to achieve sensitivity of -10 dBZ at 15 km (Figure 1.7) to enable snow measurements. The velocity requirement of 25 m/s is met with staggered PRT 2/3 scheme. Advanced attenuation correction algorithms are employed for highly attenuating frequencies (Ku-band: 13.91±25GHz, Ka-band: 35.56±25GHz). The real-time signal processor implements the time domain clutter suppression for non-uniform sampling. The radar is now operational and was successfully deployed in a field campaign during the winter of 2012. The wideband digital receiver was successfully realized for D3R and tested in the field deployment (Mishra et al., 2012). The D3R system is discussed in detail in Chapter 6.

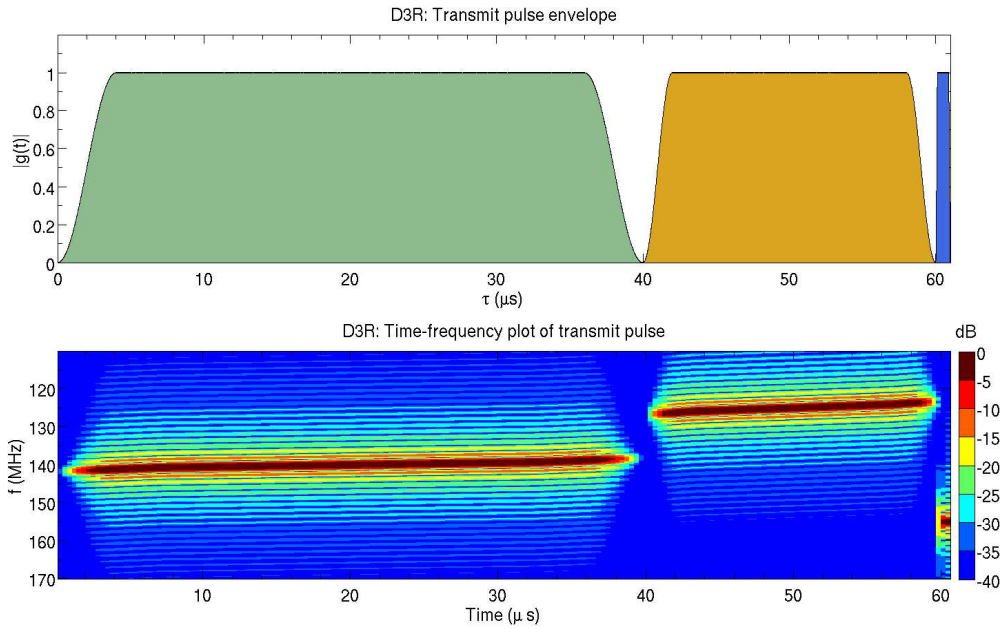

Figure 1.6: The transmit pulse envelope (top) and time-frequency plot (bottom) of the D3R waveform. 140 MHz is the central IF and the total pulsewidth is 61μs.

1.4 Thesis motivation

A wideband digital receiver would be ideal to process the pulse compression waveforms mentioned in Section 1.3.1 for solid-state weather radars. Apart from the

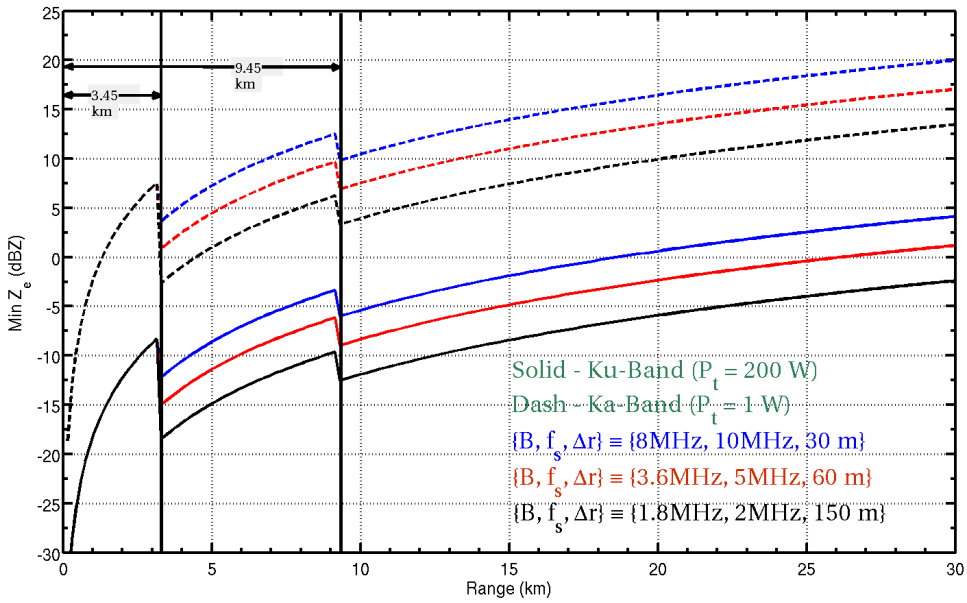

Figure 1.7: Minimum detectable reflectivity of the three-pulse D3R waveform.

benefits described before, such a receiver would be able to operate in a channelized architecture to enable processing of several subpulses and dual-polarizations. As the higher-frequency weather radar systems become more prevalent as spaceborne sensors, airborne radars, ground validation instruments, networked distributed collaborative systems and research platforms, wideband digital receivers would be integral to their development. These receivers would also be a general solution for the existing S- and C-band weather radars when upgraded to solid-state transmitters. There are, therefore, interesting opportunities in research and immense operational and performance benefit with the development of wideband digital IF receivers. This research focusses on the design, development and deployment of such a wideband digital receiver.

1.5 Organization of the thesis

The broad philosophy while organizing this research has been to first describe the general design and development of a wideband frequency diversity digital receiver for solid state weather radars. The thesis then demonstrates its experimental deploy-

ment for the NASA Dual-Polarized Dual-Frequency Doppler Radar (D3R) system as a special case. This chapter introduced the research problem which precipitates the need for developing such a receiver. Chapter 2 examines the existing digital receivers for weather radars. A review of common features of these products precedes their comparison. Chapter 3 presents the general digital receiver solution for solid-state transmitters. It specifies the requisite hardware architecture which has interfaces to the several important subsystems of a solid-state weather radar and is easily accessible for design and test to the developer. Subsequently, the principle of operation of the hardware both within the system and in stand-alone mode is introduced. Chapter 4 describes the design of FPGA-based multi-channel digital receiver while assessing multiple philosophies to achieve design goals. The software interface to configure and program the digital receiver is also included here. The networked environment wherein the output of the digital receiver is processed, archived and displayed is given in Chapter 5. The various processing modes and algorithms to produce scientifically useful products are given and their realization in a real-time system described. Chapter 6 describes the scientific objectives and engineering accomplishments of the D3R system. The waveform design for the radars is considered here within the realms of its specifications. Chapter 7 concludes the thesis by summarizing the results obtained through the first field deployment of the multi-channel digital receiver and signal processor on the D3R system.

CHAPTER 2

AN OVERVIEW OF EXISTING WEATHER RADAR DIGITAL IF RECEIVERS

Digital receivers for hard-target radars and communication systems have been commercially available for last three decades (Pace, 2000) (Tsui, 2001) (Galati, 1993). For weather radars, digital receivers and processors were not commercially available till late 1990s. Apart from several commercial solutions available today, many in-house research products have also been developed. This chapter describes some of the common requirements and features of weather radar IF receivers commonly used in magnetron and klystron-systems.

2.1 Common features

In past few years, The user demand to provide features in digital IF receivers which allow signal processing for improved data quality and enhanced operational ease has increased by several folds. All weather radar receivers typically include echo processing for signal transmitted under varied polarizations, waveforms and pulsing schemes. Most also provide varying degree of programmability (as in filters, IF sampling etc.) and can be remotely configured or accessed. It is customary that digital receivers are available as plugged-in modules for host computers (though there are exceptions as noted later). It should be noted that most of the existing commercially available digital IF receivers can not process frequency-diversity pulse compression processing for solid-state transmitter radars. Also, some features (such

as burst pulse tracking) are specific to magnetron-based systems only.

Wide dynamic range

The dynamic range of the receiver is closely related to the sensitivity of the receiver since sensitivity is the lower limit of the dynmaic range. The dynamic range for measuring the backscattered power from atmospheric targets is very large. This is so because, firstly, the effective backscatter cross-sections of atmospheric scatterers span dynamic ranges of approximately 60 dB for precipitation but much larger if cloud particles, clear air and ground target returns are included. Secondly, the dependence of the received power on the inverse of the range-squared for distributed targets spans a range of 50 dB between 1 and 300 km (Keeler and Passarelli, May 1989).

There are several techniques to increase the dynamic range of the digital receiver. The dynamic range is primarily decided by the choice of the ADC devices. To convert wideband signals of bandwidth f_{IN}, the sampling speed f_s of ADCs should be high. To digitize with low quantization error, the converter's number of bits b should also be large. The ADCs typically have a saturation level of P_{sat} dBm under which its operation is linear. Then, the lower limit of the dynamic range of the receiver expressed at bandwidth BW (typically, 1 MHz) is given by (Pace, 2000, p. 163-176),

$$DR_l(dB) = P_{sat} - 20\log_{10}(2^b) - 10\log_{10}\left(\frac{f_s/2}{BW}\right) \tag{2.1}$$

$$= P_{sat} - 6.02b - 10\log_{10}\left(\frac{f_s/2}{BW}\right) \tag{2.2}$$

Unfortunately, numerous factors degrade the ADC's ideal performance resulting in a lower SNR value and higher effective noise figure value. These factors include thermal noise, clock jitter (especially for higher input frequencies having high slew rates) and subranging errors. These errors are often represented by replacing b with the effective number of bits ($ENoB$) which is a lower number than b. When quantization noise is also taken into account, the lower limit of the dynamic range is given by (Pace, 2000,

p. 167),

$$DR_l(dB) = P_{sat} - 1.76 - 6.02(ENoB) - 10\log_{10}\left(\frac{f_s/2}{BW}\right) \tag{2.3}$$

The dynamic range itself is,

$$DR(dB) = P_{sat} - DR_l \tag{2.4}$$

Some receivers also employ additional techniques like the statistical large-signal linearization and coherent integration to increase the dynamic range by a few dB. However, many commercially available weather radar receivers employ a pair of converters for each signal to considerably improve the dynamic range. The primary (HiGain) and secondary (LoGain) ADCs with overlapping dynamic range have a nominal channel separation of tens of dBs (Vaisala Inc., Sept 2009).

Polarization agility

Polarization agility implies both H- and V- polarizations can be transmitted and received simultaneously. The backscatter matrix can be then determined from a single measurement. This is one of the most common modes of modern dual-pol weather radars where the digital receiver processes both the vertical and horizontal channels together. The signal processor computes standard moments and dual-pol moments like differential reflectivity Z_{dr}, correlation coefficient ρ_{hv} and differential phase Φ_{dp}.

Polarization diversity

Polarization diversity radar can transmit the two orthogonal polarizations alternately but receive both of them simultaneously. In this so-called "alternate mode", the typical additional output moments of the signal processor are LDR_h, LDR_v, LDR_{hv}, ρ_{cx}^h and ρ_{cx}^v (Bringi and Chandrasekar, 2001, p. 183). The backscatter matrix can only be determined in two successive measurements. This can lead to larger errors in measurements for the non-stationary targets with a correlation time shorter than the time of these two measurements, However, the most useful application of this mode

is to measure LDR which gives information about the thermodynamic state of the hydrometeor.

On-board transmit control

It is usually advisable to provide the waveform generator and transmit control in the same module as the digital receiver. This has advantages in better clock synchronization and less real-estate thereby eliminating separate board for the waveform generator. This, however, implies additional resources on the receiver board such as a bigger FPGA and digital-to-analog converters (DACs). For research radars, a greater degree of flexibility in modifying the transmit waveform is implicit to on-board transmit control. This can include change of pulsewidth, number of pulses, change in pulse-coding for different polarizations, inter- and intra-pulse coding and multiple-pulsing schemes.

BIST and BITE

Automatic calibration based on injected CW signals, solar calibration and noise injection are also available on common digital receivers. The Built-In System Test (BIST) is the digital health monitoring technique wherein, instead of ADC output, a simulated signal is injected at an unused range at the digital receiver front-end. Some receivers such as Eldes NDRX (ELDES, 2012) also provide injection of test

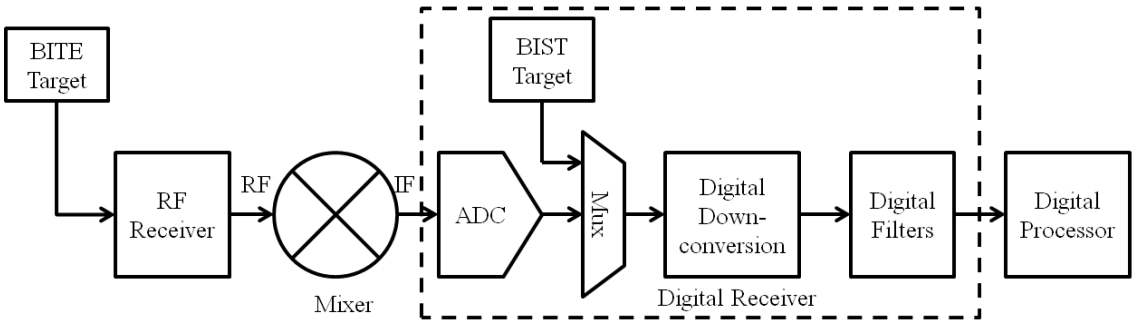

Figure 2.1: The target for BIST is injected to check the digital health while BITE target is used to indicate the health of the entire receiver.

signals at RF front-end. This technique is called Built-In System Equipment (BITE) (Figure 2.1). Several parameters to program the nature of the BITE and BIST targets are provided in digital receivers. While both the BIST target and its control may be provided in the digital receiver, only the digital control of the BITE target is included. The accuracy of these calibrations depends on a particular radar system specifications.

Transmit pulse sampling

Digital receivers usually have an additional digitization channel for the transmit pulse itself. This is especially important for magnetron radars which need the measurement of the transmit phase to perform the COHerent Oscillator (COHO) locking. The digital phase measurement also helps in range dealiasing using the phase modulation techniques. Further, the measurement of the amplitude of the transmit pulse is used for the calibration of the receiver. Also, the frequency of the transmit pulse is analyzed for errors in the nominal IF (Junyent et al., 2009). The usual sampling of the transmit pulse can be provided on-demand or at every pulse at a higher or identical sampling rate as the I-Q samples.

Multi-trip echo recovery with inter-pulse phase-coding

When the radar is operated at a high pulse repetition frequency (PRF), range aliasing of targets is frequently observed as second-trip echoes. They can also appear as false echoes at low elevation angles. Additionally, in magnetron systems, their Doppler information is incorrect and obscures the valid first-trip Doppler. Many commercially available digital receivers employ phase coding (random or not) on a pulse-to-pulse basis to suppress these second-trip echoes from beyond the unambiguous maximum range (Frush et al., 2002). In the phase coding scheme, the transmitted pulses are modulated with a phase code (ψ_n) and the received signal is then phase corrected (cohered) for error in the corresponding transmit phase code. This correction (or recoherence) is applied only on the first-trip echo while the second trip echo is phase

modulated by the difference of the two successive phase codes. If $V_f(k)$ and $V_s(k)$ are first and second-trip echoes from two distinct ranges, the received signal after recohering for the rst trip echo is given by

$$V_{fcorr}(k) = [V_f(k)e^{j\psi_n} + V_s(k)e^{j\psi_{n-1}}]e^{-j\psi_n} \tag{2.5}$$

$$= V_f(k) + V_s(k)e^{j(\psi_{n-1}-\psi_n)} \tag{2.6}$$

The second-trip echo has therefore been modified by a phase code resulting in the change of its spectral distribution. This information can now be used for suppressing $V_s(k)$. The measurement of the digital phase of the transmit pulse - enabled by employing a digital receiver - provides higher accuracy in suppressing multi-trip echoes.

Pulse compression

For the benefits explained in Section 1.3.1, pulse compression is also employed by many digital receivers. This is useful for far-range data if off-frequency short pulses are not transmitted in the near range. Further, a merged profile of the output moments from different subpulses are rarely provided by existing digital receivers.

Dual-PRF and staggered-PRT processing

The range velocity ambiguity is a fundamental limitation of radar observations. For uniform pulsing scheme the maximum unambiguous range r_a, is related to the maximum unambiguous velocity v_a, as

$$v_a r_a = \frac{c\lambda}{8} \tag{2.7}$$

where c is the speed of light and λ is the radar wavelength. A higher pulse repetition time (PRT) causes an increase in maximum unambiguous range but a decrease in the maximum unambiguous velocity. Often *staggered PRT* pulsing scheme (Figure 2.2) is employed to mitigate range-velocity ambiguity where the transmit pulse that alternates between two different pulse intervals, T_1 and T_2. For pulse pair processing in this case, the unambiguous Doppler velocity is inversely proportional to

the pulse repetition time difference (Zrnić and Mahapatra, 1985) while the maximum unambiguous range can then be related to the sum of the pulse repetition times,

$$v_a = \frac{\lambda}{4(T_1 - T_2)} T_1 > T_2 \tag{2.8}$$

$$r_a = \frac{cT_2}{2} \tag{2.9}$$

For the staggered PRT scheme, the unambiguous range-velocity equation then transforms to

$$v_a r_a = \frac{c\lambda}{4} \tag{2.10}$$

However, due to the non-uniform sampling, standard clutter suppression techniques

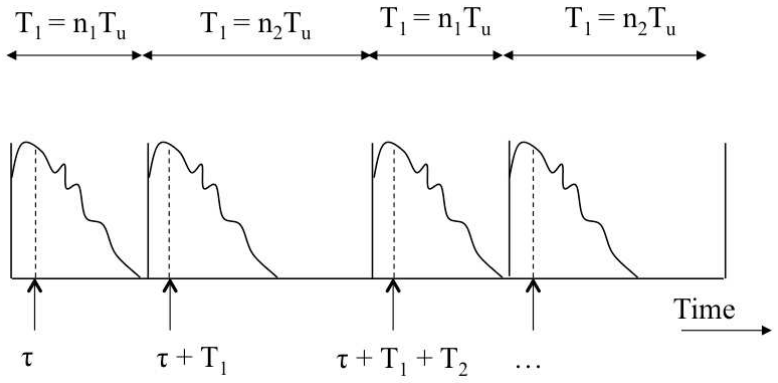

Figure 2.2: Staggered PRT pulsing scheme. The stagger ratio is n_1/n_2.

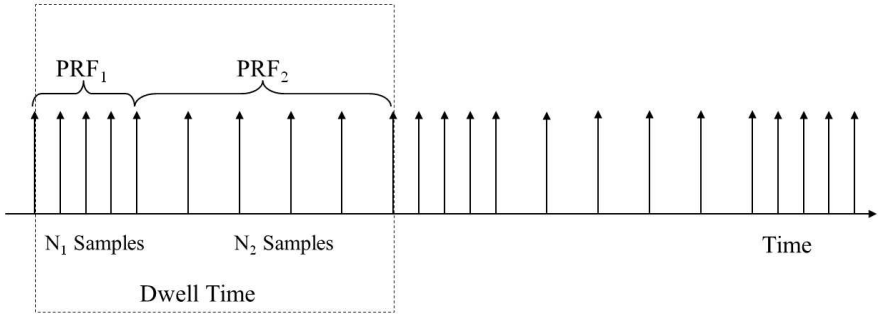

Figure 2.3: Dual PRF pulsing scheme. Different number of pulses are transmitted in each of the two PRF intervals.

cannot be directly applied in staggered PRT waveforms. An alternative way is to

employ a *dual-PRF* waveform (Figure 2.3) so that the clutter filtering can be applied to the uniformly sampled portions of the received signal. However, this causes higher variance in the products since smaller number of samples are used for estimates compared to the uniform pulsing. Also, there is a possibility of dealiasing errors due to the inherent uncertainty in the estimation of velocities. Many digital receivers provide processing for both of these pulsing schemes though clutter filtering may not be available for staggered PRT.

Attenuation correction

From equations 1.9-1.10, it is clear that radars operating at shorter wavelengths provide better sensitivity. However, the decrease in wavelength leads to the increased loss of sensitivity due to hydrometeors along the signal path (Bringi and Chandrasekar, 2001, 490-513). For the same rainfall rate, signals at the X-band (32 mm) and C-band (54 mm) attenuate 30 and four times more than signals at the largely unattenuated S-band (100 cm) Figure 2.4). Further, the attenuation is proportionally larger for higher rainfall rates for a radar operating at a particular wavelength (Figure 2.5).

An intense rain can cause a complete loss of the X-band signal. Many digital receiver-processors therefore provide real-time attenuation correction in the software for C- and, occasionally, X-bands. By calculating the differential phase shift between the vertical and horizontal orthogonal signal planes, the attenuation of the returning C-band echoes can be estimated. A similar algorithm exists for X-band correction. None of the commercially available receivers provide real-time attenuation correction for Ku- and Ka-bands.

Clutter filtering

One of the most computationally intensive and sophisticated feature of digital receivers is the mitigation and filtering of the ground clutter. Ground-clutter targets often contaminate radar returns and mask the desired weather echoes. The clutter filter can be applied in the time domain (Torres and Zrnic, 1999) or in the frequency

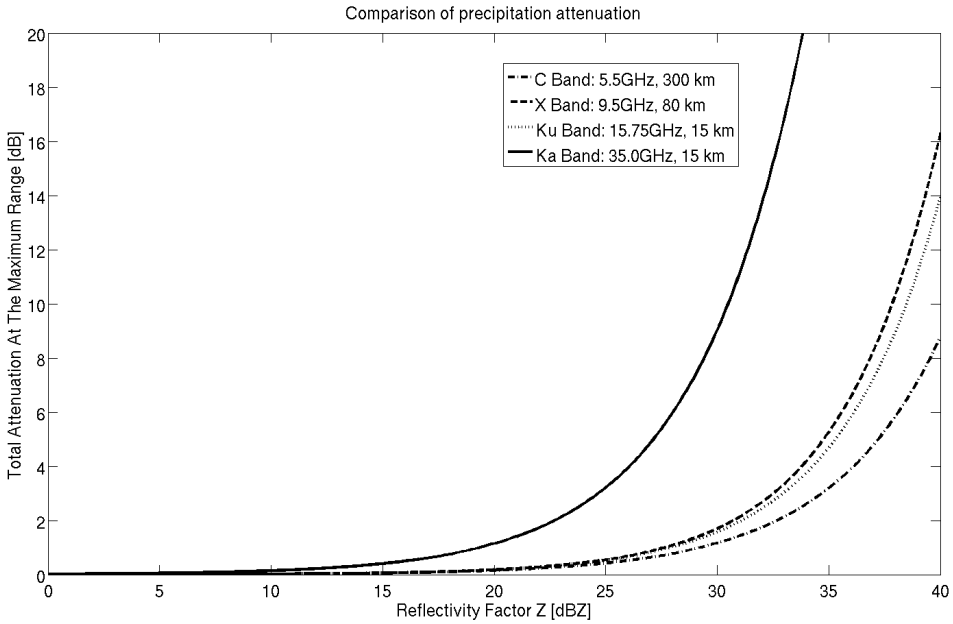

Figure 2.4: Comparison of the total path precipitation attenuation at maximum detectable range for different operating wavelengths of the radar.

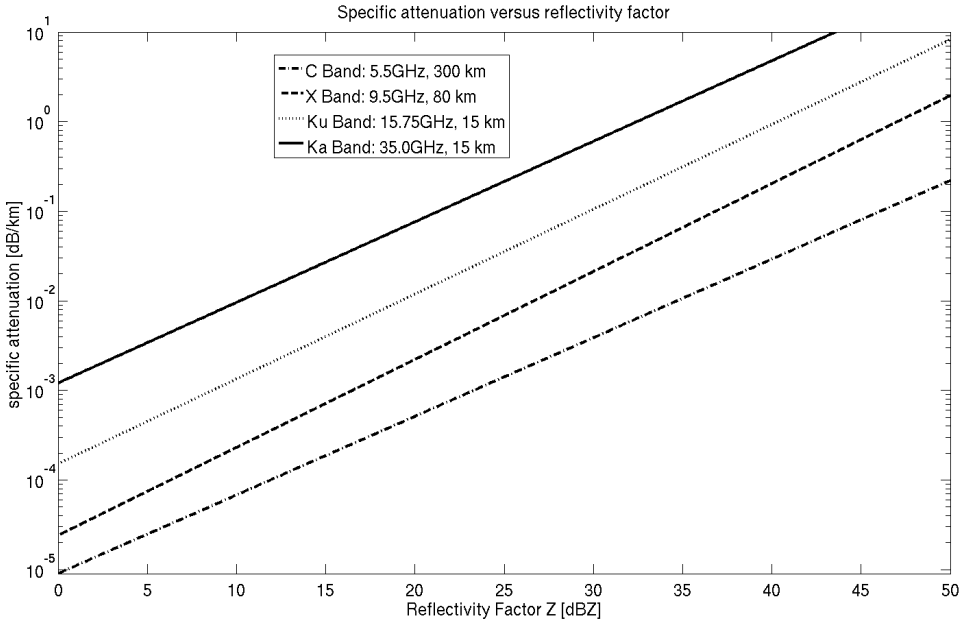

Figure 2.5: Linear approximation of specific attenuation for given reflectivity factor Z at C-, X-, Ku- and Ka- bands. With the increase in rainfall intensity (and thereby in Z) increases attenuation.

domain (Siggia and Passarelli, 2004). A further post-processing for improving data quality and clutter-censoring, usually automated, is often performed on the integrated radar moments in the signal processors. Many commercial digital receiver softwares provide proprietary clutter filtering schemes while research radars have experimented with the implementation of numerous clutter filtering algorithms over the years (Hubbert et al., 2009) (Nguyen et al., 2008).

2.2 Industry solutions

Several commercial vendors offer digital IF receivers and signal processors for weather radars. Some of these products are now reviewed here. The examples cited here are chosen based on their greater market presence, individual research significance, availability of detailed product literature and the familiarity of the author with these products. Table 2.1 shows a comparison and features of commercially available digital receivers and signal processors for weather radars.

2.2.1 Vaisala RVP series

In 1996, Vaisala Sigmet Inc. introduced RVP (Radar Video Processor) series of commercial digital IF receiver and signal processors for a weather radar system (Vaisala Inc., Sept 2009). This product marketed as RVP7 was upgraded to RVP8 in 2003 using an open hardware and software architecture on standard personal computer (PC) hardware under the Linux operating system. RVP8 series has been highly successful with over 400 units delivered worldwide and is used in the current generation National Oceanographic and Atmospheric Administration (NOAA) NEXRAD (NEXt generation RADar) systems. RVP8 transmitter card also provided capability to digitally synthesize the IF transmit waveform and output to be mixed with the STALO to provide the RF waveform to the transmitter amplifier such as the Klystron or Traveling Wave Tube (TWT). Vaisala released Field Programmable Gate Array (FPGA)-based RVP900 series of processors in 2009 which eliminated the dependency

Table 2.1: Features of commercially available weather radar digital IF receivers

Technical specification	Vaisala RVP900	GAMIC ENIGMA-IV	Gematronik GDRX
IF Sampling			
IF	30/60 MHz	30/60 MHz	60MHz
ADCs	100 MHz, 16-bit	>70MHz, 16-bit	80 MHz, 14-bit
Dynamic range	85 - >105 dB	>115dB	>105 dB
HI-Gain and LO-Gain channels	√	√	√
Wideband subsampling	×	×	×
Transmit Pulse And Control			
On-board waveform generator	√	√	√
Transmit-pulse burst sampling	√	√	√
Alternate transmit, simultaneous receive mode	√	√	√
Phase agility and phase coding	√	√	√
IF Processing Unit			
Digital pulse compression (DPC)	√	√	√
Multi-pulse processing	×	×	×
Host-interface	PCI	PCI	cPCI
Networked data transfer	√	√	√
Signal Processing Modes			
Dual-pol processing	√	√	√
Dual-PRF	√	√	√
Staggered PRT processing	×	×	×
Multi-trip echo recovery	√	√	√
Real-time attenuation correction	C-band	X-band	X-band
Clutter-filter	GMAP	spectral DFT	GIP

of multiple Peripheral Component Interconnect (PCI) slots on the host computer by turning the processor into a networked device. In addition, the RVP900 provided a single interface for the horizontal and vertical channels of dual-polarization radars. The RVP9 processor has been accepted for installation in the next generation upgrade of the Terminal Doppler Weather Radar (TDWR) (Cho and Weber, 2010).

The RVP900 provides 100 MHz, 16-bit sampling of the analog IF signal (typically, 30 or 60 MHz) independently on five channels (including the transmitter burst channel for magnetron-based systems). A very wide dynamic range (85-105 dB) can be achieved by using high- and low-gain channels for both polarizations. The processor allows for pulse compression, selectable pulse repetition frequency (PRF), range resolution, a variety of advanced processing algorithms (including velocity unfolding, second trip echo recovery and Gaussian Map Adaptive Processing (GMAP) clutter filter) and controls to program IF filters. The RVP series processor has been successfully used as a digital receiver solution on magnetron (NASA Polarimetric or NPOL S-band radar) and klystron (Kumpula C-band weather radar installed at University of Helsinki) based systems. The RVP900 series of processors currently doesn't provide a digital receiver solution which can process multi-pulse waveforms for mitigating range-velocity ambiguity and blind zone for solid-state transmitters.

2.2.2 GAMIC ENIGMA series

GAMIC mbH has developed ENIGMA series of digital IF processors for real-time Doppler signal processing for weather radar sensors (GAMIC, 2012). The latest product in the series ENIGMA IV was released in 2011. It is a PC host-based Doppler signal processor with digital IF-processing and transmitter controller and is available in 30 and 60 MHz IF versions. Similar to RVP900, ENIGMA-IV employs 16-bit Analog-to-Digital-Converters (ADCs) with sampling rate exceeding 70 MHz and a typical 100 dB total dynamic range. The receiver can be programmed to process IF pulses up to 20 μs with pulse compression, perform Built-In System Test (BIST)

and Built-in Test Equipment (BITE) and can remotely configure all processing functions via host or serial line IF Test Signal Generator. The use of spectral Discrete Fourier Transform (DFT) clutter filtering together with spectral interpolation yield clutter cancellation ratios which are basically limited by the system phase noise floor. ENIGMA IV - DFT filtering gives an intrinsic phase stability and subsequently clutter suppression in the order of >80 dB on the IF bench test with a high stability reference source (Malkomes et al., 2008).

GAMIC products are installed in large weather radar networks, like at DWD (German Weather Service) operating dual-polarized radars in a nationwide composite (GAMIC mbH, July 29 2011). ENIGMA processors are also deployed in radar systems built by Radtec Engineering Inc. (Radtec, 2012). Though ENIGMA-IV processors have a highly programmable transmit control, the receiver module is unable to handle multi-pulse processing.

2.2.3 Gematronik GDRX

Another major commercially available weather radar digital IF receiver and signal processor is the GDRX series manufactured by SELEX-Gematronik mbH. GDRX consists of a compact-PCI or cPCI-based digital receiver front-end called GDRX-RX and a signal processing back-end, called GDRX-SP. By using dual-channel, high-precision 14-bit A/D Converter input stages, GDRX-RX achieves high sensitivity and better linearity over an enlarged dynamic range that is comparable to an 18 bit digitizer (Gematronik, 2012). It includes an on-board waveform generator for coherent transmitter types supporting frequency and phase agility, phase coding and pulse-compression.

GDRX supports special functions such as multi-trip echo recovery, frequency-domain Gaussian Iterative clutter filter Processing (GIP), dual-PRF range extension and gas attenuation correction. GDRX-RX delivers I/Q data to the GDRX-SP high performance PC via a gigabit Ethernet interface. The standard IF frequency served

by GDRX is 60 MHz while IF sampling is carried out at 80 MHz. The receiver doesn;t support wideband IF sampling or multi-pulse processing.

GDRX has been used in the Australian (Jarrott et al., 2007) and the recently upgraded Dutch (Beekhuis and Holleman, 2008) weather radar network.

2.3 Research solutions

Radars operating primarily for research in engineering and meteorology require a high degree of adjustability, introduction of new features and processing modes in their digital receivers and processors. As such, several commercial features may be removed in these designs. In this section, some of the research solutions are listed based on author's familiarity and their research significance. Table 2.2 summarizes the key features of these receivers.

2.3.1 CSU-CHILL receiver

Colorado State University (CSU) operates S-band dual-polarized CHILL weather radar currently operated from its location at Greeley, Colorado. Initially jointly developed by the University of Chicago and the Illinois State Water Survey (CHILL; Mueller and Silha (1978)), the operation radar was transferred to CSU to operate from its present site in 1990. The design of the radar receiver chain was modified in 1999 to accommodate a Lassen Aspen digital-IF receiver and signal processor in 1999 (Brunkow et al., 2000). During 2005-2007, the radar was upgraded with a new digital waveform generator for the klystron transmitter and a digital receiver (George, 2007).

The current CSU-CHILL digital receiver is ICS-554E Digitizer Board - a high-speed data acquisition PCI Mezzanine Card (PMC) which consists of an IF digitizer, the signal processing FPGA board and a control FPGA. The board has four 14-bit 40 MHz Analog-to-Digital (ADCs) to acquire the incoming signals at an IF of 50 MHz and also providing a 96dB dynamic range to the digitizer. The outputs from the ADCs are routed to the main signal processing FPGA for digital downconversion, two-stage

decimation, sampling transmit samples and appending antenna position and GPS IRIG-B information. These output streams are then written to an on-board FIFO from where it is read into a host computer via PCI interface for the dissemination of data over a network. The receiver can be programmed to output I-Q streams at 1MHz or 5MHz rate at a programmable range resolution. The second-stage filter can be programmed for decimation as well as pulse compression. However, CSU-CHILL radar doesn't employ pulse compression in the usual modes of either transmission or reception. The signal processor hardware can simultaneously archive the raw time series data as well as moment data in UF (Universal Format) files. However, the transmit pulse samples can only be recorded on-demand at pre-downconversion stage of the receiver. The receiver doesn't support frequency-diversity pulse-compression processing but has been successfully used to implement alternate mode processing and phase coding (Chandrasekar and Bharadwaj, 2009).

2.3.2 CASA EDAQ

In the last decade, with the vision of employing an automated network of low-cost short-range weather radars with overlapping coverage domains to improve the coverage of the lowest portion of the atmosphere (Chandrasekar and Jayasumana, 2001), the National Science Foundation (NSF) established a consortium of four universities [Colorado State University, University of Massachusetts (lead university), University of Oklahoma, and University of Puerto Rico at Mayaguez] called Collaborative Adapting Sensing of the Atmosphere (CASA) - Engineering Research Center (ERC). During early 2006, the first test bed of X-band radar systems was deployed in central Oklahoma Integrated Project 1 (IP1). It consisted of four polarimetric, X-Band, magnetron transmitter, weather radar nodes at Cyril (KCYR), Chickasha (KSAO), Rush Springs (KRSP), and Lawton (KLWE). Recently, CASA and the North Central Texas Council of Governments (NCTCOG) have embarked on a five-year project to

create the Dallas Fort Worth (DFW) Urban Demonstration Network which will deploy a network of eight dual-pol, X-band radars to demonstrate improved hazardous weather forecasts, warnings and response in a densely populated urban environment (Chandrasekar and Philips, 2012).

The typical weather events observed by CASA radars includes tornadoes, severe storms and floods. These radar systems therefore demand high-throughput sustainable, high-speed data acquisition and processing systems. The Electronic Data Acquisition (eDAQ) unit - the digital receiver for CASA IP1 systems - employs two 14-bit 105 MHz ADCs to sample horizontal and vertical signals at an IF in the range of 5-240 MHz (Khasgiwale, 2005). An auxiliary analog channel is used to feed the radar positioner data to the receiver. A data processing FPGA digitally downconverts the incoming IF signals and decimates the I-Q stream using a cascaded integrator-comb (CIC) filter. This output stream, available at 48m and 96m range resolution, is passed to a networking FPGA which routes the processed data to the signal processor over Gigabit Ethernet interface via User Datagram Protocol (UDP). The X-band radars with conventional uniform pulsing will have low unambiguous velocity, and increasing the PRF will result in multiple trip overlays because storms can extend over a large distance. In addition, the radar systems deployed use a 28 beamwidth antenna and are intended to make observation close to the ground. The radar observations with such a system will be severely contaminated by ground clutter (Francesc et al., 2010). The radar signal processing methodologies employed for CASA radar systems, therefore, implement phase coding, dual-PRF, and ground clutter ltering using adaptive spectral processing to mitigate the challenges. The eDAQ receiver configuration, though highly configurable and useful for research (Bharadwaj et al., 2010), is limited to magnetron-based radar systems in its applications.

2.3.3 USRP-II receiver

The Universal Software Radio Peripheral (USRP) devices are general-purpose, computer-hosted, inexpensive, software defined radios developed and marketed by

Ettus Research, LLC (Ettus, 2012). The PC interface of USRP boards is either through a high-speed USB or Gigabit Ethernet link. The second-generation devices USRP-II are equipped with dual 14-bit 100 MHz ADCs and a Xilinx FPGA to process the incoming signals. The devices have 400 MHz on-board Digital-to-Analog Converters (DACs) for purposes of waveform generation and upconversion. Ettus also provides Radio Frequency (RF) front end transmitter and receiver daughter boards for frequencies ranging from 50MHz to 5GHz. The USRP-II receiver provides for direct IF sampling up to 250 MHz. One of the commonly used software frameworks to support USRP hardware driver is GNU Radio (GNU Radio, 2012) which is an open source software suite to develop software-defined radios.

The USRP-II has been successfully used as a radar receiver for incoherent scatter radars, meteor radars and lunar radars where most of the processing is done offline on the downconverted output from the device (Vierinen et al., 3-7 August 2009). Some of the other advanced processing of a radar receiver such as pulse compression as well as on-board waveform generation have also been demonstrated, in principle, using USRP boards for software-defined radars (Patton, 2007). Recently, a prototype of a software-defined solid-state Frequency Modulated Continuous Wave (FMCW) radar which works at a center frequency of 2.1 GHz with a bandwidth of 750 kHz has been realized for weather-surveillance applications using USRP-II and GNU Radio (Prabaswara et al., 2011).

Despite the availability of advanced and flexible scientific computing software suite for USRP-II, the 25 MHz IQ output streaming bandwidth of the device is a serious setback for multi-pulse processing for solid-state transmitters. Though, the ADC sampling frequency of 100 MHz is within the acceptable limits of quantization noise, it is lower compared to currently available options in the market (Pentek, 2012). Moreover, the on-board USRP-II FPGA belongs to Xilinx Spartan family which is a low-density device for computationally expensive processing for weather radar receivers.

Table 2.2: A comparison of research weather radar digital IF receivers

Technical specification	CSU-CHILL receiver	CASA eDAQ	USRP-II
DRX Board			
Transmitter	Klystron	Magnetron	Klystron[a]
IF range	50 MHz	5-240 MHz	250MHz max.
ADCs	40 MHz, 14-bit	>105MHz, 14-bit	100 MHz, 14-bit
Wideband subsampling	×	×	×
Transmit Pulse And Control			
On-board waveform generator	×	×	√
Transmit-pulse burst sampling	√	√	×
Alternate transmit, simultaneous receive mode	√	×[b]	×
IF Processing Unit			
Digital pulse compression (DPC)	×[c]	×	×
Multi-pulse processing	×	×	×
Host-interface	PCI	Embedded ARM processor	USB
Networked data transfer	√	√	√
Signal Processing Modes			
Dual-pol processing	√	√	√
Dual-PRF	×	√	×
Staggered PRT processing	√	×	√
Multi-trip echo recovery	×	√	×

[a] The reference here are radars described in (Vierinen et al., 3-7 August 2009).

[b] Though CASA receiver system is capable of processing the alternate transmission mode data, this has been rarely deployed for operational use.

[c] Though the CSU-CHILL receiver's second stage filter can process pulse compression data (George, 2007), this is not a part of normal radar operation.

2.4 Summary

The digital receiver for the radar has persuasive advantages of high flexibility, high stability, high precision and compact construction over their analog counterparts. It should be noted that the digital receivers and signal processors for weather radars are increasingly becoming more sophisticated in design and performance over the years. This overview puts the existing technology in perspective of the receiver technology required for the solid-state radars. Though the digital receiver described in the next chapter is designed to be compatible for addition of almost every feature described in Section 2.1, the focus is to provide a solution for pulse compression wideband receiver.

CHAPTER 3

DIGITAL RECEIVER SOLUTION FOR SOLID-STATE TRANSMITTER RADAR

There are several parameters which characterize the performance of a digital radar receiver (Tsui, 2009). Almost all modern digital radar receivers sample the received analog signal at IF stage. The analog-to-digital conversion process directly affects the sensitivity and dynamic range of the receiver. As discussed in Chapter 2, several existing digital radar receivers provide competing performance benefits on parameters pertaining to the digitization of IF signals (Table 2.1). It is the flexibility to process diverse waveforms and capability to render algorithms in real-time to improve data quality which distinguishes individual designs. This chapter describes the digital receiver solution for the solid-state radars. The principle of operation and the interfaces to other subsystems is then introduced and described.

3.1 Hardware requirements

The digital receiver for the solid-state transmitter radar discussed in this work is primarily aimed for research and experimentation. Therefore, the hardware requirements, listed below, for the receiver are unique and aimed for maximum flexibility:

- The receiver should accept dual-polarized analog inputs for IF sampling from the transceiver module.
- Dynamic range of >85 dB and subsampling at more than 100 MHz.

- The on-board FPGA should have sufficient resources to implement filters of several hundred taps and sufficient glue-logic.
- The receiver should be able to interface with the waveform generator module to accept various triggers for information on PRT sequences and polarization modes.
- The receiver should provide near real-time stamping of the antenna information from the antenna position decoder.
- Interface for the GPS time stamp and location information in near real-time.
- Ability to sample transmit pulse from the calibration path in the transceiver.
- Capability to render the raw time-series of all the subpulses for all range gates over ethernet to the moment processor and optionally archive it.
- Field programmability of the receiver from the host computer and configurability of parameters like downconversion frequency, BIST mode and triggers from various sources.
- Self-reporting of the temperature and voltage levels of the sensors.
- Compact form factor and high-speed interface with the host computer.

3.2 General description of the wideband IF receiver hardware

The Pentek 7150 board (Pentek, 2012) (Figure 3.1) is chosen for digital receiver (DRX) processing hardware to meet all the desired hardware specifications. The PMC module of 7150 board is installed on a single board computer provided by Concurrent Technologies (CCT, 2012). For in-lab testing, the board is mounted on a Technobox 4733 PMC carrier board (Technobox, 2012). The following subsections describe these pieces of hardware.

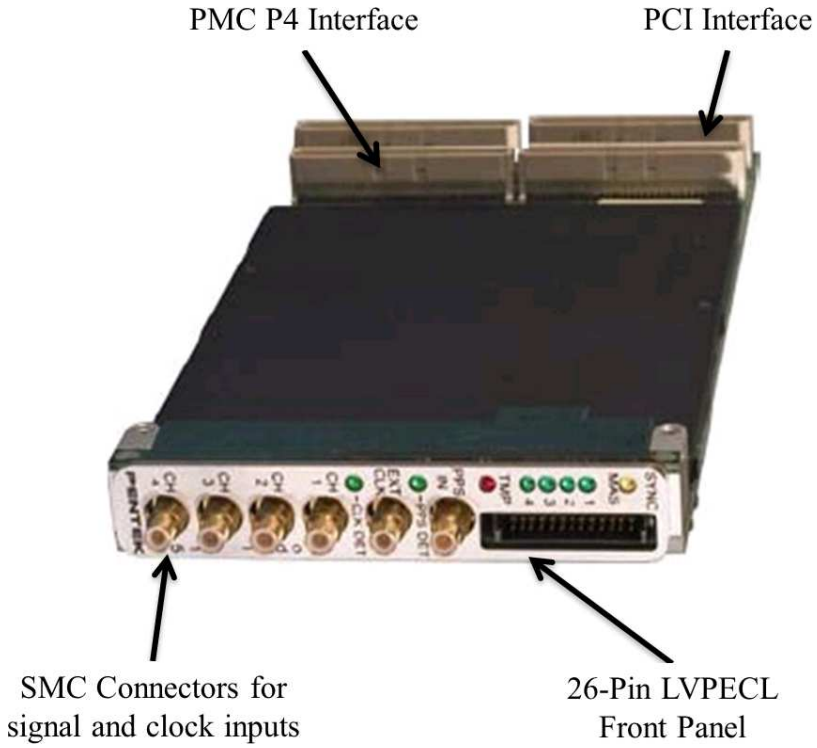

Figure 3.1: Pentek 7150 board with the SMC, LVPECL and PMC interfaces.

3.2.1 Pentek 7150

The Pentek Model 7150 (Figure 3.2) board is a multi-channel, high-speed data converter suitable for connection to HF or IF ports of a communications system. It includes four 200-MHz, 16-bit A/D converters accepting analog inputs routed through the SMC (SubMiniature version C) connectors. The board uses the PMC format described before and the PMC module can be attached directly to any digital signal processing (DSP) baseboard or a single board computer equipped with a PMC expansion site, or to a PMC bus adaptor to PCI, cPCI, PCIe, etc.

The 7150 features two Xilinx Virtex-5 FPGAs (Xilinx Inc., Feb 6, 2009) for signal interfaces and processing. The first FPGA, called the "Processing FPGA", is a user-programmable board to provide signal translation and processing. A second FPGA, identified as the "Interface FPGA", is not accessible to the user and provides board interfaces including PCI-X and PCI Express. Custom I/O connections are provided to both FPGAs through the optional PMC P4 connector (Figure 3.1). The module

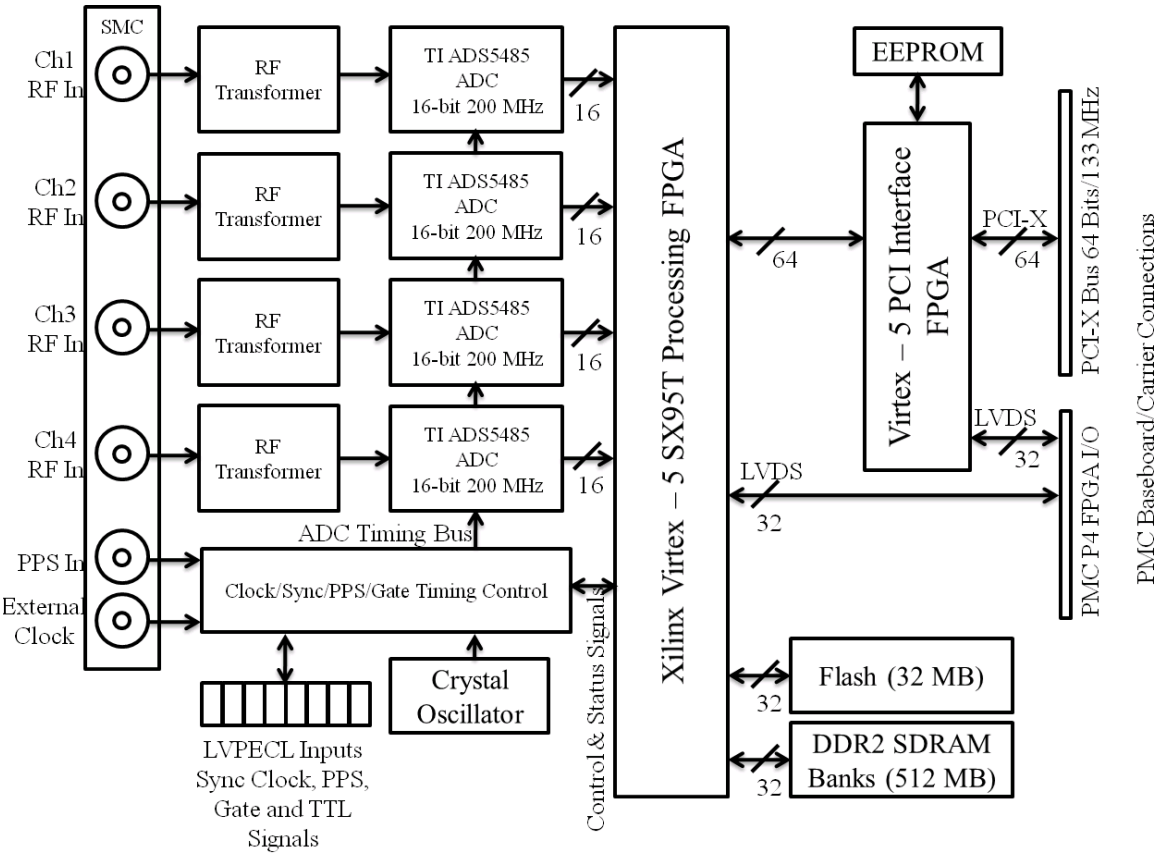

Figure 3.2: Block diagram of digital receiver board.

includes an onboard crystal oscillator for clocking, but can also accept external clocks through front panel connectors. The 7150 is equipped with an Low-Voltage Positive Emitter-Coupled Logic (LVPECL) front panel clock and sync bus that can synchronize up to four modules with built-in master/slave functions. The 7150 includes up to 1.5 GBytes of double data rate synchronous dynamic random-access memory (DDR2 SDRAM). This memory is controlled by the FPGA and is organized as two or three banks of 512 MBytes. Separate address and data per bank allow simultaneous access to all banks. This memory can be used as for data capture, as buffer memory when transferring data between board resources or to offboard resources, or as a memory resource for custom FPGA applications.

3.2.2 CCT single-board computer

While mounted on the radar system, the Pentek 7150 board should be enclosed in a module which provides connections to a single board computer and PMC carrier board. This module, provided by the Concurrent Technologies (CCT, 2012), consists of the PP PMC/202 CompactPCI PMC Carrier Board on which the board is mounted. The PP PMC/202 provides two PMC sites (either 32- or 64-bit) and can accommodate either two single-width PMC modules or one dual-width PMC module (Figure 3.3). The site supports both 33MHz and 66MHz operation. The digital receiver configuration is set for 64-bit operation at 66MHz. The carrier board contains a PLX Technology PCI 6254 PCI to PCI bridge chip which allows access to the PMC modules through a connected single board computer. The digital receiver configuration employs the PP 40x/04x CompactPCI Intel Core 2 Duo Processor Single Board Computer operated using a OCZ Vertex Series iInternal solid state drive (SSD). The PP 40x/04x single-board computers are particularly designed for the CompactPCI bus architecture. They are based upon the Intel Core Duo or the Intel Core 2 Duo processor, Intel 945GME Express chipset with Graphics Controller, two Intel 82573L and two Intel 82541PI single channel Gigabit Ethernet controllers, an IEEE 1386.1

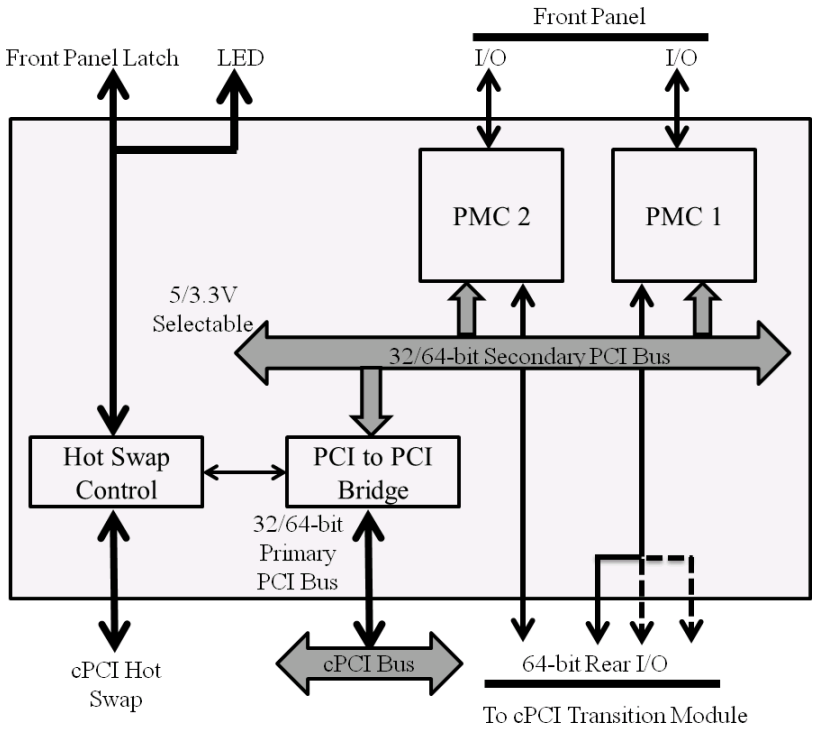

Figure 3.3: Concept diagram of the CCT CompactPCI PMC carrier board.

PMC interface, CompactFlash socket, optional on-board mass storage and interfaces for standard PC-AT (Advanced Technology) based peripherals (Figure 3.4). The I/O routing to CompactPCI backplane is supported by both PMC sites on the CCT AD PP2/001 cPCI bus transition module. The I/O connections from the PMC sites to J3 and J5 are routed as differential pairs to support the use of high-speed SCSI (Small Computer System Interface) PMC modules using LVDS (Low-voltage differential signaling) signaling (Figure 3.5). This feature is used to route the signals and triggers from the waveform generator board to the digital receiver. Figure 3.6 shows the exterior of the single-board computer enclosure with the LVPECL and SMC interfaces visible.

3.2.3 Technobox PMC carrier board

For development and testing purposes, the Pentek 7150 board can however be plugged onto the motherboard of the development machines using a generic PMC-to-PCI Express carrier card (Figure 3.7). The Technobox 4733 64-bit PMC-to-PCI

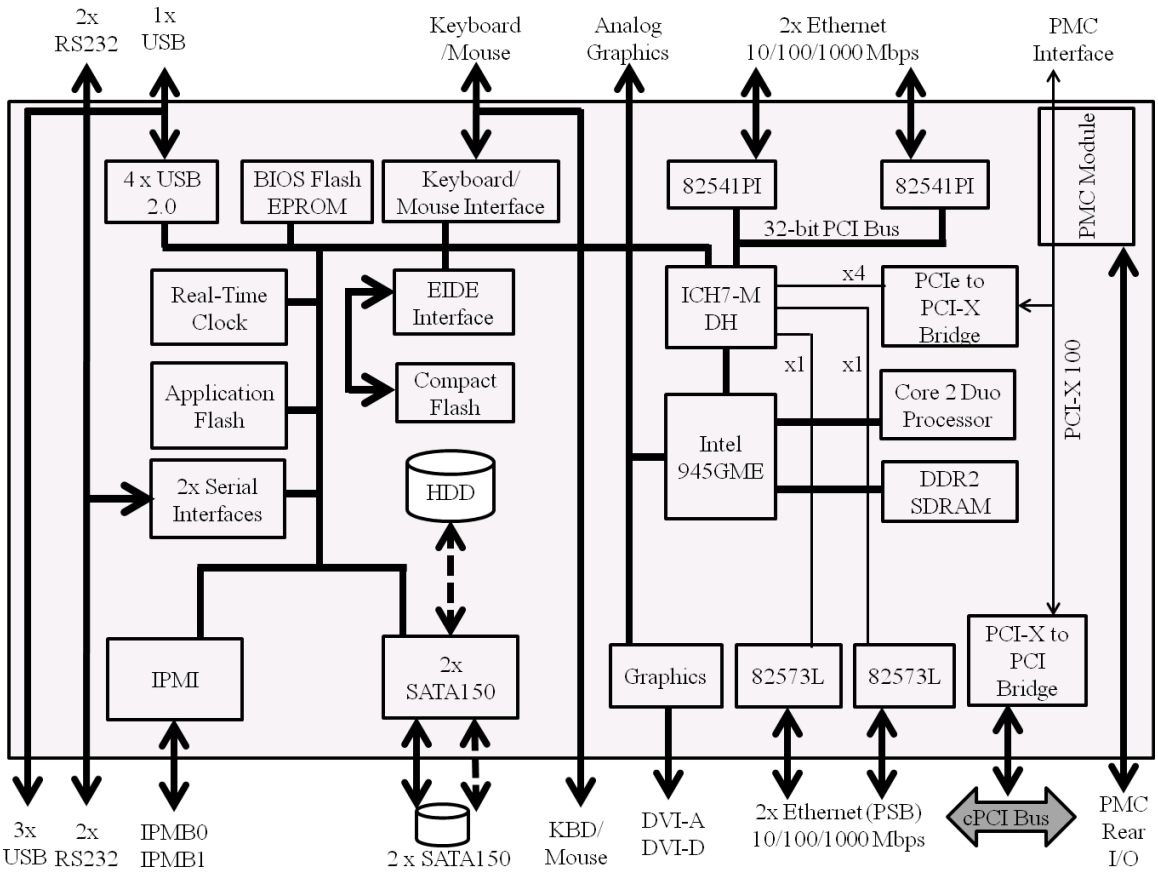

Figure 3.4: Block diagram of the CCT Single board computer with the CompactPCI interface.

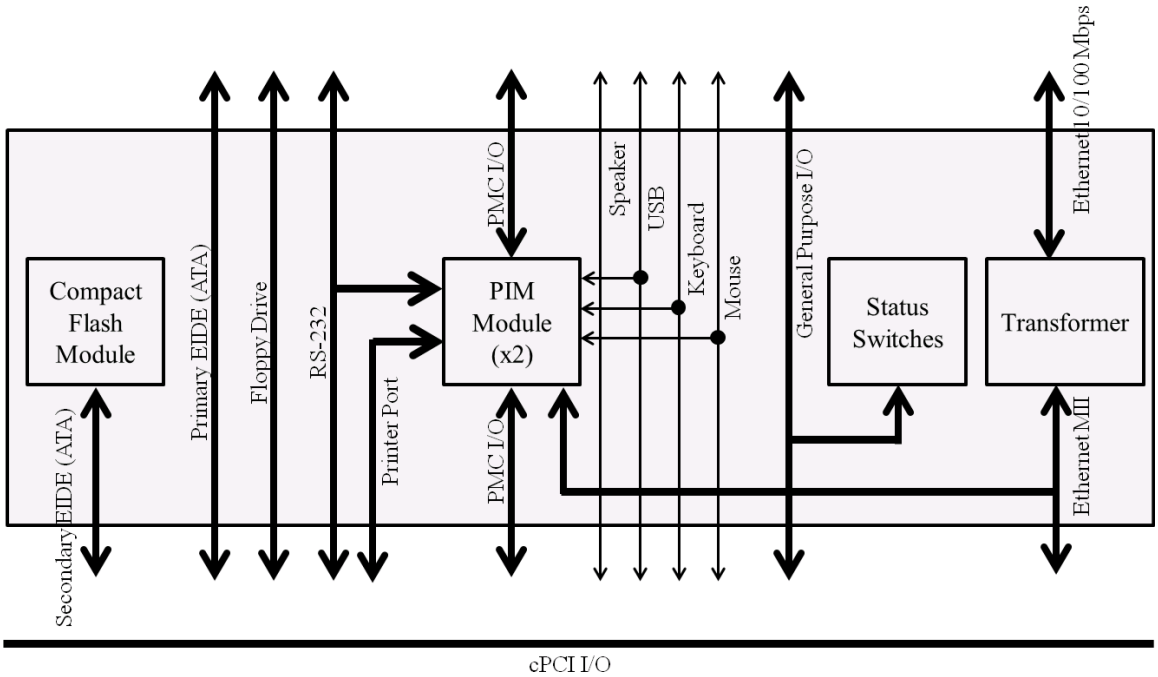

Figure 3.5: CCT rear bus transition module.

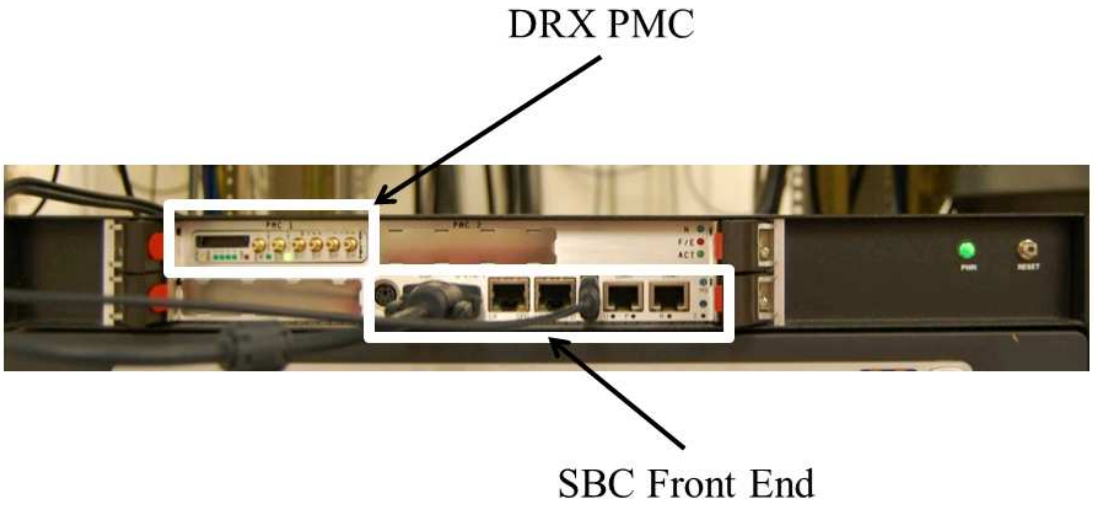

Figure 3.6: The digital receiver PMC card mounted on a single-board computer enclosure.

Express carrier card (Figure 3.8) with transparent bridge is employed to plug the 7150 board onto the chassis of the development computer. These boards are universal PMC/PMC-X cards in a 4X, 8X or 16X PCI Express slot using a PEX8114 bridge running in transparent mode. The secondary (PCI/PCI-X) side operates at 33, 66, 100 or 133 MHz, all of which are compatible with the Pentek 7150 board. While

Figure 3.7: Technobox 4733 board.

using the Pentek 7150 with the Technobox 4733 in a thermally unenclosed chassis,

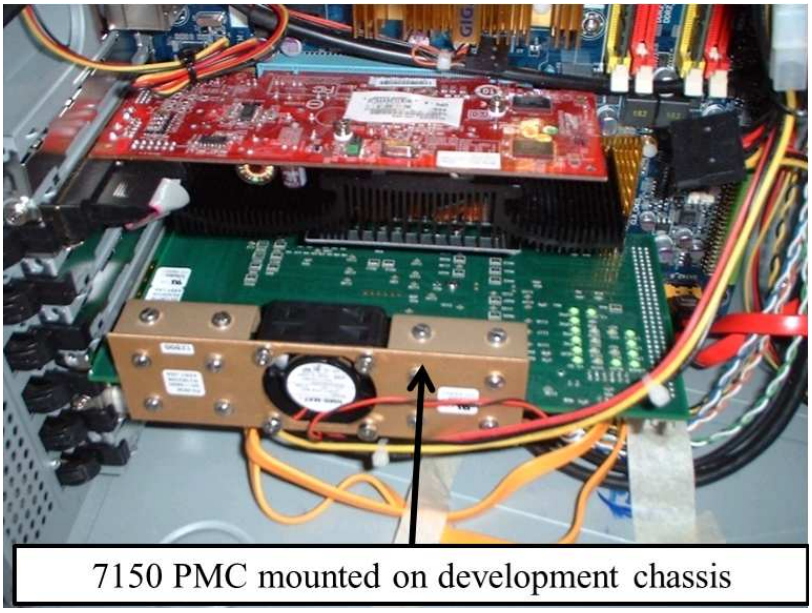

Figure 3.8: The PMC card mounted on the chassis of a development computer using the PMC-to-PCI Express carrier card.

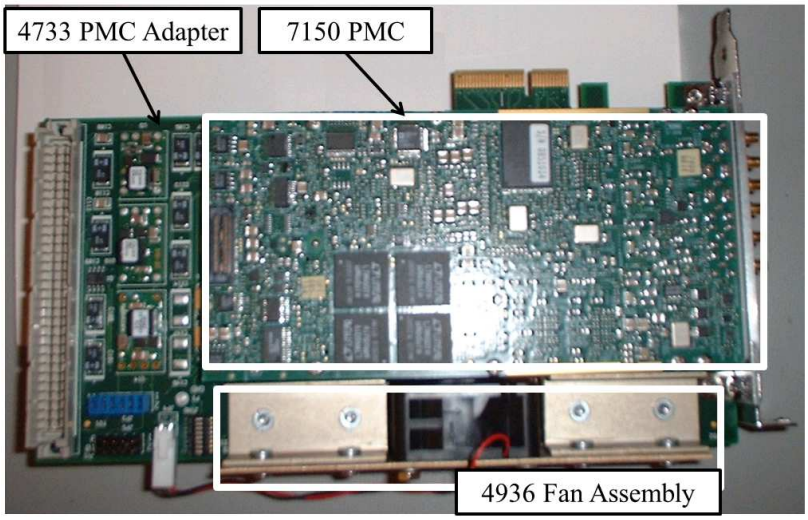

Figure 3.9: Technobox 4936 mounted on the 4733 board with the Pentek 7150 PMC module.

it is possible that the FPGAs on 7150 board are not provided appropriate amount of cooling system. This can be avoided by using a Technobox 4936 fan assembly (Figure 3.9) with the PMC carrier board.

3.3 Principle of operation

The Pentek 7150 is the most computationally critical element of the digital receiver hardware. The digital receiver directly interfaces with the analog IF signals, the reference external clock and 1 pulse per second (PPS) signal from the GPS at the SMC connector, waveform generator at the SCSI connector, antenna position decoder at RS-422 or SCSI connector, GPS time stamp source at the RS-232 or SCSI connector, the host computer at PMC level, FPGAs using the JTAG (Joint Test Action Group) assembly and finally the voltage and temperature sensors (Figure 3.10). The following subsections describe the principle of operation of each of these interfaces.

3.3.1 PMC baseboard interface

The Processing FPGA serves as a control, processing and status engine with data and programming interfaces to each of the onboard resources including the A/D converters and DDR2 SDRAM memory. The Processing FPGA can be reprogrammed by the user from a PMC baseboard processor. A second Xilinx Virtex-5 FPGA, the Interface FPGA, provides the boards external PCI-X interface. An interface to the P4 PMC connector with 16 pairs of LVDS connections to the Processing FPGA and 16 pairs of LVDS connections to the Interface FPGA for custom I/O is also provided. The Pentek JTAG Assembly provides the RS-232 and Ethernet interfaces to the Processing FPGA.

3.3.2 FPGA and software debug Interface

The Processing FPGA is connected to the PMC baseboard through a PCI-X Master/Slave interface, the Pentek PCI7150. The PCI7150 is programmed in a Xilinx

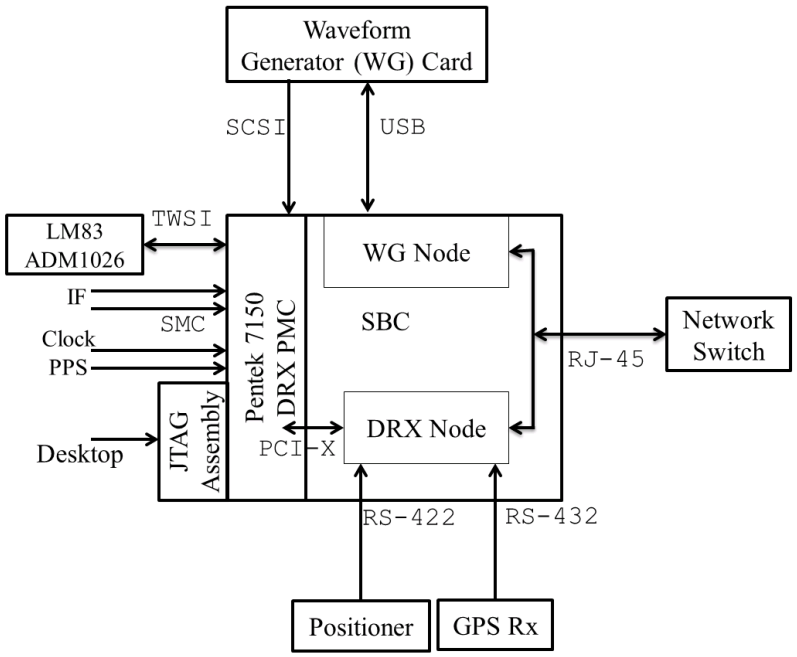

Figure 3.10: Digital receiver hardware and associated interfaces. The undecoded antenna position and GPS timestamp can also be routed through the SCSI connector. This information can then be decoded directly in the FPGA hardware.

Virtex-5 FPGA (the Interface FPGA). This interface includes separate DMA controllers for efficient transfers to and from the module. Data widths of 32 or 64 bits and data rates of 33, 66, or 100 MHz are supported. Through this PCI-X interface, any processor on the PMC baseboard can receive data from any A/D converter. Any PCI Bus Master can control all programmable features on the board, including the four A/D converters, the high-speed interfaces, SDRAM memories, and all FPGA memory map registers. While the Processing FPGA is configured online through a Flash memory, the interface FPGA (locked to the user) is programmed through a serial EEPROM.

3.3.3 Interrupts, temperature and voltage sensors

The 7150 board has several maskable interrupt sources. The PCI interrupts may be generated by A/D converter overload, DMA transfers, FIFO flags, Sync Bus gate or sync signal transitions, clock loss on either Sync Bus, hardware over-temperature,

or power supply over-voltage. The National Semiconductor LM83 is a digital temperature sensor and the Analog Devices ADM1026 digital voltage sensor are present onboard with with a 2 wire serial interface (TWSI)to provide constant monitoring of critical voltages and temperatures of the 7150 PCB. The sensors are programmable for voltage and temperature limits. If the voltage/temperature fall outside of the set limits, an interrupt can be generated. These values are monitored using the Munin network monitoring application (Munin, 2012).

3.3.4 Waveform generator interface and triggers

A front panel 26-pin LVPECL Sync connector includes sample clock, sync, PPS, and gate I/O signals. In addition to the LVPECL Sync Bus signals, the 7150 accepts an external sample clock and PPS input signals supplied through front panel SMC connectors. Also, two optional TTL Sync/Gate input signals are available through the Sync connector. Further, some triggers are available from the waveform generator card over the SCSI connector. Signals from either the LVPECL Sync Bus, the external sample clock input, the onboard oscillator or SCSI connector can be selected as the timing source for the A/D converters. Gates are used to enable writes to the FPGA FIFOs. The Universal Serial Bus (USB) interface of the SBC enclosure is used to program the waveform generator software. On the other hand, the radar system triggers about the transmit state information and PRT timing are provided to the DRX over the SCSI connector from the waveform generator (WGN). The following explains these triggers (Table 3.1):

ACQ_TRIG

This differential signal indicates the begining of the PRT period. The digital receiver begins acquiring data when triggered by this signal. The signal is active high on the resulting single-ended signal and should be atleast 10 ns.

PRF_SEL

This differential signal indicates the selection of the PRF for the current PRT period.

The digital receiver appends the data packets corresponding to the current PRT period with this selection and passes it to the moment server. A value of '0' on the resulting single-ended signal will indicate the lowest of the two PRTs.

XMIT_STATE_H

This differential signal indicates the state of H-channel transmitter for the current PRT period. The digital receiver appends the data packets corresponding to the current PRT period with the state of the current H-channel transmitter and passes it to the moment server. A value of '0' on the resulting single-ended signal will indicate that the transmitter has not been fired.

XMIT_STATE_V

This differential signal indicates the state of V-channel transmitter for the current PRT period. The digital receiver appends the data packets corresponding to the current PRT period with the state of the current V-channel transmitter and passes it to the moment server. A value of '0' on the resulting single-ended signal will indicate that the transmitter has not been fired.

SEQ_RESET

This differential signal indicates if the current PRT period is a part of a preset sequence (such as a phase coding sequence). The digital receiver appends the data packets corresponding to the current PRT period with this information and passes it to the moment server.

SPARE00-10

These differential signal lines are reserved for future use and, unless otherwise noted, digital receiver would ignore these signals. In the WiBEX radar system, some of these lines are used to provide the antenna position information, IRIG-B and 1PPS signal.

3.3.5 Antenna decoder interface

The digital receiver card can interface with the control and communications in the pedestal in two ways. The first, as in the WiBEX radar system, is acquire the

Table 3.1: Pin and signal description of the DRX-WGN interface

Signal Name	DRX FPGA LVDS Bus Pin	PMC P4 Pin	WGN FPGA I/O
ACQ_TRIG	LVDS2_IN_P(0)	2	IO00_P
	LVDS2_IN_N(0)	4	IO00_N
SPARE00	LVDS2_IN_P(1)	6	IO01_P
	LVDS2_IN_N(1)	8	IO01_N
SPARE01	LVDS2_IN_P(2)	10	IO02_P
	LVDS2_IN_N(2)	12	IO02_N
SPARE02	LVDS2_IN_P(3)	14	IO03_P
	LVDS2_IN_N(3)	16	IO03_N
PRF_SEL	LVDS2_IN_P(4)	18	IO04_P
	LVDS2_IN_N(4)	20	IO04_N
SPARE03	LVDS2_IN_P(5)	22	IO05_P
	LVDS2_IN_N(5)	24	IO05_N
SPARE04	LVDS2_IN_P(6)	26	IO06_P
	LVDS2_IN_N(6)	28	IO06_N
XMIT_STATE_H	LVDS2_IN_P(7)	30	IO07_P
	LVDS2_IN_N(7)	32	IO07_N
XMIT_STATE_V	LVDS2_OUT_P(0)	34	IO08_P
	LVDS2_OUT_N(0)	36	IO08_N
SEQ_RESET	LVDS2_OUT_P(1)	38	IO09_P
	LVDS2_OUT_N(1)	40	IO09_N
SPARE05	LVDS2_OUT_P(2)	42	IO10_P
	LVDS2_OUT_N(2)	44	IO10_N
SPARE06	LVDS2_OUT_P(3)	46	IO11_P
	LVDS2_OUT_N(3)	48	IO11_N
SPARE07	LVDS2_OUT_P(4)	50	IO12_P
	LVDS2_OUT_N(4)	52	IO12_N
SPARE08	LVDS2_OUT_P(5)	54	IO13_P
	LVDS2_OUT_N(5)	56	IO13_N
SPARE09	LVDS2_OUT_P(6)	58	IO14_P
	LVDS2_OUT_N(6)	60	IO14_N
SPARE10	LVDS2_OUT_P(7)	62	IO15_P
	LVDS2_OUT_N(7)	64	IO15_N

bit-encoded LVDS signal over the SCSI connector. A logic '0' is encoded as a bit-sequence of 1000 while a logic '1' is encoded as a sequence of 1000. There are 48 bits per frame with each frame separated by a long time period. The azimuth is encoded in the first 16-bits while the elevation is encoded in the second group of 16-bits. Other bits are unused. The DRX FPGA implements a state machine to decode the antenna position information and sends it in the data packet. This approach ensures minimum latency in the position information with the high-speed data sampling.

The second method, as in the D3R system, is to interface the DRX SBC with the Orbital Systems (Orbital Systems, 2012) pedestal electronics on an RS-422/232 interface. The position information is then decoded in the host computer software and is stamped on the acquired data. This approach introduces latency in the antenna position (since communciation with the pedestal is over the network) with respect to the digital receiver time series.

3.3.6 GPS decoder interface

Similar to the antenna position, the GPS receiver signals can also be interfaced with the DRX in two ways: the IRIG-B (Inter-Range Instrumentation Group B) time code over the SCSI connector (as in WiBEX) which is eventually decoded in a state machine within the Processing FPGA or National Marine Electronics Association (NMEA) 0183 protocol in the SBC software (as in D3R) over the RS-232 interface. The D3R system employs the NAVSYNC CW25 GPS receiver (CW25) which is a small size GPS module specifically designed for use in weak signal GPS environments while maintaining all the features of a standard GPS solution, such as high accuracy. When connected to the RS-232 interface, the device is synchronized with the available Network Time Protocol (NTP) server using the open-source GPS daemon (`gpsd`) software (Raymond, 2012). This software will sit between the GPS device and the NTP daemon (`ntpd`), making both the PPS signal and the NMEA 0183 data available to NTP daemon through a pair of shared memory (SHM) devices.

3.4 Summary

This chapter described the general principle of operation of the hardware which will be used to program the digital receiver functions of the solid-state transmitter. With all possible information available from different subsystems, this digital receiver hardware should now be configured for multi-channel processing in the Processing FPGA. The Xilinx Virtex-5 SX95T model of Pentek 7150 is chosen for the Processing FPGA since this device is the richest in available on-chip signal processing resources. In the next chapter, the design of the multi-channel digital receiver has been described for this FPGA.

CHAPTER 4

MULTI-CHANNEL DIGITAL RECEIVER

All the functions related to the digital receiver are realized on a high density Xilinx Virtex-5 SXT95 FPGA available on the digital receiver board. The receiver includes four 200 MHz 16-bit analog to digital converters, the compute FPGA and a PCI interface FPGA in a PMC form-factor. The PMC is mounted on a cPCI chassis over which it transfers the I/Q output data to a single-board computer. The digital receiver implements the quadrature modulation of the sampled complex envelope of the IF signal, digital down-conversion from the IF to the baseband data rate and correlation processing.

The digital receiver is required to process all the range gates for I/Q data corresponding to each of the subpulse for both H and V channels. A traditional implementation of this 12-channel processing chain, i.e. allocating separate lters dedicated to each of the subpulses, would mandate use of excessive multipliers than the resources of the XC5VSX95T device can offer. This chapter describes the design of A multichannel design of the processing chain, wherein each lter - clocked higher than the input sample rate - shares the data for different subpulses, is chosen for implementation of the most of the functions of the digital receiver.

4.1 User requirements and design constraints

Apart from the user requirements discussed in previous chapters, the design of the multi-channel digital receiver is affected by a few other factors, such as,

- The multi-channel digital receiver should be able to perform subsampling of the IF data at the ADC level.
- The receiver should be able to simultaneously process all twelve channels (=3 subpulses x 2 (H, V polarizations) x 2 (I, Q samples)) for all the range gates through a cascade of decimation filters.
- The option of Built-In Self Test should be included to allow the test of digital performance of the entire system.
- The clock and timing circuit of the receiver should clock at 200 MHz.
- The receiver should be able to provide raw time series data with and without pulse compression at a rate of 10 MHz with capability to resample at a rate as low as 1 MHz.
- The entire system should be programmable and scalable to allow easy upgrade to more features and channels.

The Pentek 7150 board is available with several options for the Processing FPGA from Xilinx. The Virtex 5 SX95T device is chosen for the multi-channel digital receiver considering the plenty of signal processing resources available on the chip. In simple terms, the digital receiver configured on this device implements a quadrature modulation of the sample IF signal, downconverts the data to the baseband rate while filtering out the subpulses and performs correlation processing.

4.1.1 Xilinx Virtex 5 SX95T FPGA

Most advanced system designs require the programmable strength, low power features and savings in real-estate offered by FPGAs. The Virtex-5 family of Xilinx FPGAs (Xilinx Inc., Feb 6, 2009) offers a high-end solution for addressing the needs of high-performance logic designers, high-performance DSP (Digital Signal Processor)

designers, and high-performance embedded systems designers with plenty of logic, DSP, hard/soft microprocessor and connectivity capabilities. Built on a 65-nm state-of-the-art copper process technology, Virtex-5 FPGAs are a programmable alternative to custom ASIC technology. Using the second generation ASMBL (Advanced Silicon Modular Block) column-based architecture, the Virtex-5 family furnishes five distinct platforms (sub-families): LX, LXT, SXT, TXT, and FXT. Each platform contains a different share of features to address the needs of a wide variety of advanced logic designs.

In addition to the most advanced, high-performance logic fabric, Virtex-5 FPGAs contain many hard-IP system level blocks, including highly configurable 36-Kbit block RAM/FIFOs, advanced 25 x 18 DSP slices, SelectIO technology with built-in digitally-controlled impedance, ChipSync source-synchronous interface blocks, system monitor functionality, enhanced clock management tiles with integrated DCM (Digital Clock Managers) and phase-locked-loop (PLL) clock generators, and advanced configuration options. Additional platform dependant features include power-optimized high-speed serial transceiver blocks for enhanced serial connectivity, PCI Express compliant integrated Endpoint blocks, tri-mode Ethernet MACs (Media Access Controllers), and high-performance PowerPC 440 microprocessor embedded blocks. These features allow advanced logic designers to build the highest levels of performance and functionality into their FPGA-based systems. Virtex-5 SXT is designed for high-performance signal processing applications with advanced serial connectivity. The Processing FPGA XC5VSX95T is a Virtex - 5 SXT family device with an intermediate range of resources. Table 4.1 quantifies the relevant available features on this device. The total number of DSP48E slices are 640 (none of which has been used in the default Pentek design). The default Pentek design occupies about 50% of the logic leaving only 20% for the user design.

Table 4.1: List of available resources on the Virtex-5 SX95T device

Resource	**Value**
Logic Slices	14,720
DSP48E Slices	640
Total distributed RAM	1,520 Kb
Total Block RAM	8,784 Kb
Clock Management Tiles	6 (= 6 PLLs and 12 DCMs)
Rocket IO Transceivers	16
f_{max}	550 MHz

4.2 Design philosophy

The cost of the filter chain in the digital receiver as shown in Figure 4.1 for all twelve channels is very expensive (Table 4.2) considering that each subpulse would require processing through a cascade of decimation filters and a pulse compression filter with variable number of taps. Given the resource constraints on the Processing

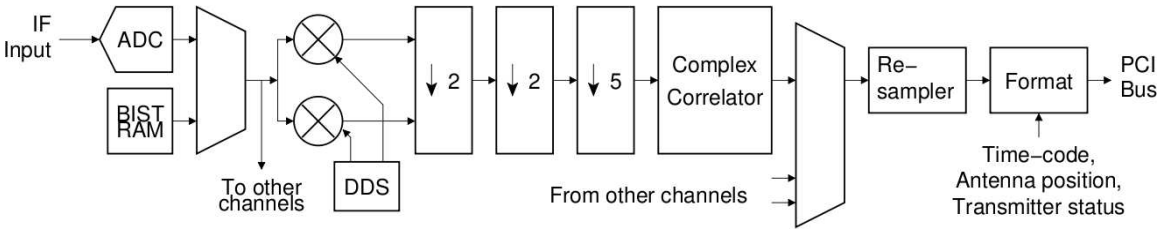

Figure 4.1: Block diagram of frequency-diversity digital receiver. Processing for only one sub-pulse is shown. Two such receivers are implemented, one for each polarization channel.

FPGA, the multi-channel receiver design clocks each filter higher than the input sample rate. This causes the subpulses to share the same resource in one clock cycle. Figure 4.1 shows the major components of the digital receiver design implemented on the XC5VSX95T device. A high SFDR (95 dB) multi-channel direct digital synthesizer (DDS) is employed for the quadrature modulation of the sampled IF data. A cascade of the half-band lters and a low pass FIR lter decimates the I/Q data so obtained. Polyphase implementation of these lters further reduces the usage of DSP48E slices. The matched ltering of the I/Q data is performed by single-rate

Table 4.2: Cost of implementation of the filter chain for one subpulse channel. XC5VSX95T offers 640 25 18 bits DSP48E Slices. The percentage of the DSP48E slices occupied on the device for each implementation is noted in the last row.

Filter	**Taps**	**Mults (MATLAB)**	**DSP48Es (FPGA)**
Halfband Filter 1	23	13	4
Halfband Filter 2	23	13	4
Decimate-by-5 Filter	255	205	13
40 μs Correlation Filter	400	401	22
20 μs Correlation Filter	200	201	12
Total		828 (130 %)	53 (8 %)

FIR lters clocked higher than the input sample rate. This entire design consumes close to 400 DSP48E slices on the FPGA. The MATLAB cost of the traditional design of the filter chain exceeds the available resources on the XC5VSX95T device (Table 4.2)

.

It is obvious that the design philosophy for the digital receiver must capitalize on using the multi-channel high clock rate versions of filter design. Figure 4.2 shows this design where every filter is clocked at 400 MHz to process multiple subpulse channels. The details of the clock and timing are not shown in this diagram. After every processing stage of a decimation filter, the sample rate decreases. The channels are then multiplexed and regrouped for the next stage of the filter chain so that the overall sample rate is still 200 MHz.

The MATLAB Fixed-Point Toolbox allows the user to estimate the bit growth after every processing stage in the digital receiver. The total number of bits and the number of fractional bits at every output stage is shown in Figure 4.2 where 's' denotes the signed numbers. The total number of bits should however not exceed 32 since the PCI bus can be 32-bit only. The subsequent sections deal with the details of the implementation.

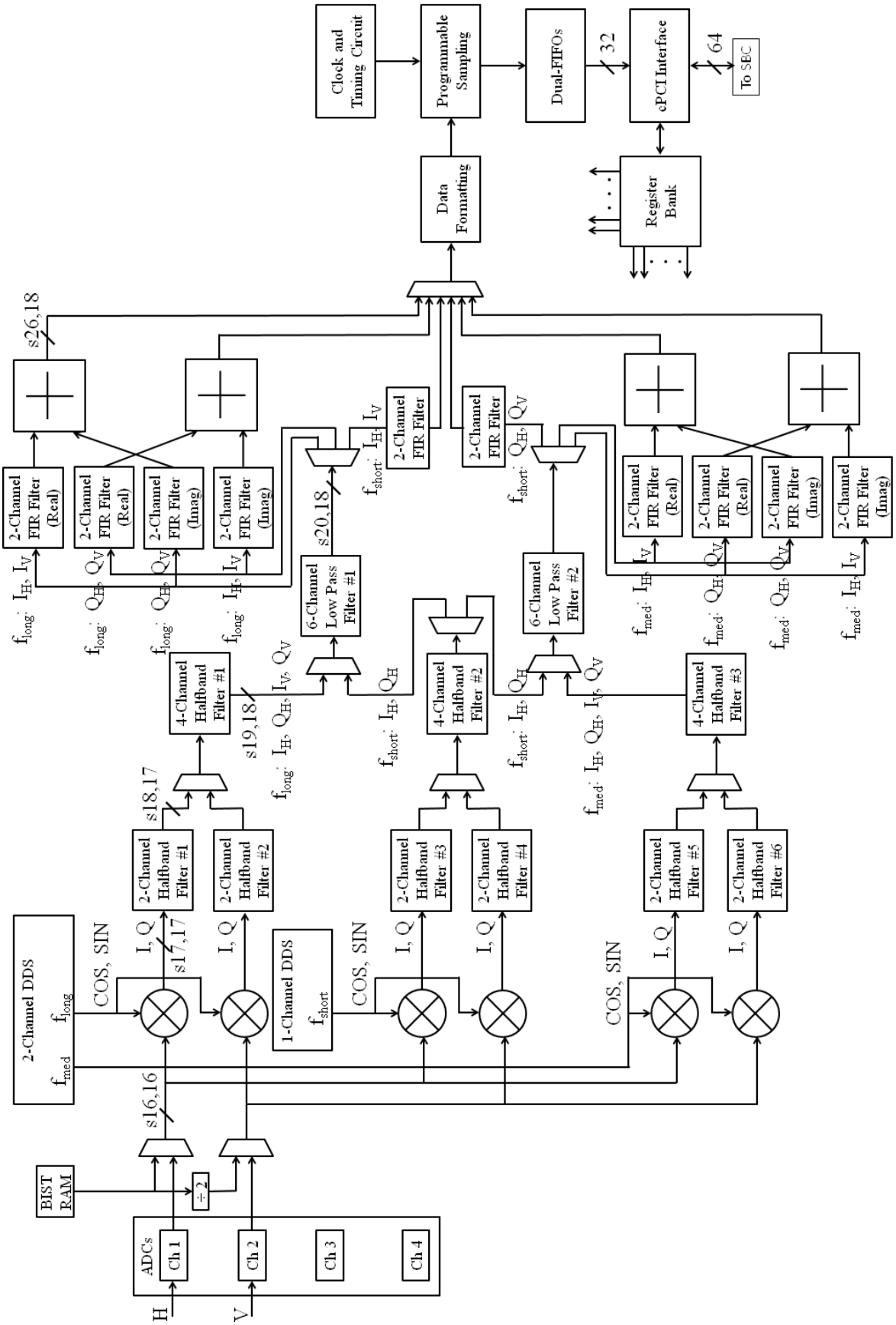

Figure 4.2: Block diagram of the multi-channel digital receiver.

4.2.1 IF digitizer

The 7150 board is designed for a maximum input sampling frequency of 200 MHz. The front end accepts four full scale analog HF or IF inputs on front panel SMC connectors at +8 dBm into 50 ohms with transformer coupling into four Texas Instruments ADS5485 200 MHz, 16-bit A/D converters (ADCs). The digital outputs are delivered into the Processing FPGA for signal processing or for routing to other module resources. The ADC outputs are usually timed for the double data rate (TI, Oct 2008) which can be easily converted back to the normal data rate using Xilinx primitives.

The IF digitization of the frequency-diversity receiver employs IF subsampling interpreting the Nyquist criterion for band-limited signals. Since the IF stage frequency remains unused as part of the signal extraction, there is no requirement to preserve it while sampling the data. The Nyquist criterion for the IF (which requires sampling rate twice the IF) can actually be violated as long as Nyquist criterion for the bandwidth of complex envelope is obeyed. The A/D converter's sample rate is selected to be less than the signal's center frequency to intentionally alias the center frequency. Since Nyquist criterion is being intentionally violated, the analog signal must be conditioned to prevent multiple frequency intervals from aliasing to the same frequency location as the desired signal component will alias. Therefore, the three-pulse frequency diversity signal at IF frequency of 140 MHz when sampled at 200MHz would produce an inverted image at 60 MHz (Figure 4.3). The signal bandwidth of approximately 35 MHz (with 15 MHz separation between the subpulses form the center frequency) ensures that these two images are not aliased. The digital receiver then extracts the signal centered at 60 MHz.

Further, the ENoB for ADS5485 devices is stated as 12.1 bits (TI, Oct 2008). As

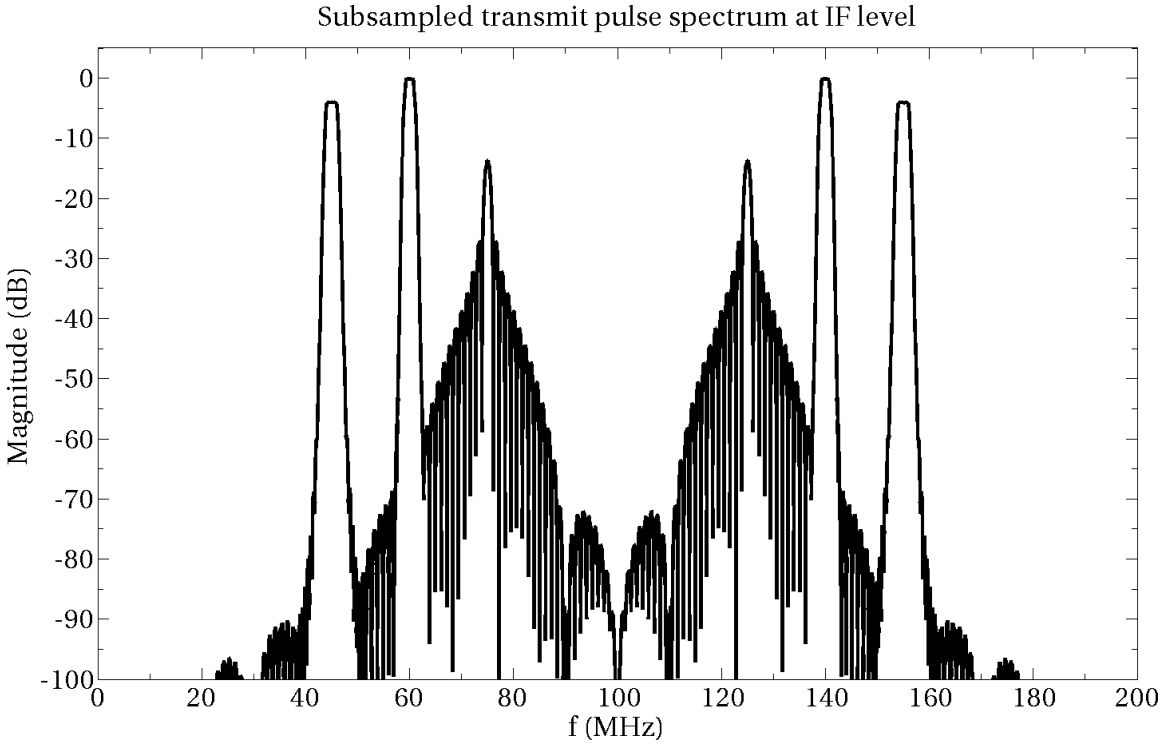

Figure 4.3: The IF subsampling of the frequency diversity waveform. The signal centered at 140 MHz is sampled at 200 MHz. This produces an image at 60 MHz.

explained in Chapter 2, this gives the digital receiver's dynamic range as,

$$DR(dB) = -1.76 + 6.02(12.1) + 10\log_{10}\left(\frac{200/2}{1}\right) \tag{4.1}$$

$$= 91.08 \tag{4.2}$$

4.2.2 Clock and timing

The digital receiver front panel LVPECL Sync connector provides clock, sync, PPS, and acquisition trigger input/output signals. This connector also provides two TTL Gate/Sync inputs. The front panel has two coaxial SMC receptacles for input of an external sample clock and PPS signal. The LVDS connections from the SCSI interface can also be used for the acquisition trigger or PPS. Each FIFO gate may be programmed as a trigger using the ADC FIFO Control Registers. In Trigger mode, the gate is generated after a desired polarity logic transition on the external gate source or register write, and the resulting gate continues either indefinitely (Hold

mode) or for a programmed number of ADC samples (Trigger Length). At any time the triggered gate may be asynchronously disabled by a control register write. This functionality is helpful in designing the Dual-FIFO interface for data acquisition as expalined later in the chapter. The digital receiver can be programmed to clock on either the onboard internal clock or external clock from the SMC connectors. It can also be programmed to accept triggers from either from the SMC input, LVDS input or an internally generated signal.

4.2.3 Digital down-converter

A Digital Down Converter (DDC) translates a passband signal comprising one or more radio or intermediate frequency (RF or IF) carriers to one or more baseband channels for demodulation and interpretation. This is achieved by mixing the signal with a numerically controlled oscillator (NCO) output to shift the signal spectrum from the selected carrier frequencies to baseband, further decimating the signal to reduce the sample rate, and filtering to remove adjacent channels, minimize aliasing, and maximize the received signal-to-noise ratio (SNR). The DDC input signal has a relatively high sample rate, generally, the output sample rate of an ADC (= 200 MHz) which samples the detected signal (often after analog frequency translation and pre-processing), while the output is a much lower rate, for example, the data rate of PCIe bus to facilitate data transfer at reasonable speeds.

The mixing is performed by multiplying the input sampled signal by the quadrature outputs of a Direct Digital Synthesizers (DDS). The multi-channel digital receiver employs two DDS modules one clocked at 400 MHz with two-channel outputs and the second single-channel output module at 200 MHz (Figure 4.4). The clarity of the sinusoid generated by the DDS is crucial to the spectral purity of the overall DDC output, as the output signal is limited by the noise floor of the DDS. This noise is caused by both the phase and amplitude quantization of the frequency synthesis process in the look-up table of the NCO module. A phase dithering method

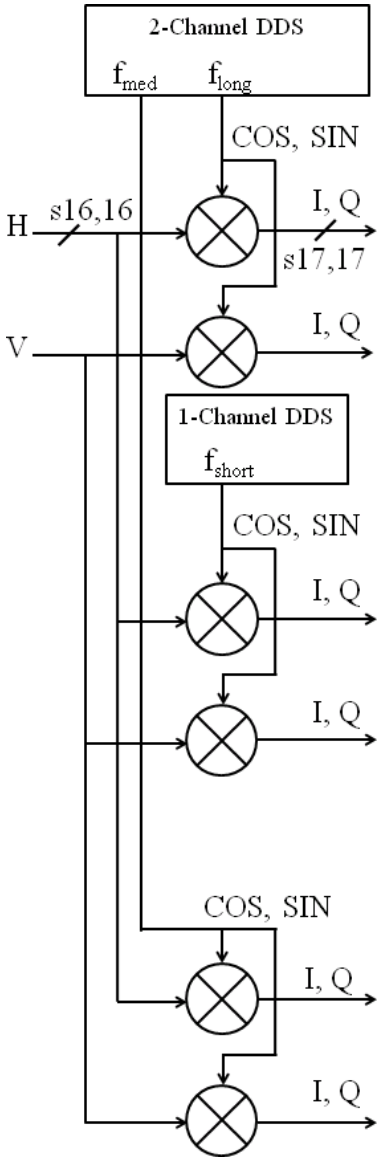

Figure 4.4: The multi-channel digital receiver uses two DDS modules for the digital downconversion process.

is often used to improve the spurious-free dynamic range (SFDR) of the generated sinusoidal waveform by 12 dB without increasing the depth of the look-up table, by removing the spectral line structure associated with conventional phase truncation waveform synthesis architecture. Although the dithered DDS has a multiplier-free architecture, it can consume too many block RAMs for the storage of the sampled sinusoidal waveform in the high SFDR setting, which results in the deterioration of the design speed. A Taylor series corrected method can provide even higher SFDR (up to 120 dB) using the same depth of sinusoidal look-up table. The multi-channel digital receiver implementation has a very high SFDR of 95 dB with phase-dithered noise shaping option. Additionally, the on-board ADCs are also configured to provide phase-dithering in order to increase the SFDR without utilizing more resources. The MATLAB fixed-point implementation and the Hardware Description Language

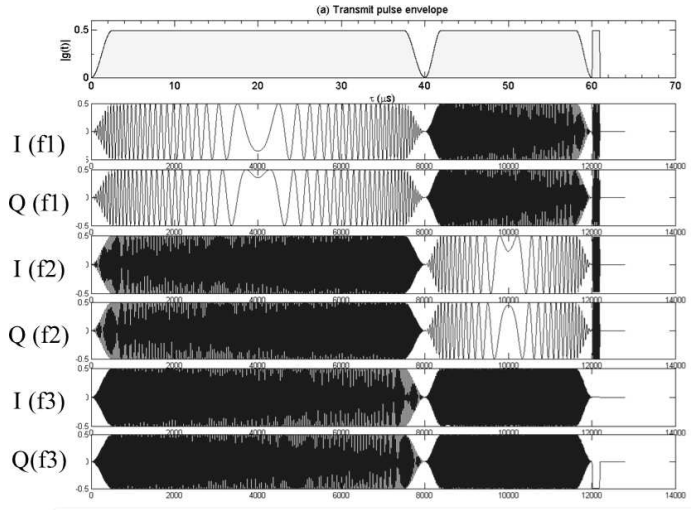

Figure 4.5: The MATLAB Fixed-Point simulation results of the digital downconversion chain.

(HDL) simulation of DDC stage outputs are respectively shown in Figures 4.5-4.6. They show identical results for the long (f_1), medium (f_1) and short (f_3) subpulses.

4.2.4 DDC filter design

The downconversion process is followed by a cascade of downsampling FIR filters. The main functions performed by FIR filters in DDC circuits are image anti-aliasing

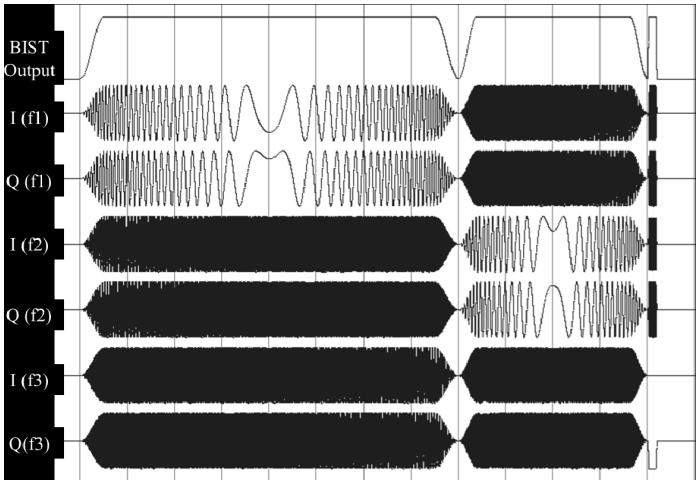

Figure 4.6: The HDL simulation results of the digital downconversion chain.

for decimation and channel selection for received data. There are several approaches to implement the DDC filters depending on the performance desired and available resources.

4.2.4.1 CIC-CFIR cascade

One of the most common DDC filter implementation is the Cascaded Integrator Comb (CIC) filter. CIC filters (or Hogenauer filters (Hogenauer, 1981)) are a unique class of digital filters in the sense that they present a computationally efficient way of implementing band-limited low-pass filters for image-rejection in high data-rate designs. CIC filters use only delays and summation units and eliminate the multiplication operations as required in an FIR filter. The filters are constructed from Integrator and Comb filter stages (Figure 4.7). CIC filters can efficiently perform either decimation or interpolation, with two complementary structures being employed to implement these functions. Decimation requires a cascade of a number of integrator units, followed by a down-sampling stage and finally a cascade of the comb filter units. Conversely, interpolation cascades several comb filters with an up-sampler and several integrators. A rate change is always involved in CIC filtering, and the filter response exhibits linear phase.

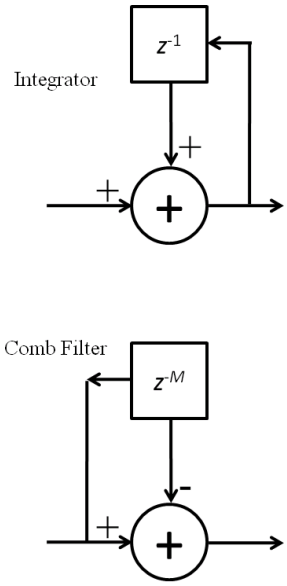

Figure 4.7: The CIC building blocks.

The disadvantage of using the CIC filters is the "passband droop" in its frequency response. However, in a multi-channel system with a pulse compression end-stage, a flat passband in the magnitude frequency response is desirable to prevent signal distortion. The sinc-like frequency response of CIC filters can. therefore, decay appreciably even within the passband when there are many CIC stages or a high rate change. As a result, it is necessary to cascade the CIC filter with an FIR filter which compensates for this droop with an inverse-sinc frequency response. This compensator-FIR (CFIR) filter requires additional resources on the FPGA necessitating the use of multipliers which CIC filters offered to eliminate. The multichannel digital receiver, therefore, avoids the use of CIC stages and instead utilizes the efficient polyphase implementation of FIR filters on Xilinx FPGAs.

4.2.4.2 FIR decimation filter cascade

The multi-channel DRX makes use of a cascade of three multi-rate filters (Figure 4.8). The first two stages are decimate-by-two halfband filters followed by a polyphase decimator. The half-band filters have the property of performing decimation without decreasing the dynamic range of the digitized signal (by preserving

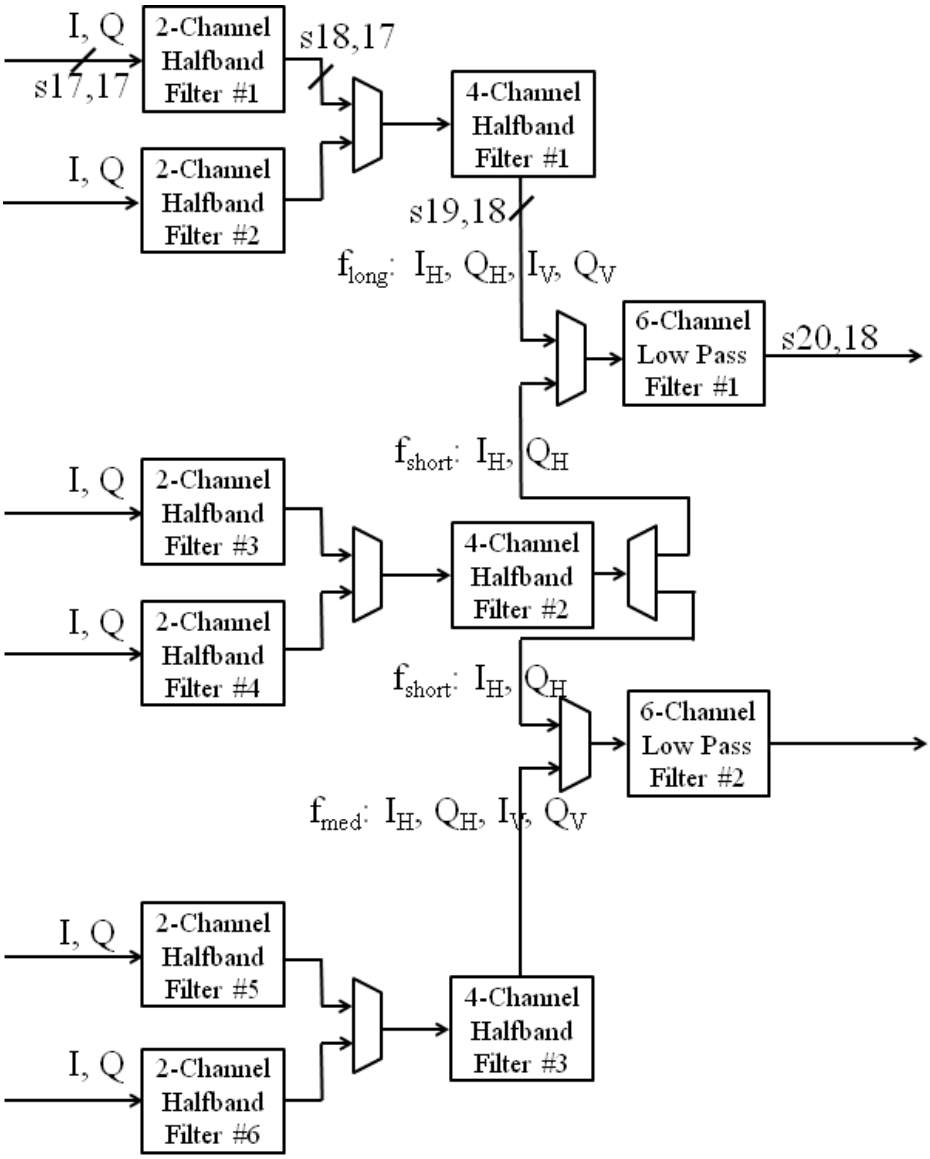

Figure 4.8: The DDC decimation filters as implemented in the multi-channel digital receiver.

the level of quantization noise). The zero-phase FIR half-band filters have the linear phase property. The impulse response of the half-band filters is given by

$$h(n) = ch^*(-n) \tag{4.3}$$

with $|c| = 1$. Therefore, the number of coefficients in a half-band filter is one less than a multiple of four (Vaidyanathan, 1993). Further, every alternate coefficient of the half-band filter is zero. A symmetric half-band filter can also be configured as a polyphase filter thereby requiring even fewer multipliers. Therefore the FIR implementation of halfband filters would save significantly more logic than the CIC filter. The final decimation-by-5 stage is implemented as a polyphase filter which reduces the number of multipliers by a factor of five compared to the conventional FIR filters. All filters, implemented in multi-channel modes, have a stopband attenuation of 80 dB and passband ripple of 0.01 dB. The HDL outputs of the filters for all three subpulses is shown in Figure 4.9.

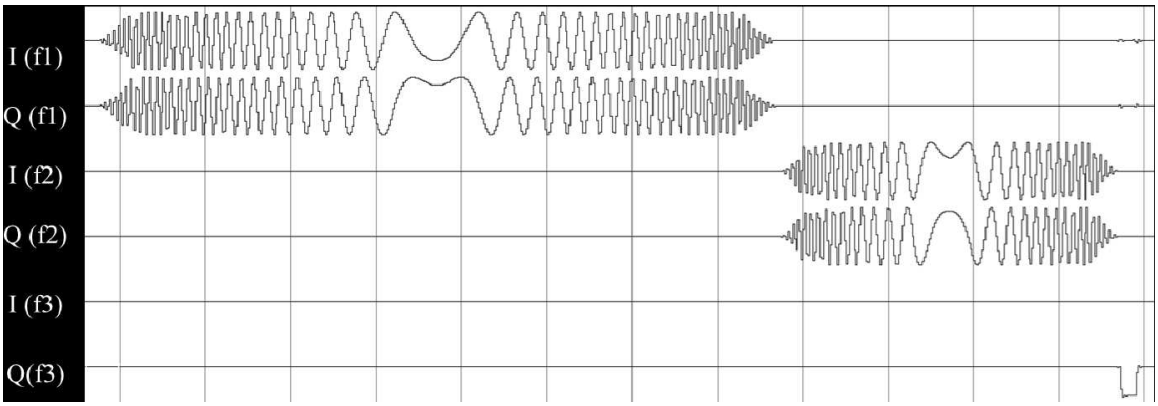

Figure 4.9: The HDL simulation outputs of the DDC decimation filters.

4.2.5 Pulse compression filter

In practice, a pulse compression filter is a complex coefficient filter. If $A + jB$ represents the complex pulse compression filter and the complex input samples are

given by $I_{in} + jQ_{in}$, then the complex output samples are given by:

$$I_{out} + jQ_{out} = (I_{in} + jQ_{in}) * (A + jB) \tag{4.4}$$

$$= (I_{in} * A - Q_{in} * B) + j(I_{in} * B + Q_{in} * A) \tag{4.5}$$

Therefore a complex filtering operation is equivalent to four real filters which produce the outputs $I_{in} * A$, $Q_{in} * B$, $I_{in} * B$ and $Q_{in} * A$. These outputs can now be rearranged in the hardware to produce the equivalent output of the complex filter. This approach is illustrated in the Figure 4.10. Figure 4.11 compares the digital output of the pulse compression stage with that of the ADC mode output for an example waveform.

4.2.6 Resampling, data formatting and dual-FIFO

The data format and resampling module is essentially a multiplexer. The inputs of the mux are all the words that are required to be passed to the dual-FIFO. There is a separate control line for each word. For each range gate, the I and Q samples for every subpulse and polarization must be selected while the PRT count and clock tick words are selected only once every instance of the acquisition trigger. Before pushing every word in the FIFO, it is formatted with a unique four-bit header. These headers are used for data-verification in the SBC firmware.

The ADC trigger length register keeps the count of the number of words to be pushed in the FIFO. This trigger is multiplexed with another gate which controls the resampling frequency. The current resampling frequency is programmed at 1 MHz for the raw time series data. A dual-FIFO structure is used to buffer the data for a particular acquisition cycle. The data formatting module pushes the data in the FIFO after appending the appropriate headers. The read-write controls of the FIFO are controlled by the DMA-engine through the SBC DRX firmware (Figure 4.12). Since the data reading speed of the DMA and the data writing rate of the DRX differ, the data integrity cannot be maintained by a single FIFO. In the dual-FIFO design, two FIFOs are used alternately by data formatting module and the DMA engine

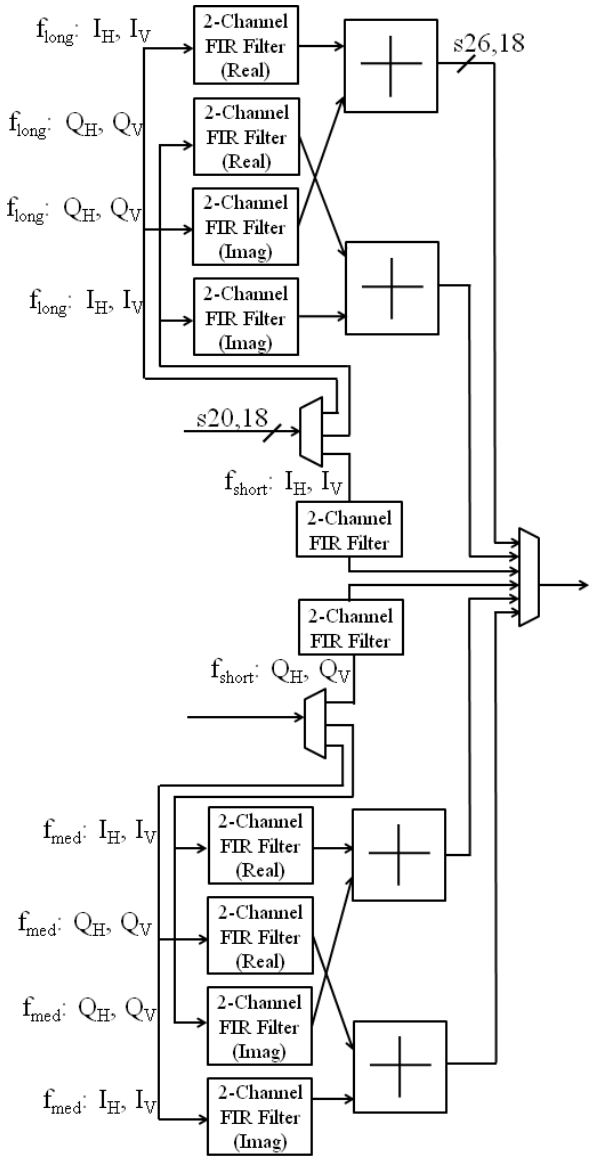

Figure 4.10: The correlation (pulse compression and matched) filters as implemented in the multi-channel digital receiver.

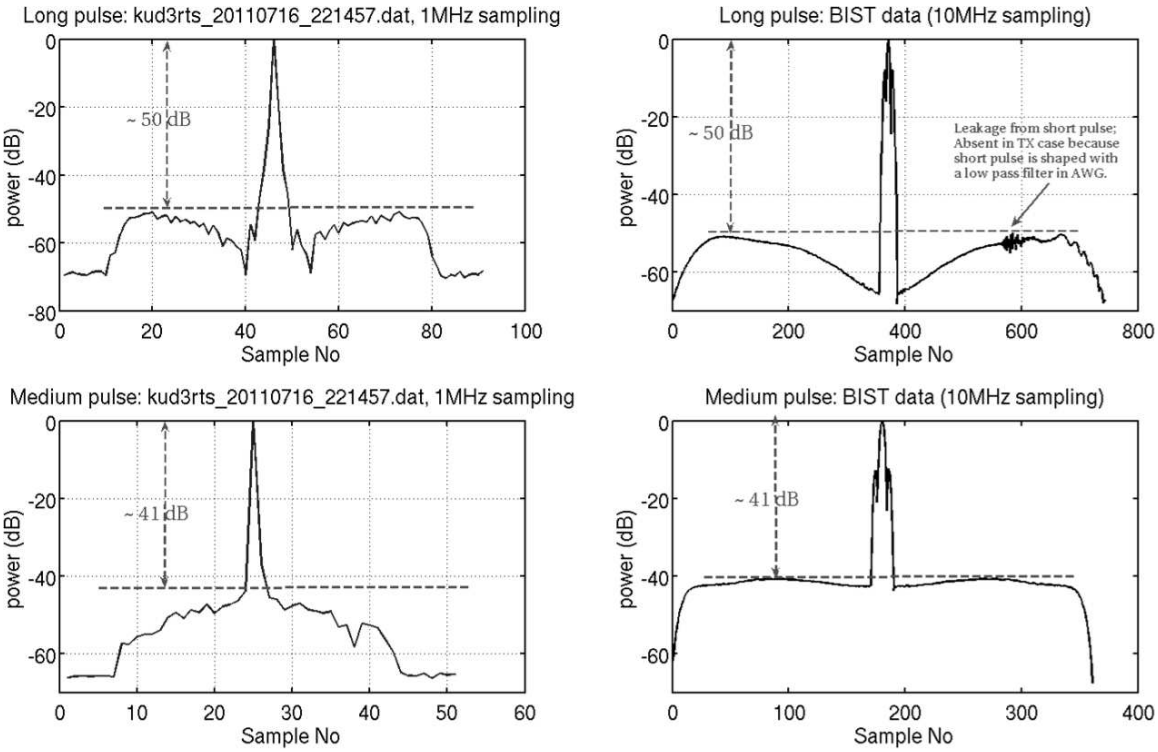

Figure 4.11: Comparison of the pulse compression filter outputs of the DRX in BIST and ADC modes.

to write and read the data exclusively at different rates. After each read operation on a FIFO, the respective FIFO is asynchronously flushed out just before the write operation begins. The DRX firmware employs multiple-DMAs for the data transfer.

4.3 Configurability and programmability

The entire digital receiver hardware can be programmed through a large bank of 64-bit registers each of which is uniquely accessible to the DRX firmware. The ID Readout registers give out information of the hard-coded versions of the FPGA images. The TWSI registers are used to store information about the sensor data and can be queried for the latest sensor datalog. The registers for Master Bus Control, Sync Generators and PPS/Gate Controls are used to configure various options for clock and timing circuits. The ADC registers store information on enabling the A/D dither, trigger length, trigger status, FIFO empty-full levels and data packing. There

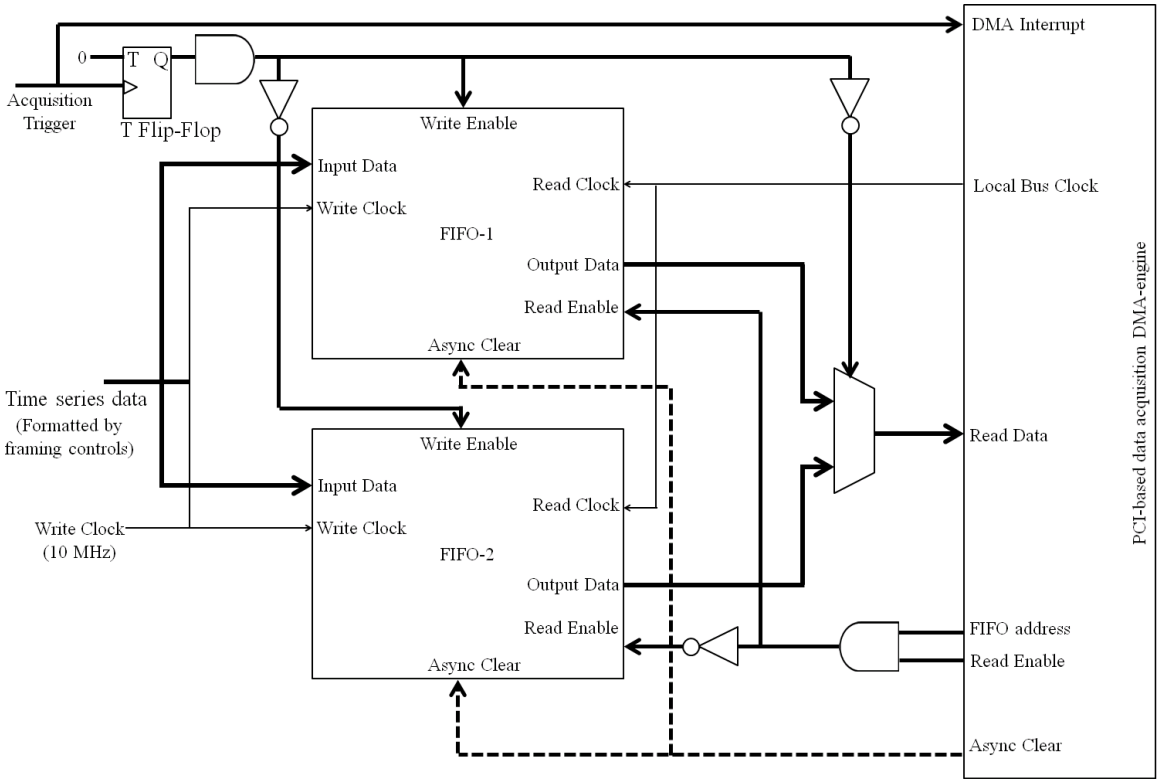

Figure 4.12: The dual-FIFO interface of the DRX consists of two FIFOs with mutually exclusive read and write cycles controlled by the DMA-based acquisition firmware. During one acquisition cycle, when one of the FIFOs is being buffered with the data, the other FIFO is being read by the DMA engine. At the end of the read cycle, this FIFO is cleared and enabled for writing.

are separate registers for setting the DDS frequencies, BIST, PRTgeneration controls and DDC filter coefficients.

The single-board computer DRX firmware sets all these controls before enabling the data transfer from the digital receiver using a DMA-based acquisition over a PCI interface. The acquisition thread sends the data in a circular buffer where it is queues to a socket server thread which serves connections to the signal processors. The acquisition thread also continuously keeps track of the PRT counts and clock ticks to check for any data loss.

4.4 Summary

The multi-channel digital receiver highlights the significance of using high-end FPGAs to achieve scalability, programmability and performance in a resource-constraint environment. This chapter presented results from the simulation and BIST mode for various processing stages of the digital receiver. This receiver was first deployed for the D3R system, for which its field results are listed in Chapter 7. The I-Q time series data collected by the receiver SBC is sent to the signal processor for computation and interpretation as described in the next chapter.

CHAPTER 5

PROCESSING MODES AND ALGORITHMS

There are several modes to process the digitized and filtered I and Q samples of the weather signals in a solid-state transmitter radar. The traditional pulse-pair technique (Bringi and Chandrasekar, 2001, p. 279-281) is employed to first estimate the moments from each channel. All other algorithms must then process data from all the channels and provide a single range profile of all products culled from the twelve channels of the digital receiver. The use of non-uniform sampling causes additional calculation of several products such as mean velocity, spectrum width and LDR and facilitates research for compatible clutter filtering techniques. The signal processor design should be able to also interface with the radar display and moment archiver.

This chapter describes the operational signal processor design, its potential upgrades and research applications. Some common features are described first, followed by descriptions of the unique techniques for improving the data quality.

5.1 Software and network architecture

As described in Chapter 4, the host computer acquires the I-Q data generated by the digital receiver and stamps it with the antenna position and the GPS timestamp over the cPCI bus. This I-Q data can now be processed and distributed over the Ethernet link archiving, product generation, display and playback. The high-end general purpose processors are employed for the exchange, computation and dissemination of the data using TCP/IP protocol. Figure 5.1 shows the framework for the signal

processing network which uses Intel Xeon Octal-Core processors communicating with each other over the Gigabit Ethernet link. Each of these processors is two-way hardware multi-threaded implying availability of total 16 central processing unit (CPU) cores for parallel processing. This flexible network architecture allows for access of data to multiple clients at every stage of computation. The following sections discuss functions of these servers - each of which operates on Unix operating system (mostly CentOS) - in detail.

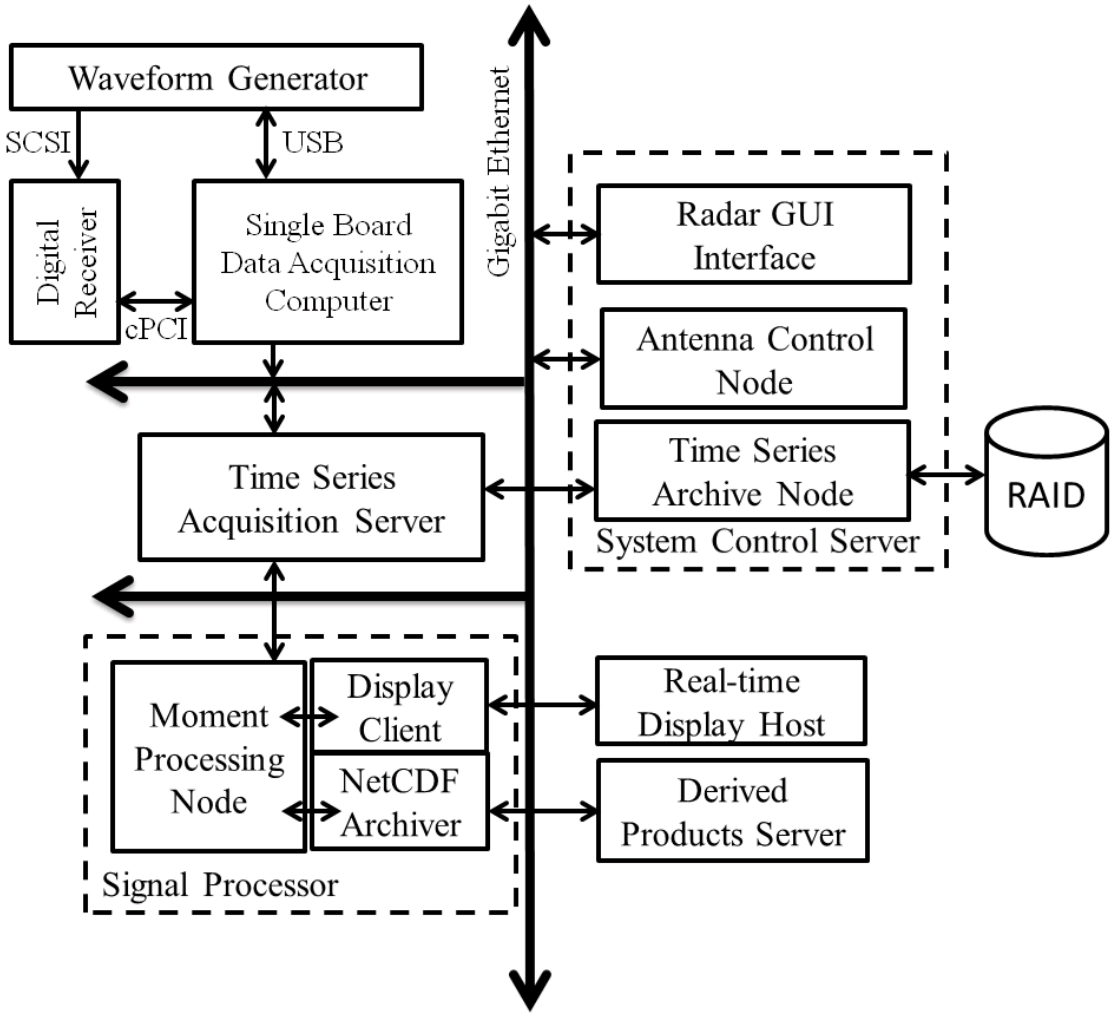

Figure 5.1: Framework for the signal processing software. The comunication between most of the subsystems is through Gigabit Ethernet link (solid dark line). In practice, this is accomplished through a network switch.

5.1.1 Time series acquisition and dissemination

This digitized data should be processed to generate the meteorological products by the moment processor. At the same time, the entire raw I-Q data must also be archived. If the digital receivers are mounted as movable modules above the slip-ring, the usual fibre optic link that connects the host computer to the servers down is often unable to handle this massive volume of data for multiple clients. The Time Series Acquisition and Dissemination Server is employed to acquire the data from the digital receiver via the fibre optic link over the slip-ring and then making it available to multiple clients. This way, the acquisition of the raw I-Q time series is minimized to only one client bringing down the overall data rate over the fibre-optic link. The

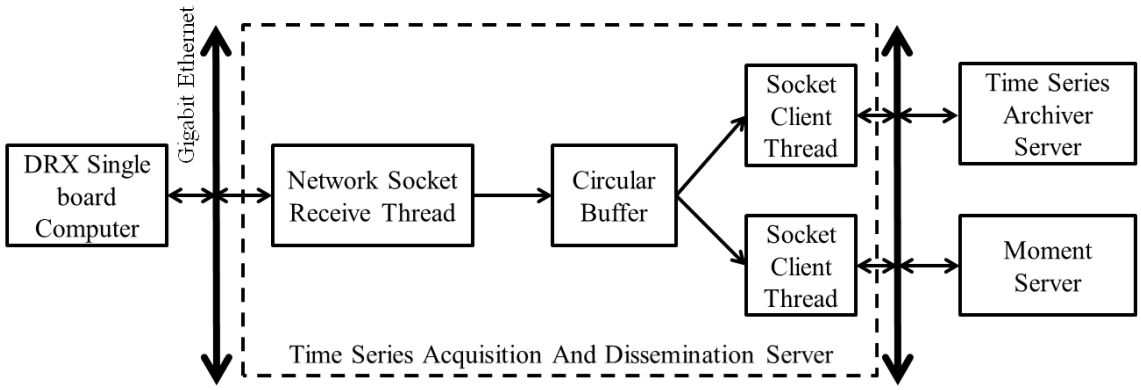

Figure 5.2: Conceptual diagram of time series acquisition and dissemination process.

Time Series Acquisition and Dissemination Server acts as a socket client to the digital receiver host computer while acquiring the time series data by a network receive thread (Figure 5.2). This data is then written into a sufficiently large asynchronous software buffer. This circular buffer is necessary to avoid data loss ocurring due to variable network loads and relatively higher speed at which digital receiver generates the I-Q outputs. Another thread acts as a network server and initiates a separate thread to handle each of the multiple clients requesting connection to the Time Series Acquisition and Dissemination Server. These socket client threads read the output

of the buffer and stream it to remote servers such as the Time Series Archiver Server and the Moment Server.

5.1.2 Moment processing

The moment computation process is executed on high-end multi-core processors. The moment generation is a computationally expensive task and multiple cores allow decomposition of this process into several parallel threads. The network socket thread connects to the Time Series Acquisition and Dissemination Server to obtain the raw I-Q data and writes it to the circular buffer (Figure 5.3).

There are several programmable options which are used to configure the moment computation process. In its most general configuration, these options in the Moment Server are set through the configuration words sent by the system controller. In the absence of a system controller, a configuration file stored on the Moment Server is read directly by the moment program to prepare the raw I-Q data for product generation. The critical system options like calibration data (gain, transmit power and noise levels), finite bandwidth losses, number of integration samples, range gate contributions for each subpulse and clutter filter options are set at this stage. At the same time, information about the PRT pulsing scheme (uniform or staggered), polarization agility and diversity is ascertained through the flags set in the received time series as explained in Section 3.3.4. Following this conditioning, the time series data is buffered for number of integration samples. Separate threads are now initiated to compute moments for all range gates of each subpulse. The moment calculation algorithm may vary depending on whether clutter filtering is enabled or not. The existing moment processor employs the standard pulse-pair method to generate products by computing autocorrelations. This module has been designed to be seamlessly replaceable with the moment generation using the Time Domain GMAP (GMAP-TD) clutter filter (Nguyen and Chandrasekar, 2009) for non-uniform sampling in the future. For each

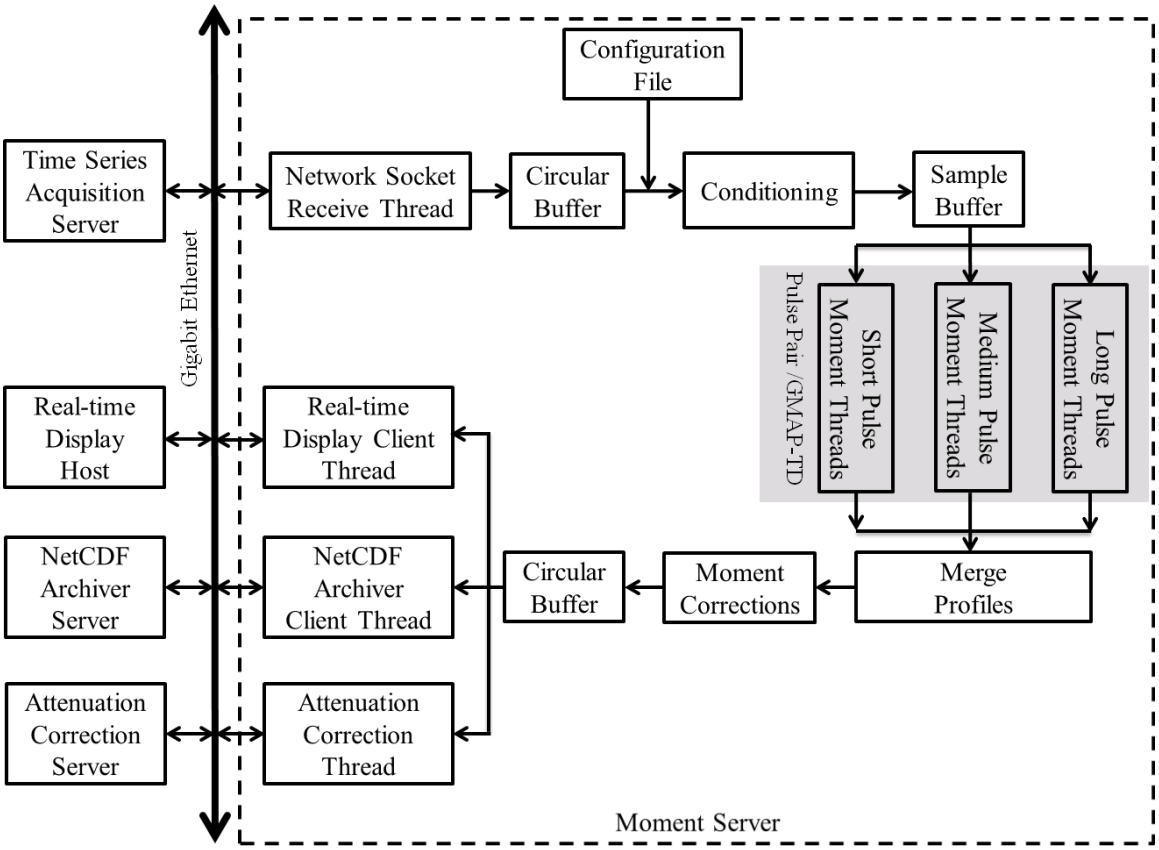

Figure 5.3: Conceptual diagram of moment computation process.

subpulse, the input data is computed in several constituent threads in groups of range gates.

The outputs from the subpulse threads are then merged in the main program to generate a single range profile for each product. The merge manager is also capable of applying the individual corrections or modifications (such as different receiver gains) on each of the subpulse profiles before merging them. This data is then queued in a buffer to service multiple networked clients such as product archiver, attenuation correction program and real-time display. When the connection to a new client is established, a separate thread to send data to that client is initiated. The outgoing data format is stamped with a single median antenna position and timestamp for the integrated product. A common packet format is used to service all the clients.

5.1.3 Time series archive and replay

The Time Series Archiver Server records the raw digital receiver output on the RAID (Redundant Array of Independent Disks). The core program on this server accepts the raw time series data from the Time Series Acquisition and Dissemination Server over the network (Figure 5.4). The disk writing process being slower than the variable network data rate, this data is first written into a large circular buffer. A separate thread reads this data from the buffer, extracts the timestamp (to append to the names of the created files) from the time series packet in Coordinated Universal Time (UTC) and writes the data on to the RAID. The time series packet also contains scan information which is used to determine the instance of a new file creation based on a file-per-sweep rule. The system controller can also flag the time series packet with the option to not archive any files. Following subsections describe the details of the different fields in the time series packet the order of which is listed in Table 5.1.

Header

This field indicates the beginning of a valid time series packet. It is a 32-bit integer with a fixed value (= 0xABCD1234).

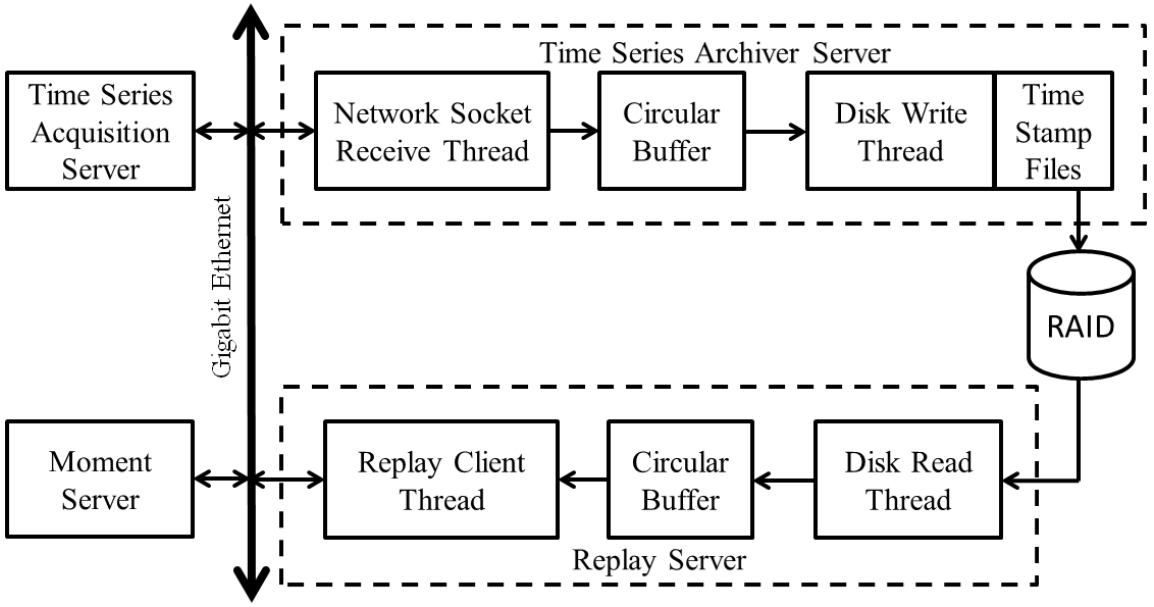

Figure 5.4: Conceptual diagram of time series archive and data replay process.

PRT Count

This field gives the 24-bit PRT counter value. An increment of 1 in the value indicate successive PRT packets.

Clock Ticks

This field gives the 24-bit Clock tick counter value. An increment of 1 in the value indicate successive 200MHz clock ticks. The value of the counter is sampled once every PRT.

FPGA1 Image Version: Year

This field gives the year of the version of the Signal Processing FPGA image. It is indicated by a BCD coded 16-bit number. For example, $0010|0000|0001|0000_2 = 2010_H$ corresponds to the year 2010.

FPGA1 Image Version: Date

This field gives the month and day of the version of the Signal Processing FPGA image. The month is indicated by a BCD coded 8-bit number followed by the date encoded in the same format. For example, $0001|0010|0011|0001_2 = 1231_H$ corresponds

to the thirty-first day of the twelfth month i.e. December 31.

FPGA1 Image Version: Number

This field gives the version of the Signal Processing FPGA image. It is indicated by an eight digit number followed by two 4-digit sub-version numbers. For example, 00001110|0011|1010 corresponds to Version 15.3.10.

FPGA2 Image Version: Year

This field gives the year of the version of the Interface FPGA image. It is indicated by a BCD coded 16-bit number. For example, $0010|0000|0001|0000_2 = 2010_H$ corresponds to the year 2010.

FPGA2 Image Version: Date

This field gives the month and day of the version of the Interface FPGA image. The month is indicated by a BCD coded 8-bit number followed by the date encoded in the same format. For example, $0001|0010|0011|0001_2 = 1231_H$ corresponds to the thirty-first day of the twelfth month i.e. December 31.

FPGA2 Image Version: Number

This field gives the version of the Interface FPGA image. It is indicated by an eight digit number followed by two 4-digit sub-version numbers. For example, 00001110|0011|1010 corresponds to Version 15.3.10.

DRX software Version: Year

This field gives the year of the version of the DRX software on the single-board DRX host computer. It is indicated by a BCD coded 16-bit number. For example, $0010|0000|0001|0000_2 = 2010_H$ corresponds to the year 2010.

DRX Software Version: Date

This field gives the month and day of the version of the DRX software on the single-board DRX host computer. The month is indicated by a BCD coded 8-bit number followed by the date encoded in the same format. For example, $0001|0010|0011|0001_2$

$= 1231_H$ corresponds to the thirty-first day of the twelfth month i.e. December 31.

DRX Software Version: Number

This field gives the version of the DRX software on the single-board DRX host computer. It is indicated by an eight digit number followed by two 4-digit sub-version numbers. For example, 00001110|0011|1010 corresponds to Version 15.3.10.

GPS Timestamp

This field gives the information about the year, month, day, hour, minute and second stamp of the current ray. Each field is 32-bit and formatted to give the Unix Time.

Latitude, Longitude, Altitude

This field gives the information about the latitude, longitude and altitude of the installed radar. These parameters are obtained by scaling this signed value by 1e-6.

Antenna Position: Azimuth

This field gives the azimuth information collected from the antenna position decoder. The azimuth angle is obtained by scaling this signed value by 1e-6.

Antenna Position: Elevation

This field gives the elevation information collected from the antenna position decoder. The elevation angle is obtained by scaling this signed value by 1e-6.

Archiving Enable

A value of '1' in this field indicates that the time series data should be archived. A value of '0' indicates the opposite.

Online Digital Health

A value of '1' in this field indicates that the digital receiver chain has been found to be working as per the expectations and the ensuing time series data is valid. A value of '0' indicates that following time series data should be ignored for all the calculations.

Transmit Mode

This field indicates the status of H and V transmitters and its value should be interpreted as follows:

00 = None of the H and V transmitters were fired.

01 = Only H transmitter was fired.

10 = Only V transmitter was fired.

11 = Both H and V transmitter were fired.

PRF Selection

A value of '0' indicates PRF 1 and a value of '1' indicates PRF 2 for the corresponding data packet. This field facilitates inferring uniform or staggered PRT mode.

Calibration Enable

A value of '1' in this field indicates that the DRX data corresponds to the calibration channel of transceiver. A value of '0' indicates regular receiver channel data.

ADC/BIST

This field indicates if the source signal for the DRX is ADC or BIST. A value of '0' indicates ADC and a value of '1' indicates BIST.

DPC Bypass

This field indicates if the time series data has been collected after the digital pulse compression or before. A value of '0' indicates DPC was not bypassed and a value of '1' indicates it was bypassed.

Scan Type

This field indicates the nature of data collection and type of antenna scan. This is a three-bit value to be interpreted as follows:

000 = Vertically pointing antenna (VPT): Data with the antenna pointing vertically.

001 = Fixed positing antenna (FPT): Data with the antenna fixed at a specified azimuth and elevation.

010 = Plan position indicator (PPI): Data volume with PPI sweeps. The file can

have one or many PPI sweeps. The sector size of the individual PPI sweeps need not be the same.

011 = Range height indicator (RHI): Data volume with RHI sweeps. The file can have one or many RHI. The sector size of the individual RHI may not be the same.

100 = Co-plane scanning (COP): Data volume with COP sweeps. The file can have one or many COP. The sector size of the individual COP may not be the same.

101 = Heterogeneous sweeps (HGS): Data volume with heterogeneous sweeps in the file. The data file can have any number and combination of radar sweep types (i.e., FPT, PPI, RHI, COP).

110 = Reserved

111 = Reserved

Scan On/Off

This field indicates if the radar scan is in progress. A value of '1' indicates that the scan is in progress and the value of '0' will indicate otherwise.

00 = Scanning Scan Off

01 = Scanning Scan On

10 = Slewing Scan Off

11 = Invalid Value

PRT Sequence Number

This field indicates if the current PRT is part of phase-code sequence. Its value toggles between '0' and '1'. Its consecutive packet values are a string of zeros or ones. The transition between the two values indicate the begining of a new sequence.

Scan Count

This field indicates the number of remaining scans (including the ongoing scan) in the current scan task. The minimum acceptable value of this field is 1.

Number of range cells

This field gives the number of gates in the ensuing time series data of each subpulse

channel.

Time series data

This field gives the fixed-point format I and Q samples for every range gate corresponding to the subpulses f_1, f_2 and f_3 of both H- and V- channels in that order.

The time series data can be read back from the RAID for a replay of the scan (Figure 5.4). The replay server sends the time series data to the Moment Server where the data is processed as if it has been received from the digital receiver. This mode is useful in regenerating products while testing a new or modified moment processing technique and examining the time series for further analysis on a display program.

5.1.4 Interfaces to netCDF archiver and display

The netCDF (network Common Data Form) data format (Rew et al., June 2011) is chosen to store the single and dual frequency data sets. The netCDF format is machine-independent/portable, self-describing array-oriented scientific data format that is supported by the freely available netCDF library. A netCDF file contains dimensions, variables, and attributes. These elements combined together capture the data set and all the associated information about the data fields in an array-oriented data set. The dimension is used to represent the axes of the variables stored in the file. The dimension may be used to represent an actual physical dimension, e.g. time, height, and range. The dimension may also be used for indexing the variables to structure the data set according to instrument operation or convenience of representation, for example, sweep index and volume index. The data in netCDF files can also be stored in packed format which allows for using smaller data types to store the original data by limiting the numerical precision of the data values. The attributes of the packed data - scale factor and offset - can be used to unpack the data values. The netCDF archiver server receives the data from Moment Server and creates netCDF files in a process similar to that of the Time Series Archiver Server as described in Section 5.1.3.

Table 5.1: Sequence of the data fields in the time series packet

Message	Bits/Frequency	Source
Header	32/packet	Digital Receiver
PRT Count	24/packet	Digital Receiver
Clock Ticks	24/packet	Digital Receiver
FPGA1 Image Version: Year, Date, Number	48/packet	Digital Receiver
FPGA2 Image Version: Year, Date, Number	48/packet	Digital Receiver
DRX Software Version: Year, Date, Number	48/packet	Digital Receiver
GPS Timestamp: Year, Month, Day	96/packet	GPS Decoder
GPS Timestamp: Hour, Minute, Seconds	96/packet	GPS Decoder
Latitude, Longitude, Altitude	96/packet	GPS Decoder
Antenna Position: Azimuth	32/packet	Antenna Position Decoder
Antenna Position: Elevation	32/packet	Antenna Position Decoder
Archiving Enable	1/packet	Antenna Position Decoder
Online Digital Health	1/packet	Digital Receiver
Transmit Mode	2/packet	Waveform Generator
PRF Selection	1/packet	Waveform Generator
Calibration On	1/packet	System Controller
ADC/BIST	1/packet	System Controller
DPC Bypass	1/packet	System Controller
Scan Type	3/packet	Antenna Position Decoder
Scan On/Off	2/packet	Antenna Position Decoder
PRT Sequence Number	1/packet	Waveform Generator
Scan Count	16/packet	Antenna Position Decoder
Number of range cells (N)	16/packet	System Controller
$I^{(1)}_{H-f_1} \cdots I^{(N)}_{H-f_1}$	24/range cell	Digital Receiver
$Q^{(1)}_{H-f_1} \cdots Q^{(N)}_{H-f_1}$	24/range cell	Digital Receiver
$I^{(1)}_{V-f_1} \cdots I^{(N)}_{V-f_1}$	24/range cell	Digital Receiver
$Q^{(1)}_{V-f_1} \cdots Q^{(N)}_{V-f_1}$	24/range cell	Digital Receiver
$I^{(1)}_{H-f_2} \cdots I^{(N)}_{H-f_2}$	24/range cell	Digital Receiver
$Q^{(1)}_{H-f_2} \cdots Q^{(N)}_{H-f_2}$	24/range cell	Digital Receiver
$I^{(1)}_{V-f_2} \cdots I^{(N)}_{V-f_2}$	24/range cell	Digital Receiver
$Q^{(1)}_{V-f_2} \cdots Q^{(N)}_{V-f_2}$	24/range cell	Digital Receiver
$I^{(1)}_{H-f_3} \cdots I^{(N)}_{H-f_3}$	24/range cell	Digital Receiver
$Q^{(1)}_{H-f_3} \cdots Q^{(N)}_{H-f_3}$	24/range cell	Digital Receiver
$I^{(1)}_{V-f_3} \cdots I^{(N)}_{V-f_3}$	24/range cell	Digital Receiver
$Q^{(1)}_{V-f_3} \cdots Q^{(N)}_{V-f_3}$	24/range cell	Digital Receiver

The radar display employed here is the CHILL Real-time Display (RTD) (GTK Display, 2012) which is a Unix-based radar display software. When the RTD is launched on a remote host, it requests connection to the real-time display node at the Moment Server. The Moment Server RTD node makes the products available to the RTD on demand. The RTD can also provide visualization in either the PPI or A-Scope mode, superimpose maps and GIS information, infer the location data from the GPS information in the moment packets and apply simple numerical thresholds while displaying the data.

5.2 Processing algorithms

As described in Section 1.2.1, the time series output of digital receiver is an array of complex numbers ($I_k + jQ_k$ where $k = 1, \cdots, N$). This array is used for statistical computations yielding variables which provide useful information about the hydrometeor scatterers. This section first explains the physical meaning of the available products followed by the special processing techniques for the three-pulse waveforms.

5.2.1 Available products

The standard moments and the dual-pol variables are always computed and archived by the signal processor. The calculation of the standard and dual-polarized moments from the Sinclair matrix was explained in Section 1.2.4. Following describes the relation of these moments with the time series data and their meteorological interpretation.

Equivalent reflectivity factor

The equivalent reflectivity factor for horizontal polarization, Z_h, at a particular range cell is obtained by computing the mean received power $\bar{P}_h$ at that range cell:

$$\bar{P}_h = \frac{\sum^{N} \left(I_h^2 + Q_h^2\right)}{N} \tag{5.1}$$

where N is the number of integration samples. As explained in Section 1.2.2, the Z_h is then calculated as

$$Z_h \ (dBZ) = 10 \log_{10} \bar{P}_h + C - G_{rx} + 20 \log_{10} R \tag{5.2}$$

where C is the radar constant in log scale, G_{rx} is the gain of the radar receiver and R is the range (in km). This equation is a logarithmic version of the weather radar equation for distributed targets. The radar reflectivity factor for the vertical polarization can be similarly computed using $\bar{P}_v$. The quantities Z_h and Z_v are directly related to the first-order autocorrelation moment of the time series. A related product is the Normalized Coherent Power (NCP) or Signal Quality Index (SQI) which is the ratio of lag 1 autocorrelation to lag 0 autocorrelation:

$$NCP = \frac{|R_1|}{R_0} \tag{5.3}$$

This product is normalized magnitude of autocorrelation at lag 1 and varies from unity for a noise-free zero-width signal to zero for an uncorrelated signal.

Mean Doppler velocity

For a symmetric Doppler spectrum , the estimate of mean velcoity can be calculated from the autocorrelation at lag 1,

$$\hat{\bar{v}} = -\frac{\lambda}{4\pi T_s} \angle(\hat{R}[1]) \tag{5.4}$$

where λ is the radar wavelength, T_s is the pulse repetition or sampling time and $\hat{R}[1]$ is the autocorrelation at lag 1. This calculation is valid for the uniform pulsing scheme where the unambiguous velocity is given by,

$$v_u = \frac{\lambda}{4T_s} \tag{5.5}$$

The calculation of the estimate of mean velocity for the staggered PRT scheme is explained in Section 5.2.3.

Spectrum width

The Doppler spectrum of weather echoes has a Gaussian shape. The variance of this distribution or the spectrum width is the measure of shear and turbulence. Also, a faster antenna rotation rate has the effect of broadening the wetaher echo spectrum. For the uniform pulsing scheme, the estimate of the spectrum width is calculated using lag 0 and lag 1 autocorelations:

$$\hat{\sigma}_v = \frac{\lambda}{2\pi T_s \sqrt{2}} \left[\ln \left| \frac{R(0)}{R(1)} \right| \right]^{1/2} \tag{5.6}$$

In the presence of noise $R(0)$ is replaced by $R_{S+N}(0) - R_N(0)$ where the indices S and N represent the presence of the signal and noise respectively. For the staggered pulsing scheme, the spectrum width computation is discussed in Section 5.2.3.

Differential reflectivity

The differential reflectivity Z_{dr} (dB) is the ratio of Z_h to Z_v. Z_{dr} is negative for prolate, positive for oblate and zero for spherical scatterers. Raindrops tend to flatten and are usually oriented oblately. It can also be zero for nonspherical particles which have a random distribution of orientations such as hail. Z_{dr} can therefore be used to discriminate hydrometeor types. The observations of differential reflectivity are also related to drop size distribution (DSD) parameters like the mean mass diameter (D_m) and the median volume diameter (D_0) (Gorgucci et al., 2002).

Differential propagation phase

The differential phase shift (Φ_{dp}) discussed in Setion 1.2.4 is a measure of the propagation phase difference between the horizontally and vertically polarized waves. For oblate raindrops, the propagation of the horizontally polarized waves is slower than the vertically polarized waves. As a result, the phase shift of the horizontal component is larger. The phase shift is an important parameter for hydrometeor classification and rainfall estimation. The range derivative of Φ_{dp} is known as the specific differential

propagation phase K_{dp}, i.e.,

$$K_{dp}\ (^{\circ}/_{km}) = \frac{1}{2}\frac{d}{dr}\Phi_{dp} \tag{5.7}$$

$$= \frac{\Phi_{dp}(r_2) - \Phi_{dp}(r_1)}{2(r_2 - r_1)} \tag{5.8}$$

The K_{dp} is closer to DSD for rainfall estimation and is less susceptible to DSD variablility compared to the Z-R relations. K_{dp} is relatively less sensitive to ice in the radar volume.

Copolar correlation coefficient

Copolar correlation coefficient ρ_{co} is sensitive to the distribution of particle sizes, axis ratios and shapes. For raindrops and ice crystals, theoretically ρ_{co} can be estimated to be 0.99 while it is less than 0.90 within the melting layer. The copolar correlation coefficient can also be used for hard target calibration (for which it is close to unity) and solar calibration. During a 'quiet' sun day, i.e., when there are no flares or sun spots, the solar radiation is randomly polarized. The correlation coefficient calculated for the center of a quiet sun is, therefore, very low (<0.1).

Linear depolarization ratio (LDR)

Like ρ_{co}, LDR is also sensitive to the presence of large wet particles and hence, useful for hydrometeor identification. The particles, whose major axes are not aligned with the transmit polarization, scatter some signal in the orthogonal polarization state as well. The cross-polar signals often originate from the wobbling nonspheroidal particles and are enhanced for wetted and melting particles. Usually, LDR has smaller values (-35 to -15 dB) but, within the melting layer, it can increase to -15 to -20 dB.

5.2.2 I-Q processing in GSL

Using the I and Q samples, the moment processor forms vectors and matrices to calculate the autocorrelations and covariances before generating the products described in Section 5.2.1. This process is computationally expensive and, therefore, a

numerical software package GNU Scientific Library (or GSL) (Galassi et al., April 29 2011) is used to achieve greater efficiency. The GSL is a software library for numerical routines which includes complex number datatypes, matrix eigenvalues and eigenvectors, singular-value decompositions, linear equations, least-squares, numerical differentiation and statistics. The GSL is part of the GNU Project and is distributed under the GNU General Public License. It is portable to both GCC (GNU C Compiler) and Intel compilers.

The I-Q processing requires complex number arrays and statistical routines from GSL. GSL uses it own memory management for matrices and vectors. The GSL matrices are defined as C-structs that also contain information about the size of the matrix. Unlike other standard numerical linear algebra packages such as BLAS (Basic Linear Algebra Subprograms) and LAPACK (Linear Algebra PACKage) which are originally FORTRAN libraries, GSL is written entirely in standard C and makes heavy use of header files, C typedefs, and other C data types and data structures that have no counterparts in Fortran. This absence of C wrapper programs in GSL makes it easier to code and compile within I-Q processing routines on moment processors. Also, the GSL supports double precision complex numbers and is, therefore, suitable to process the 24-bit I-Q outputs from the digital receiver.

5.2.3 Staggered PRT mode

When the moment processor detects the staggered PRT flag in the time series packet, it employs different algorithms for the calculation of mean Doppler velocity and spectrum width. Section 2.1 explains the calculation of the velocity in staggered PRT mode. The mean unambiguous velocities v_1 and v_2 corresponding to each PRT are first estimated as.

$$\hat{\bar{v}}_1 = -\frac{\lambda}{4\pi T s_1}\angle(\hat{R}_{T1}[1]) \tag{5.9}$$

$$\hat{\bar{v}}_2 = -\frac{\lambda}{4\pi T s_2}\angle(\hat{R}_{T2}[1]) \tag{5.10}$$

where Ts_1 and Ts_2 are the corresponding PRTs. The autocorrelations at lag 1 for the echoes corresponding to these PRTs are $\hat{R}_{T1}[1]$ and $\hat{R}_{T2}[1]$. The dealiasing of the velocity for the staggered 2/3 PRT waveform is then carried out using the Chinese remainder theorem.

As for the spectrum width, autocorrelation moments up to the second lag can be used depending on their accuracy and speed. The simplest spectrum width estimator employs the magnitude of the autocorrelation of first lag of the smaller PRT echoes. It assumes that the Doppler spectrum is Gaussian and that the signal-to-noise ratio is large.

$$\hat{\sigma}_v = \frac{\lambda}{2\pi T_s\sqrt{2}}\left[\ln\left|\frac{R(0)}{R_{T1}(1)}\right|\right]^{1/2} \tag{5.11}$$

For the weaker signals where the signal-to-noise is lower, the spectrum width is estimated using the second lag autocorrelation moment:

$$\hat{\sigma}_v = \frac{\lambda}{2\pi T_s\sqrt{2}}\left[\ln\left|\frac{R_{T1}(0)}{R_{T2}(1)}\right|\right]^{1/2} \tag{5.12}$$

5.2.4 LDR processing mode

As described in Section 1.2.4, the LDR is defined as the ratio of cross-polar signal return to the coploar signal return,

$$LDR\ \ (dB) = 10\log_{10}\left(\frac{Z_{cx}}{Z_{co}}\right) \tag{5.13}$$

where Z_{cx} and Z_{co} are reflectivities obtained from the return signal power in the cross-polar and co-polar channels respectively. For example, if the transmit polarization state is horizontal (vertical), the reflectivity in the horizontal channel is given by Z_{hh} (Z_{hv}) and in the vertical channel by Z_{vh} (Z_{vv}). The LDR in the horizontal (vertical) transmit mode is then given by LDR_{vh} (LDR_{hv}):

$$LDR_{vh}\ \ (dB) = 10\log_{10}\left(\frac{Z_{vh}}{Z_{hh}}\right) \tag{5.14}$$

$$LDR_{hv}\ \ (dB) = 10\log_{10}\left(\frac{Z_{hv}}{Z_{vv}}\right) \tag{5.15}$$

LDR is sensitive to the canting angle of hydrometeors but it can be difficult to detect it dur to the cross-polar performance of the antenna as explained in Chapter 6. In the

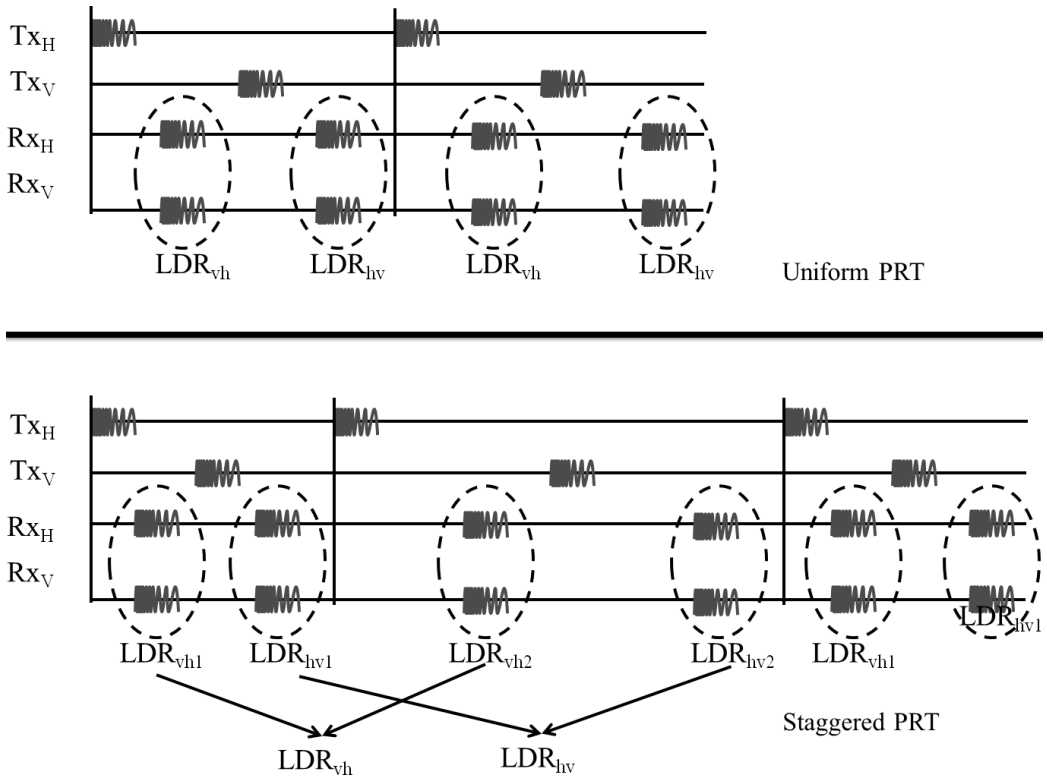

Figure 5.5: Computation of LDR in staggered PRT mode. Contrary to the inform pulsing, the number of range gates for the LDR corresponding to each polarization state varies for every alternate transmit cycle of that polarization in the staggered PRT pulsing. The LDRs are computed only for the minimum of the number of the range gates of the two transmit cycles.

uniform pulsing mode, the LDR for each transmit state is calculated in every alternate transmit cycle (Figure 5.5). The total number of range gates for the LDR of each transmit state remains same for each transmit cycle. However, for the staggered PRT pulsing, the number of gates vary for every alternate cycle of the same transmit state. The moment processor then only calculates LDR of each transmit state only for the number of gates corresponding to the smaller PRT. If the actual number of range gates corresponding to the LDR_{vh1} (LDR_{hv1}) is N_1 and to the LDR_{vh2} (LDR_{hv2}) is N_2, then the number of range gates in the output product of LDRs of both the PRTs

is,

$$N = min(N_1, N_2) \tag{5.16}$$

5.2.5 Calibration mode and variable pulse averaging

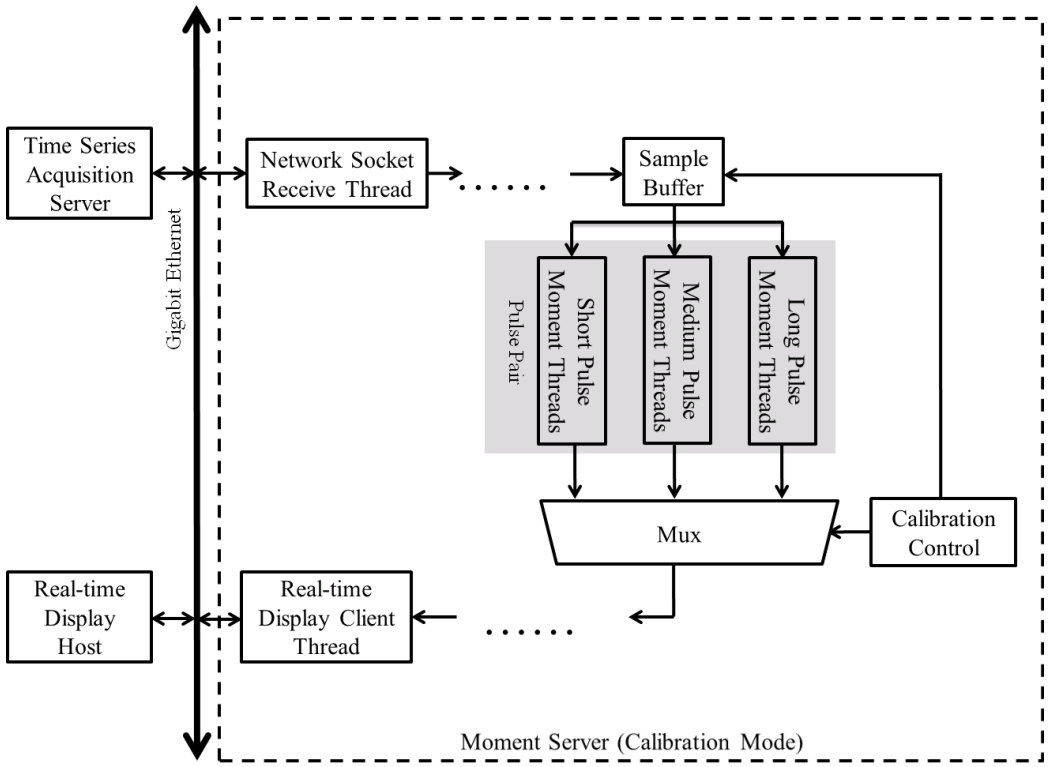

Figure 5.6: Moment processor in calibration mode allows power products to be available for full range profiles of each subpulse.

Weather radar calibration is essential in the error-free operation of the system and improvement of the data quality. Modern digital receivers have made the process of the online calibration simpler. The power and frequency sweeps to calibrate the receiver gain should often be performed to keep the system updated. In the calibration mode, the digital receiver is still in the standard mode and outputs the I-Q data to the moment processor. However, the moment processor no longer merges the profiles from each of the subpulses (Figure 5.6).

The calibration control word can configure the moment processor to output the full range profiles of either of the subpulses. Also, the autocorrelation at zero lag is

available for both the horizontal and vertical channels. This can be used to estimate the receiver gains for both polarizations. Further, the number of integration samples can also be changed in the Sample Buffer. The number of samples in the standard mode is 128 but the calibration mode allows it to vary in powers of 2 from 8 to 1024. The sample size smaller than 8 causes dataloss while sample size larger than 1024 slows down the real-time operation.

5.2.6 Sensitivity Enhancement System (SES) processing mode

Chandrasekar et al. (October 2010) have developed a sensitivity enhancement system (SES) for pulse compression weather radar systems. The underlying principle of SES is that the first waveform is used to estimate prior knowledge about the signal while the second waveform, designed with the larger native range resolution and less receiver noise, will utilize that information to perform SES processing. This waveform has been tested on field for the D3R system. The SES processing mode for this radar as implemented in the digital receiver and signal processor is described as follows.

In its normal operational mode, the moment processor employs a novel frequency-diversity waveform (Mishra et al., 2012) consisting of three subpulses of duration 40 μs (long), 20 μs (medium) and 1 μs (short). The long and medium pulses are coded with the signal bandwidth of 3.6 MHz each. For the transmission, this waveform is upconverted from a baseband sample rate of 50MHz. The digital receiver sub-samples the received waveform at 200 MHz and then processes the downconverted data through a pulse compression filter which has an output sample rate of 10 MHz (Mishra et al., 2011). The In-phase (I) and Quadrature-phase (Q) outputs are finally made available at a downsampled rate of 1 MHz.

For the SES experiment on the D3R system (Nguyen et al., 2011), the waveform consisted of only the long and medium subpulses (Figure 5.7). The pulse durations for the two-pulse SES waveform were kept identical to that of the long and medium pulses of the normal three-pulse D3R waveform. Further, the measurements obtained

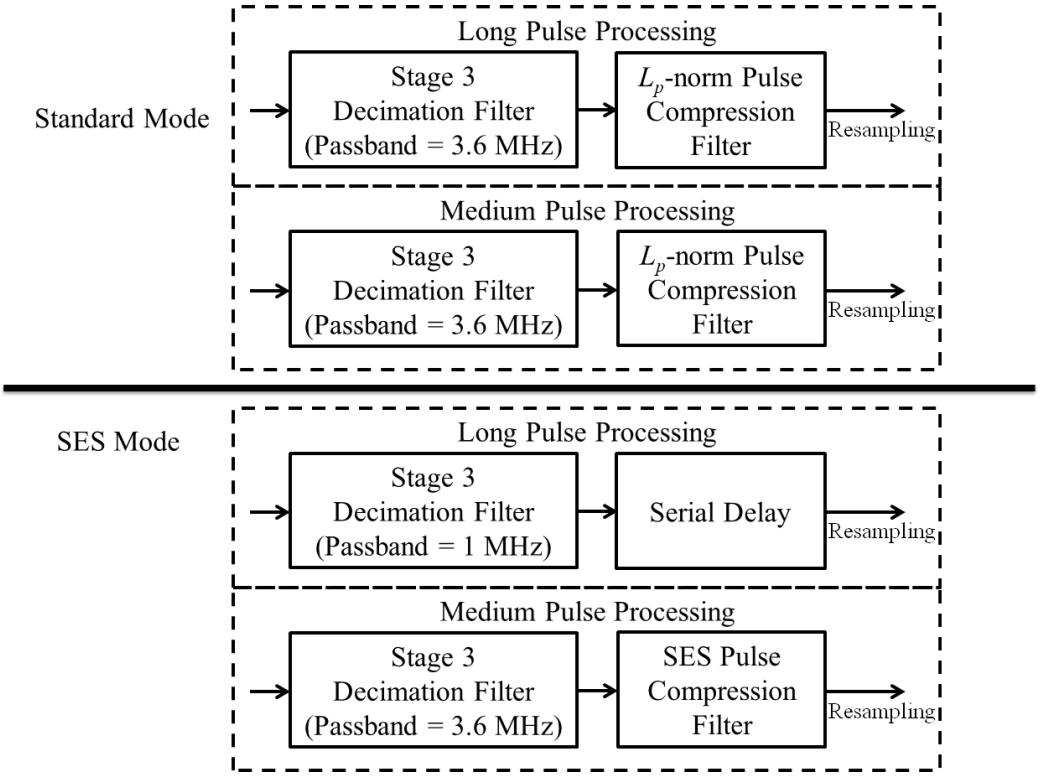

Figure 5.7: SES Processing Mode of the digital receiver. The pulse compression filter for the long pulse processing channel is programmed to operate as a serial delay block.

by the medium pulse in the SES waveform were used as a reference. Therefore, the signal bandwidth (= 3.6 MHz) of the SES medium pulse was also identical to that of the medium pulse in the regular three-pulse waveform. However, the SES long pulse was designed for 1 MHz bandwidth which is different than that of the regular long pulse. This is because even though the medium pulse is processed in the 10 MHz compression filter, this data is only available at a downsampled rate of 1 MHz in the current radar configuration. This setup allows compatibility with the normal processing mode of the radar.

For the SES processing mode, the pulse compression filter of the long pulse channel is configured to act as a serial delay block for the same number of taps as in the original pulse compression filter. In this configuration, the range calibration within the digital receiver doesn't need any alteration as also the subsequent processing in the moment processor.

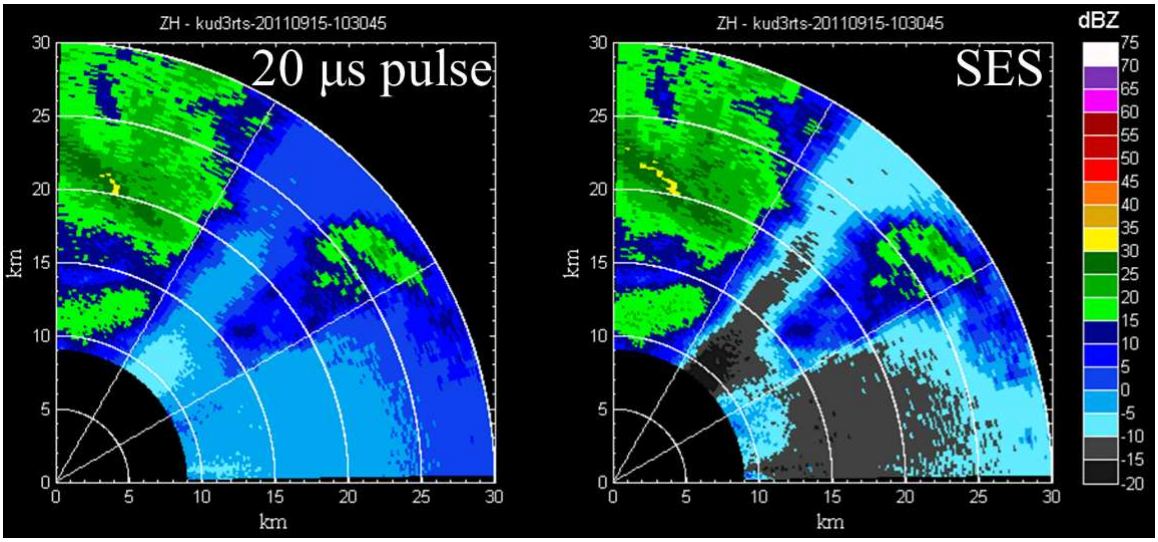

Figure 5.8: Sector PPI images of reflectivity (H-polarization) during a light rain event observed by the D3R system. Left panel: 3.6 MHz bandwidth medium pulse output processed with an ISL filter. Right panel: Outputs of the SES processing (Nguyen et al., 2011).

The SES experiment on the D3R system was carried out on September 15, 2011 during a light rain event. The D3R radar was deployed at the CSU-CHILL radar

facility at Greeley, Colorado at the time of the experiment. Figure 5.8 shows the Ku-band measurements from the reference medium waveform in SES mode and the product so obtained using SES processing for the long pulse during a sector PPI scan. In Figure 5.8 the observations made by the SES and medium pulses show a remarkable agreement in the reflectivity for the stronger echo regions. In the weak echo regions such as the 30-90° sector, it is obvious that the SES processing provides better sensitivity.

5.3 Summary

This section presented the processing algorithms for the frequency-diversity waveforms and the transmit pulsing modes associated with them. The critical future upgrades to the signal processor should include clutter filtering for the non-uniform pulsing and real-time attenuation correction. The spectrum width algorithms for the staggered PRT should also be improved further. The real-time moment processing for the SES mode is also possible in the GSL processing. Many of the existing modes described in this chapter have been tested on field for the NASA D3R system. The next chapter describes the special waveform design and considerations fo this radar in the context of its broad scientific and engineering goals. The example data for the digital receiver and the signal processor modes are presented in the subsequent chapter.

CHAPTER 6

THE NASA DUAL-FREQUENCY DUAL-POLARIZED DOPPLER RADAR

Since the arrival of remote sensing of clouds and precipitation on space-borne platforms, much progress has been made in related radar instrumentation, algorithm improvement and interpretation of the data. Lately, the dual-polarization measurements for satellite sensing has opened up interesting research opportunities in the ground validation of satellite missions (Chandrasekar et al., 2008). The objectives of a ground validation program include quantitative assessment of the the error in space-borne estimates, invetigation of sources of those errors, advance evaluation of methods to mitigate them and improvement of existing retrieval algorithms.

The digital receiver and signal processor design discussed in Chapters 3-5 was first deployed and tested on the NASA D3R which is integral to the GPM Ground Validation program. This chapter describes the NASA D3R system and challenges associated with the retrievals in this radar.

6.1 Overview of the D3R system

The scientific understanding of the global water cycle requires detailed knowledge of vertical precipitation structure and the mesoscale physical structure of rain systems on a global scale and those can only be directly obtained by a spaceborne radar. The successful introduction of a single-frequency (Ku-Band: 13.8 GHz) Precipitation Radar (PR) onboard the Tropical Rainfall Measuring Mission (TRMM) satellite in

1997 facilitated improved understanding of the spatial distribution, variability, intensity of rainfall and its role in climate in tropical and subtropical regions (Kummerow et al., 2000). As a follow-on mission to TRMM, the Global Precipitation Measurement (GPM) mission will attempt to advance further the goal of making global scale precipitation observations to higher latitudes with more frequent sampling by deploying the next generation of satellite-borne weather radars.

The GPM core satellite will carry a Ku-Ka band Dual-frequency Precipitation Radar (DPR) (Iguchi et al., 2003) that can make multi-parameter measurements of precipitation directly related to the microphysical rain structure (such as raindrop size distribution and vertical water content profiles). While the Ku-band radar is an advanced, high-resolution version of the TRMM precipitation radar, the Ka-band radar will provide higher sensitivity which can prove useful in the measurement of snow and light rain. To ensure desired accuracy and validation of DPR measurements as well as enhance robustness of the retrieval algorithms, GPM will employ a comprehensive and global ground validation (GV) program (Bidwell et al., 2004). The Dual-Frequency Dual-Polarized Doppler Radar (D3R) is a ground validation radar for the GPM-GV program which has been jointly developed by Colorado State University, NASA Goddard Space Flight Center and Remote Sensing Solutions. The leg work on the radar began in Fall 2008 and a mechanically working system was deployed at Southern Great Plains (SGP) site of the Department of Energy (DoE) Atmospheric Radiation Measurement (ARM) program during the GPM Midlatitude Continental Convective Clouds Experiment (MC3E) during the summer of 2011. A fully functional radar system then successfully participated in the GPM Cold Season Precipitation Experiment (GCPEx) at the Environment Canada (EC) Center for Atmospheric Research Experiments (CARE) site in Egbert, Ontario, Canada during early spring of 2012.

The preferred frequency bands of operation for precipitation surveillance in ground radar systems have been nearly non-attenuating frequencies such as S- and C-band

or attenuating frequencies like X band which are employed for short-range measurements. But it is not practical to use traditional ground-based weather radar frequencies (such as S- or C-band) for space-borne precipitation radars because of the limitations imposed by the size of the satellite-mounted antenna and the power available. On the other hand, moving to the higher frequencies to observe precipitation offers the challenge of attenuation in signal propagation due to precipitation. The Ku-band frequency in TRMM PR was successfully demonstrated to be very useful for tropical rain profiling (Iguchi et al., 2010). However, TRMMs center-frequency (13.8 GHz) is less sensitive to backscatter from smaller raindrops. Therefore, the GPM mission has embarked on a dual-frequency approach at Ku- and Ka-band for characterizing the precipitation. Ka-band, in particular, would considerably increase the radars sensitivity towards light rain, drizzle and snow and also offer excellent spatial resolution. In addition, the dual-frequency system also provides a mechanism for retrieving the raindrop size distribution.

6.1.1 Scientific objectives

The GPM-GV D3R is a dual-frequency ground-based radar which provides for various options, including polarimetry and Doppler capabilities. Polarimetry is critical for understanding the microphysics and, in the recent times, extensive use of polarimetric radar systems at higher frequencies has been made feasible by advances in attenuation correction methods based on polarimetric measurements. Doppler measurements are useful for linking the dynamics with the microphysics of precipitation structure. Thus, as a value-added validation instrument, it is very useful to have both dual-polarization and Doppler measurement. Hence, the name D3R or Dual-frequency Dual-polarized Doppler Radar. The scientific goals of D3R extend over several seminal research areas, some of which include the following:

Enrich dual-frequency database

While extensive ground radar observations of precipitation are available at S- and

C- band, such measurements do not exist at Ku- and Ka-band. Ground radar measurements enjoy the advantage of coincident microphysical observations available to interpret radar signatures. An important broader science goal of the NASA D3R is to enhance the database of dual-frequency radar observations on the ground, in conjunction with existing observations, in order to provide a dataset for physical validation (Chandrasekar et al., 2012). The sensitivity of the system at both frequencies is pegged at -10 dBZ at 15 km to enable snow measurements, which can document the "missing tail" in the current snow observations from GPM DPR.

Microphysical Characterization

Dual polarization radar observations can be used operationally to not only improve the data quality of a standard Doppler radar but also improve precipitation measurement accuracy and provide a basis for hydrometeor classification. D3R is aimed to yield enhanced microphysical characterization similar to what has been done at lower frequencies. The measurement of precipitation at higher frequencies is particularly useful in understanding behavior of falling snow and ice.

Error Characterization

The routine reporting of error estimates from ground validation site is one of the major operational activities. The self-consistency of dual-polarization and dual-frequency observations presents an additional level of interpretation. The error estimates are usually based on a composite retrieval derived from a mean of time and space-coincident products from satellite-borne instruments and the validation sites. The multiple overpasses of the satellites serve as multiple sources of composite products with the validation site observations as a substitute of ground truth. With the ground-based D3R, an independent estimation of hydrometeor classification and drop size distribution retrievals can be carried out to understand the error structure of retrievals. Thus, the radar will also offer an insight into the physics of the retrieval processes and the associated measurement errors.

Algorithm Improvement

The current spaceborne retrieval algorithms are susceptible to various sources of errors which include assumptions regarding DSD parameters, vertical extent of liquid water and ice content, attenuation due to clouds and horizontal variations of precipitation in a remote resolution cell. The D3R will help the development for the ground validation counterparts of satellite-borne retrieval algorithms. The ground validation algorithms would help in the understanding and quantification of errors associated with the model assumptions in the satellite-borne algorithms. In this respect, D3R can provide anchor points for the global retrieval algorithms used in GPM DPR. While the DPR will present a global picture of precipitation through observations at Ku- and Ka-band, the ground-based D3R will yield detailed fine-scale local statistics of the microphysical interpretation.

6.1.2 Technical specifications

D3R has been designed as developed as a fully polarimetric, ground-based, scanning weather radar system. The nominal operating frequencies of D3R are 13.9 GHz and 35.5 GHz to allow for close compatibility with GPM instrumentation like High-Altitude Imaging Wind and Rain Airborne Profiler (HIWRAP) (Heymsfield et al., 2006) and DPR (Schwaller, Oct 21, 2009).

The sensitivity of D3R should be better than that provided by the space-based DPR so that it permits testing of validation of the DPR algorithms. The sensitivity of the radar is pegged at -10 dBZ at 15 km in clear air for a single pulse at 150 m range resolution for both the frequencies. This is achieved through careful designs at multiple levels. First, the antennas for both the frequencies have high gains of the order of 45 dB. Second, the transmitted waveform is based on the frequency diversity pulse compression technique which has been implemented on digital waveform generator and receiver for the solid-state transmitter system. The transmitters themselves have relatively higher power of 200 W and 45 W at Ku- and Ka-band respectively. At

the time of writing this thesis, the radar was using a placeholder Ka-band transmitter of 1 W output. The dynamic range of the receiver is expected to be greater than 90 dB for reasons described in Chapter 2.

The gain of the antenna is critical in determining its size at a particular frequency. If ϵ_A is the aperture efficiency and A is the cross-sectional area of the parabolic dish, then the diameter of the antenna D is related to the gain and frequency as (Kraus and Marhefka, 2002),

$$G_{lin} = \frac{4\pi A}{\lambda^2}\epsilon_A \tag{6.1}$$

$$\text{or, } D = \frac{\sqrt{G}\lambda}{\pi\sqrt{\epsilon_A}} \tag{6.2}$$

where G_{lin} is the antenna gain on the linear scale. The parabolic dishes of D3R antennas for Ku- and Ka-bands have the diameters 6 ft (1.8288 m) and 28 inches (0.7112 m) respectively. This gives an aperture efficiency of $\sim$0.4.

The size of the antenna also determines the minimum operating range of the radar since the measurements in the near-field range are unreliable. The near-to-far-field transition of an antenna is given by,

$$d_f = \frac{2D^2}{\lambda} \tag{6.3}$$

This gives the near-to-far-field transition ranges of Ku- and Ka-band antennas as 310 m and 120 m respectively. Further, the recovery time of the RF receiver is estimated to be about 2 μs equivalent to the range of 300 m for both the frequencies. Moreover, the blind range of the shortest pulse in the frequency-diversity waveform is 150m. Considering all three factors, the D3R has the minimum operational range specified as 450 m.

The radar has both polarization diversity and polarization agility to allow measurement of products like LDR for hydrometeor classification. The cross-polar isolation of more than 32 dB is provided on the antennas for both frequencies for acceptable

cross-polarized backscatter detection capability. The nominal half power beam width (HPBW) of the radar is less than a degree in any principal plane. This permits an approximate vertical resolution of 500 m at a range of 30 km - a nominal limit for research purposes. To minimize bias errors in the measurement of Z_dr, both of the radar antennas H- and V-beams matched within 5% and the receiver cross-pol isolation greater than 35 dB. Further, antenna beam sidelobe gains are 25 dB lower than the main beam to prevent contamination from the ground clutter and other targets outside the purview of the HPBW. The antenna performance is further evaluated in Section 6.2.

The antenna and pedestal system is capable of scanning at variable scanning rates ranging from a minimum of 1°/s to 24°/s to also record rapidly changing meteorological events with sufficient variability. The radar can also perform over-the-head RHI scans and the elevation scan range is full 0-90°.

The unambiguous Doppler velocity for D3R is 25 m/s and is provided as a single variable for both the frequencies. It is based on an acceptable maximum measurement range of 30 km. This range will provide adequate spatial coverage and Nyquist velocity range for precipitation retrievals. The unambiguous Doppler is achieved through the staggered-PRT pulsing scheme (Section 2.1). This scheme would mandate the use of clutter filters like GMAP-TD as explained in Chapter 2.

Table 6.1 lists the detailed technical specifications of the D3R system. The D3R provides several meteorological products as listed here for both the frequencies in NetCDF format (Rew et al., June 2011). The radar is also expected to provide science products such as specific differential phase, liquid water content profiles, hydrometeor identification, median drop diameter, instantaneous rain rate and the liquid drop number concentration in future. The D3R is a mobile transportable radar capable of faster set-up and tear-down times to facilitate its participation in science field campaigns. The radar can be operated remotely and powered on the Uninterrupted Power Supply (UPS) and generators in a secured site. All the subsystems of the radar

Table 6.1: D3R Radar Parameters

System	
Frequency	Ku: 13.91 GHz ± 25 MHz Ka: 35.56 GHz ± 25 MHz
Minimum detectable signal (Ku, Ka)	-10dBZ at 15 km for a single pulse at 150m range resolution
Minimum operational range	500 m
Operational range resolution	150 m (nominal)
Maximum range	30 km
Angular coverage	0-360° Az, -0.5-90° El (full hemisphere)
Antenna	
Parabolic reflector (diameter)	6ft/72in (Ku), 28in (Ka)
Gain	44.5 dB (Ku, Ka)
HPBW	$\sim 1°$ (Ku, Ka)
Polarization	Dual linear simultaneous and alternate (H and V) (Ku, Ka)
Maximum sidelobe level	$\sim$ -25 dB (Ku, Ka)
Cross-polarization isolation	$<$ -32 dB (on axis)
Ka-Ku beam alignment	Within 0.2°
Scan capability	0-24°/s Az, 0-12°/s El
Scan types	PPI sector, RHI, Surveillance, Vertical pointing
Transmitter/Receiver	
Transmitter architecture	Solid state power amplifier modules
Peak power/Duty cycle	200 W (Ku), 1 W (Ka) per H and V channel, Max duty cycle 30%
Receiver noise figure	4.6 (Ku), 5.5 (Ka)
Receiver dynamic range	$\geq$90 dB (Ku, Ka)
Clutter suppression	GMAP-TD
Data Products	
Standard products	Equivalent reflectivity factor Z_h (Ku, Ka), Doppler velocity (unambiguous: 25 m/s) ν, spectrum width σ_ν
Dual-polarization products (Ku, Ka) (LDR only in alternate transmit mode)	Differential reflectivity Z_{dr} Differential propagation phase ϕ_{dp} Copolar correlation coefficient ρ_{hv} Linear depolarization ratios LDR_h, LDR_v
Data format	NetCDF

are designed to survive severe thermal (+40 °C to -40 °C), precipitation and wind regimes.

6.1.3 Engineering considerations

The unique requirements on the performance of the D3R system have led to several ingenious design decisions in every subsystem. The major engineering design considerations are as follows.

Aligned antennas: An important engineering aspect of a dual-frequency system is the level of integration of antennas with the pedestal and transceiver hardware. This can range from a design where two separate radar units operate independently to the one that employs a common reference system for dual transmitters on a single dual-frequency aperture. The first generation version of the D3R falls somewhere in the middle, i.e., a common platform transmitter illuminating two distinct but aligned antennas (Figure 6.1). These antennas have been manufactured by the Seavey Divi-

Figure 6.1: D3R deployed at Southern Great Plains (SGP) site of the Department of Energy (DoE) Atmospheric Radiation Measurement (ARM) program during the GPM Midlatitude Continental Convective Clouds Experiment (MC3E) (May 28, 2011).

Figure 6.2: The pedestal for the D3R system is provided by the Orbital Systems, Ltd. It has evolved from a satellite tracking pedestal.

Figure 6.3: The D3R pedestal is mounted on a trailer that can be towed by a van-sized vehicle. This photograph was taken on Dec 09, 2010 during the antenna assembly phase at CSU-CHILL site.

sion of the Antenna Research Associates, Inc. (ARA, 2012). There are future plans to migrate to a single aperture system. The D3R pedestal is provided by the Orbital Systems (Orbital Systems, 2012)(Figure 6.2). It is mounted on a commercially available 16-ft trailer suitable for towing by a pick-up truck or a van-sized vehicle as shown in Figure 6.3.

Solid-state transceiver: Rain-profiling and reliable detection of cross-pol rain backscatter demand substantially higher peak power. One of the novel aspects of D3R is that it employs a solid-state transceiver which can considerably enhance the sensitivity of the radar by also allowing implementation of pulse compression (Bharadwaj et al., 2009). Furthermore, the use of a solid-state transmitter also enables the deployment of D3R at very different and extreme climatic locations. The solid-state transceiver system has been designed by the Remote Sensing Solutions, Inc. (RSS, 2012) for both the frequencies and supports an extremely widebandth up to 50 MHz. The multi-channel digital receiver and signal processor which implement frequency-diversity pulse compression have been used for D3R along with a programmable digital waveform generator (George et al., 2010).

Rotating and non-rotating subsytems: The transceivers, IF electronics, waveform generator and digital receivers are mounted on the back of the respective antennas as shown in Figure 6.1. These subsystems form the rotating subsystems of the radar. The time series and positioner data is transferred to the dedicated moment generation servers through two fiber-optic Gigabit links over the slip rings. These servers provide the processed data to remote and local real-time displays, remote dual-frequency derived products server and a data archiving node. The entire system is configured and commanded by a system controller node.

Retrieval algorithms: The dual-frequency dual-polarization operation at higher frequencies involves non-Rayleigh scattering mechanisms and presents different precipitation signatures compared to the conventional S- or C- band observations. Indeed, most of the engineering challenges stem from making precipitation measure-

ments on the ground at a highly attenuating frequency. For instance, the traditional dual-pol DSD retrieval algorithms for ground-based radar using Φ_{dp} are not suitable at Ka-band. In order to support the development, extensive numerical evaluations have been carried out to document the extinction statistics of propagation through precipitation and new parameter retrieval techniques by combining dual-frequency and dual-polarization observations have been investigated (Le et al., 2009).

6.1.3.1 System architecture

Figure 6.4 shows a simplified block diagram of the D3R system. The radar has physically separate hardware for the transceivers of Ku- and Ka-band frequencies. The programmable digital waveform generator upconverts the frequency-diversity waveform to the IF stage. In the actual system, the IF filters and mixers are in two-stages on both the transmitter and receiver hardware. The first IF is 220 MHz and the second IF is 140 MHz in the receiver chain. The STALO output is passed through a splitter (not shown in the block diagram) to the mixers of H- and V-polarization chains to translate the signal from the IF to RF.

The solid-state power amplifiers (SSPA) drive this RF signal to the directional couplers which send the signal to the waveguide-coax interface of the latching circulators connected to the antenna waveguide ports. The other port of the directional coupler is interfaced to the calibration receiver channel which provides option for sampling the transmit pulse and also injecting output of the noise sources (through a Single-Pole-Single-Throw or SPST switch) to the receiver. The waveform generator also has RS-485 interface with the transceiver board to provide digital control for the SSPAs. At the receiver, the output of the calibration channel and the antenna waveguide port are selected through a Single-Pole-Double-Throw or SPDT switch and fed to a Low Noise Amplifier (LNA) which has a gain of the order of 20-22 dB. Separate digital receivers for Ku- and Ka-band subsample the 140 MHz IF signal at ADc sampling frequency of 200 MHz. The raw I-Q time series output of the digital

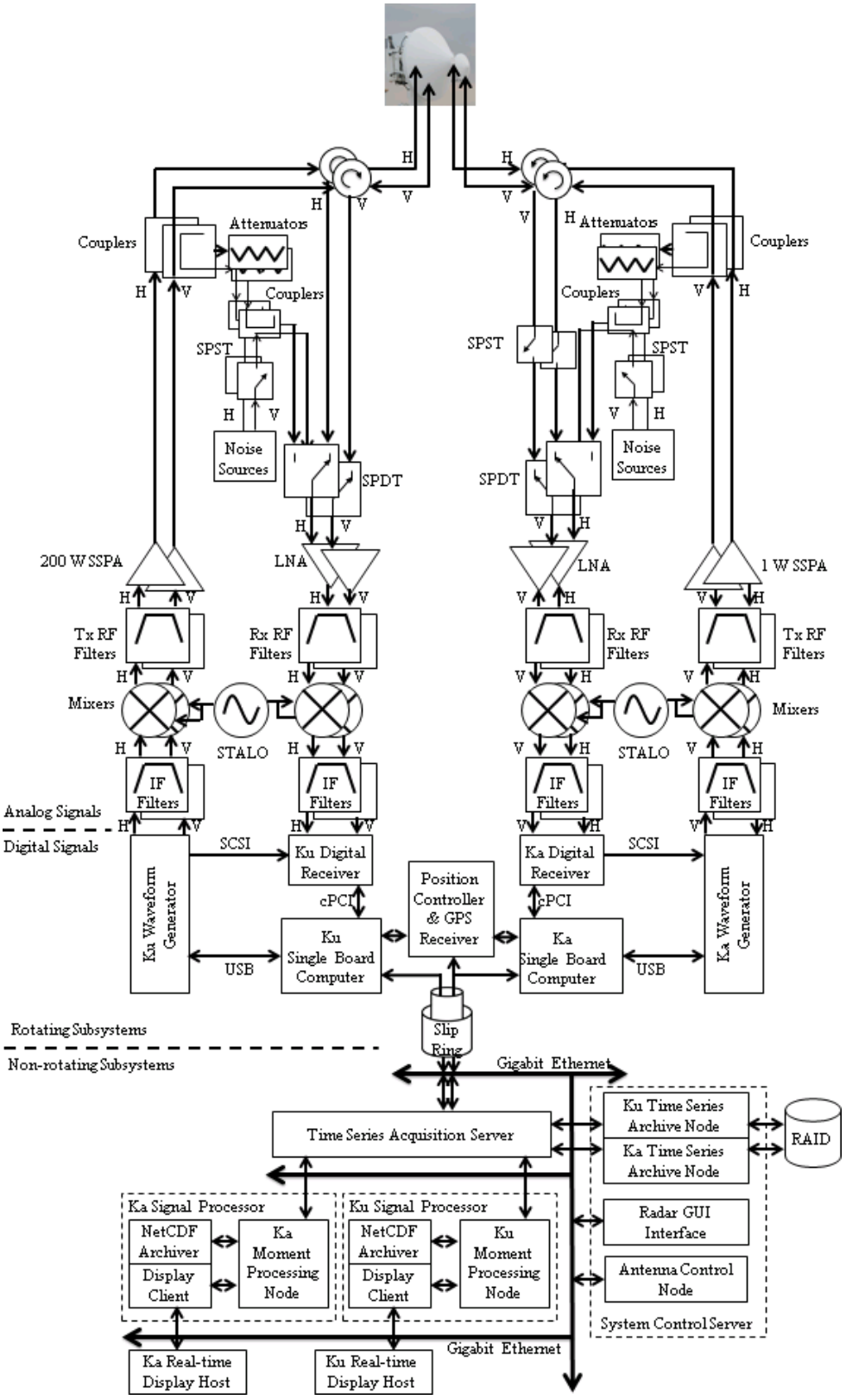

Figure 6.4: Simplified block diagram of the D3R system. The details of the system controller, IF stages, waveguide-coax interfaces, STALO splitters, transceiver RS-485 board and the dual-frequency server are omitted from the diagram.

receivers is sent to a Time Series Acquisition and Distribution Server over the slip rings. The signal processors and other nodes connect to the Time Series Acquisition and Distribution Server to perform various functions as discussed in Section 5.1. The comunication between most of the subsystems is through a Gigabit Ethernet link. In practice, this is accomplished through a network switch.

The conceptual design of the D3R system also envisions a dual-frequency server which will receive the products from both Ku- and Ka-moment servers to compute derived science products. Also, in practice, the system controller server is able to communicate with several subsytems which include the Power Distribution Unit (PDU) (not shown in the block diagram). A Graphic User Interface (GUI), currently under development, at the system controller node provides options to control and report the status of the system.

6.2 Evaluation of D3R antenna performance

The performance of the D3R antenna is of critical importance for accurate dual-polarization measurements. Low copolar and cross-polar sidelobe levels and high polarization purity in the main lobe are essential to avoid contamination from ground clutter and targets outside the HPBW view. Further, slight copolar pattern mismatch can cause considerable bias in the measurement of Z_{dr}, especially in areas of strong reflectivity gradients. The cross-polar performance of the antenna also determines the bounds on the measurable LDR.

The integrated cross polar ratio is closely related to the LDR limit of the system. The D3R has a requirement of 32 dB cross-polar isolation. If, f_{co} and f_{cx} are gain-normalized co- and cross-polar power patterns respectively, then the $ICPR_2$ (or the two-way $ICPR$) calculated by integrating over the entire pattern. For practical purposes, integration over the main beam (null-to-null) only will suffice. For any

Φ-plane (Brunkow et al., 2000):

$$ICPR_2 = 10\log_{10}\frac{\int f_{co}f_{cx}\sin\theta d\theta}{\int f_{co}^2\sin\theta d\theta} \tag{6.4}$$

In practice, the LDR bounds are also calculated by integrating over the main beam (null-to-null) only. The "vh" and "hv" bounds are normalized by the horizonatl (f_h) and vertical (f_v) copolar power pattern respectively (Chandrasekar and Keeler, 1993). The corresponsing cross-polar pattern are given by $f_{\epsilon v}$ and $f_{\epsilon h}$ respectively. The lower bound is calculated by reversing the sign of the radical term in the numerator. For instance, in any Φ-plane, (Bringi and Chandrasekar, 2001, Eq. 6.29):

$$LDR_{vh}^{ub} = 10\log_{10}\frac{\int (f_h f_{\epsilon v} + f_v f_{\epsilon h} + 2\sqrt{f_h f_v f_{\epsilon h} f_{\epsilon v}})\sin\theta d\theta}{\int f_h^2\sin\theta d\theta} \tag{6.5}$$

Also, in practice, the Z_{dr} bias error is calculated by integrating over the main beam (null-to-null) only. For any Φ-plane (Bringi and Chandrasekar, 2001, Eq. 6.25):

$$Z_{dr} = 10\log_{10}\frac{\int f_h^2 d\theta}{\int f_v^2 d\theta} \tag{6.6}$$

The pattern mismatch is then given by $1 - Z_{dr}$.

The figure of merit for the beam match between Ku- and Ka-patterns is given by the dual-frequency ratio (DFR). In practice, it is calculated by integrating over the main beam (null-to-null) only. For any Φ-plane,

$$DFR = 10\log_{10}\frac{\int f_{co(Ku)}^2 d\theta}{\int f_{co(Ka)}^2 d\theta} \tag{6.7}$$

The requirements on the D3R antenna performance are therefore very stringent. They are summarized in Table 6.2.

Figures 6.5-6.6 show the copolar patterns of Ku- and Ka-band antennas for one of the four principal planes for horizontal polarization. The PSL are observed to be

Table 6.2: Desired performance of the D3R antenna (both frequencies)

Performance parameter	**Desired performance**
Gain	44.5 dB
Half-power beam width	$\leq 1^\circ$
Copolar mismatch	$\leq 5\%$
Cross-polarization isolation	$\geq$ 32 dB
Peak sidelobe level (PSL)	$\geq$ -25 dB
Sidelobe envelope	Monotonically decrease from $\geq$ -25 dB within 2° of HPBW to $\geq$ -35 dB within 15°
Sidelobe level at all angles	$\geq$ -38 dB
DFR (linear)	$\sim$1

within -25 dB, the antenna gain $\geq$ 44.5 dB and the HPBW $\leq$1°. The -30° to +30° copolar plots (Figures 6.7-6.8) show the monotonically decreasing sidelobe envelope satisfying the requirements enlisted in Table 6.2. Figures 6.9-6.10 show wide-angle plots of these copolar patterns. It can be seen that the sidelobe levels at all angles are within the -38 dB limit. The cross-polar performance plots for one of the principal planes are shown for the center frequencies in Figures 6.11-6.12. The $ICPR_2$ calculated for the Ku- and Ka-band for these figures is -35.88 dB and -35.19 dB respectively. Figures 6.13-6.14 show the dual-frequency copolar and cross-polar plots. The D3R antenna meets most of the requirements enlisted in Table 6.2 without any major non-compliance.

6.3 Waveform design perspective and simulations

As explained in Chapters 1-2, several considerations should be taken into account for the waveform design for solid-state transmitter radars. The D3R system has its own unique requirements which adds up on these factors as listed below. The sensitivity requirement of -10 dBZ at 15 km for both frequencies at 150 m resolution calls for an improved design of the pulse compression waveform and the receiver filter as explained in Chapter 4. For the Ku- and Ka-band systems of D3R, the Figures 6.15-6.16 exhibit the trade-off between the chirp bandwidth B and sampling

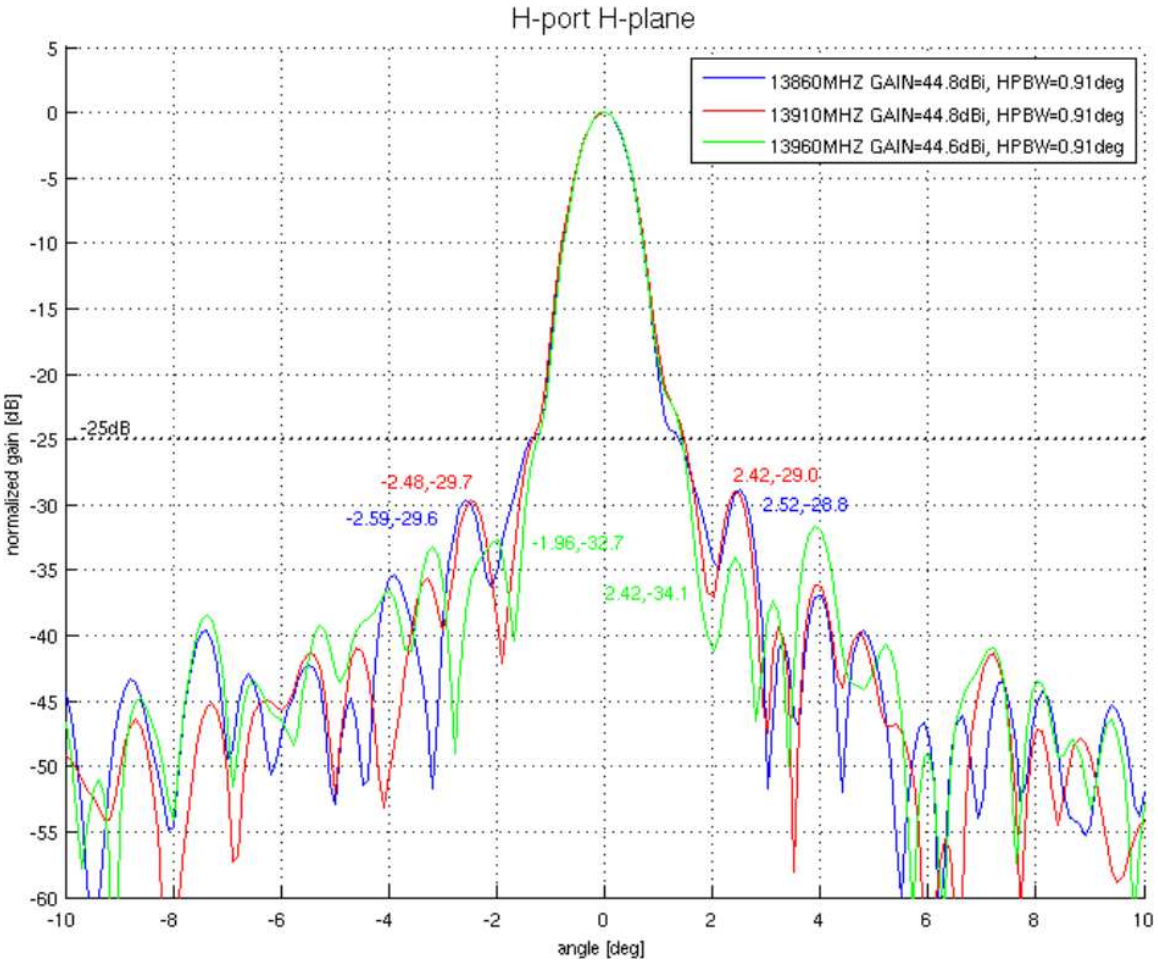

Figure 6.5: Copolar plots for the Ku-band antenna for the H-plane of the horizontal polarization port for the center and corner frequencies (±25 MHz). The PSL are well within -25 dB (Courtesy: GSFC, Feb 2010).

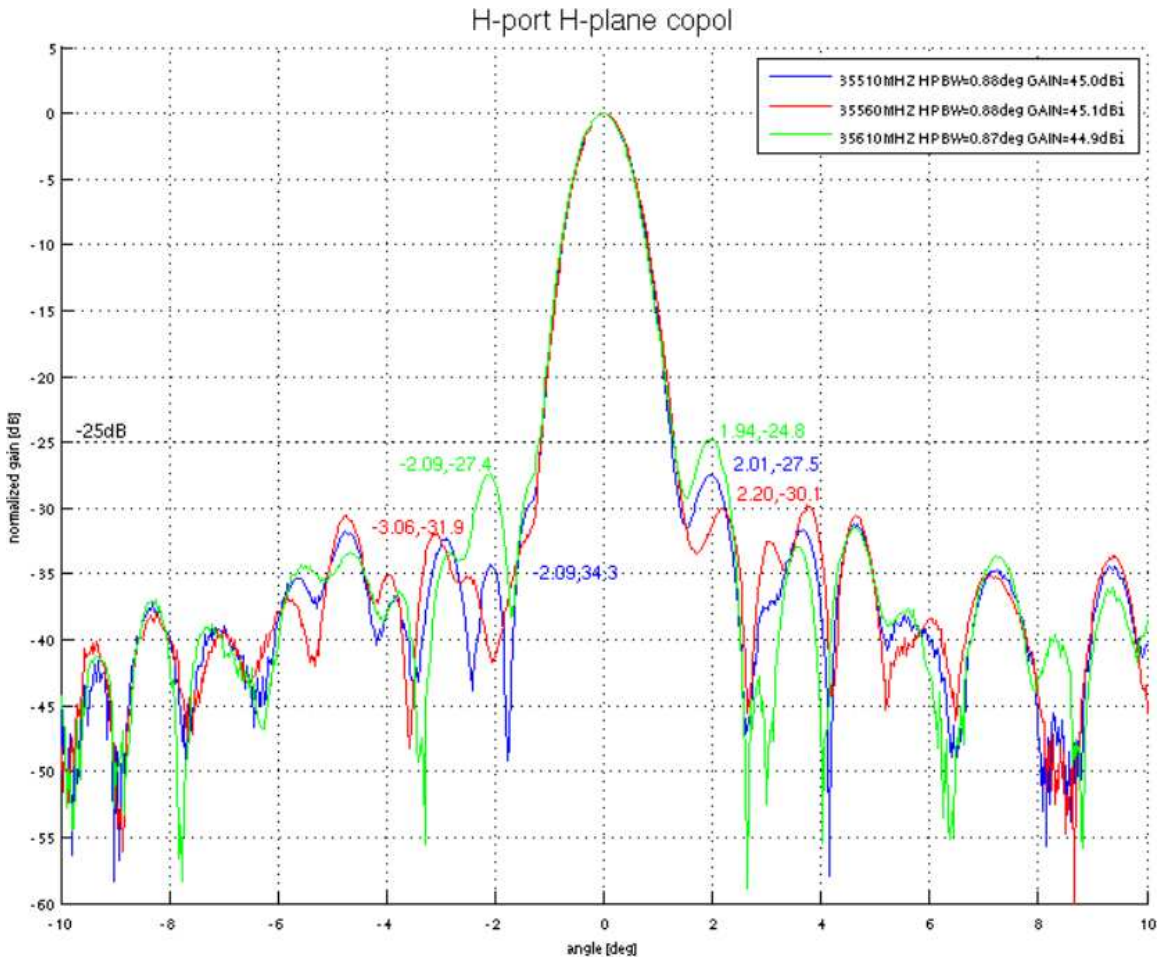

Figure 6.6: Copolar plots for the Ka-band antenna for the H-plane of the horizontal polarization port for the center and corner frequencies (±25 MHz). The PSL are well within -25 dB (Courtesy: Seavey/ARA, Apr 2010).

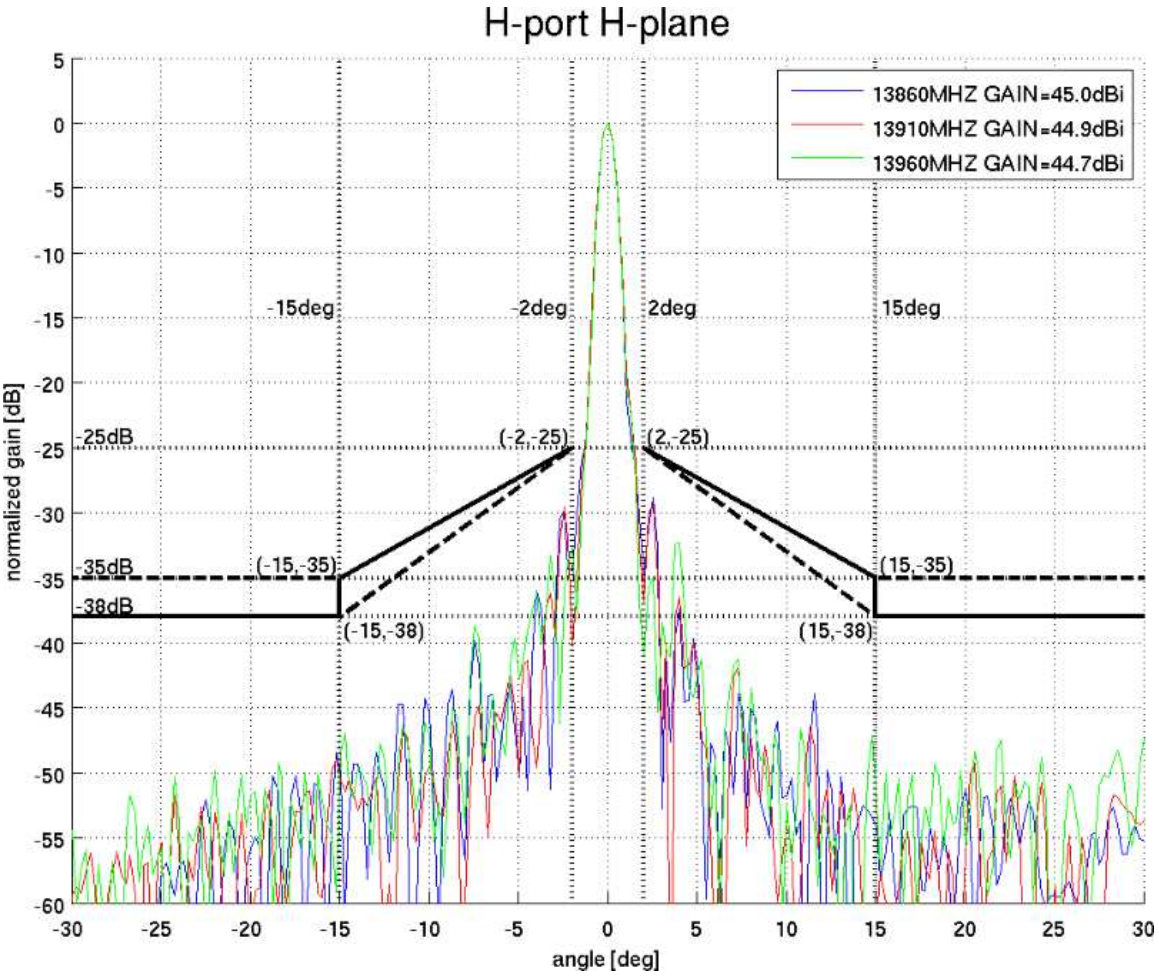

Figure 6.7: The -30° to +30° copolar plots for the Ku-band antenna for the H-plane of the horizontal polarization port for the center and corner frequencies (±25 MHz) showing the sidelobe envelopes (Courtesy: GSFC, Feb 2010).

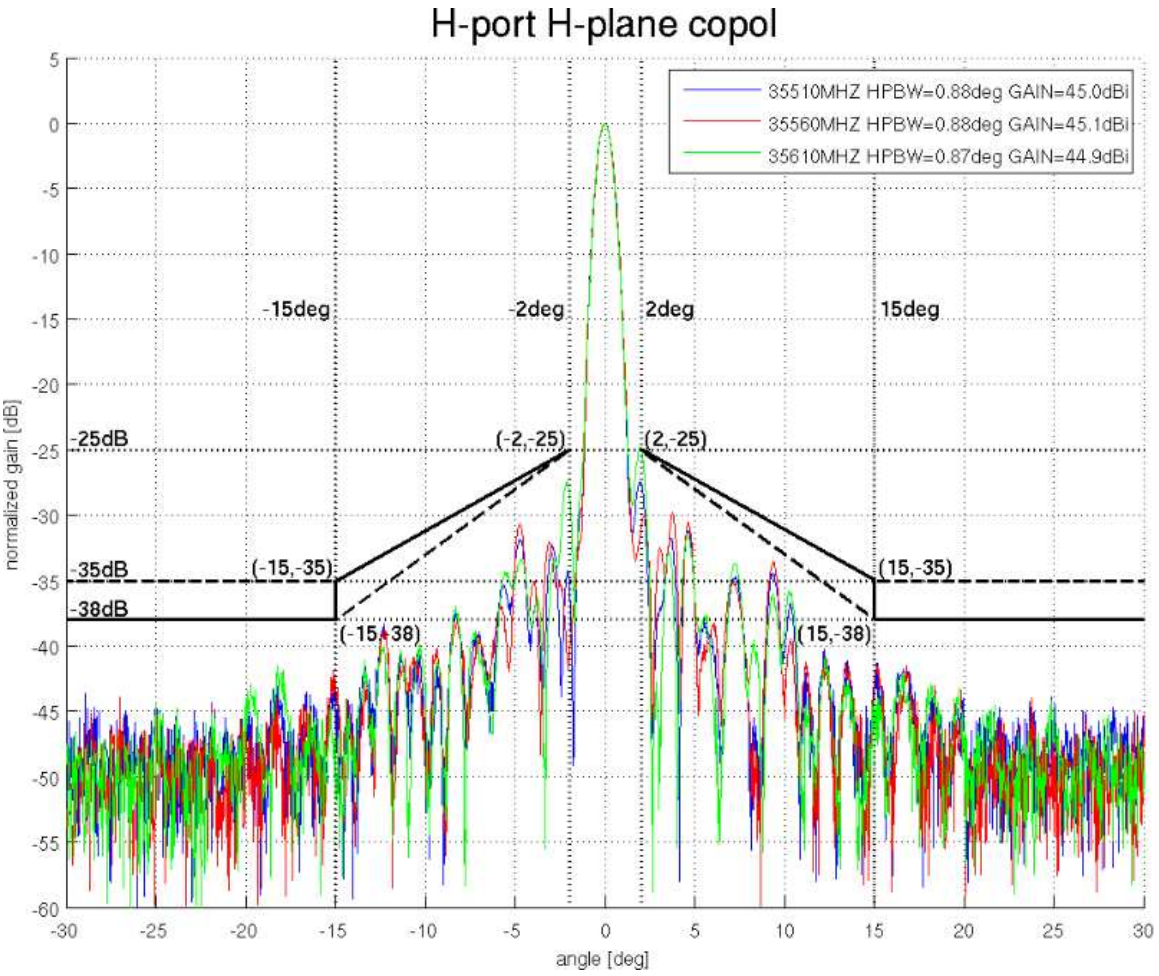

Figure 6.8: The -30° to +30° copolar plots for the Ka-band antenna for the H-plane of the horizontal polarization port for the center and corner frequencies (±25 MHz) showing the sidelobe envelopes (Courtesy: Seavey/ARA, Apr 2010).

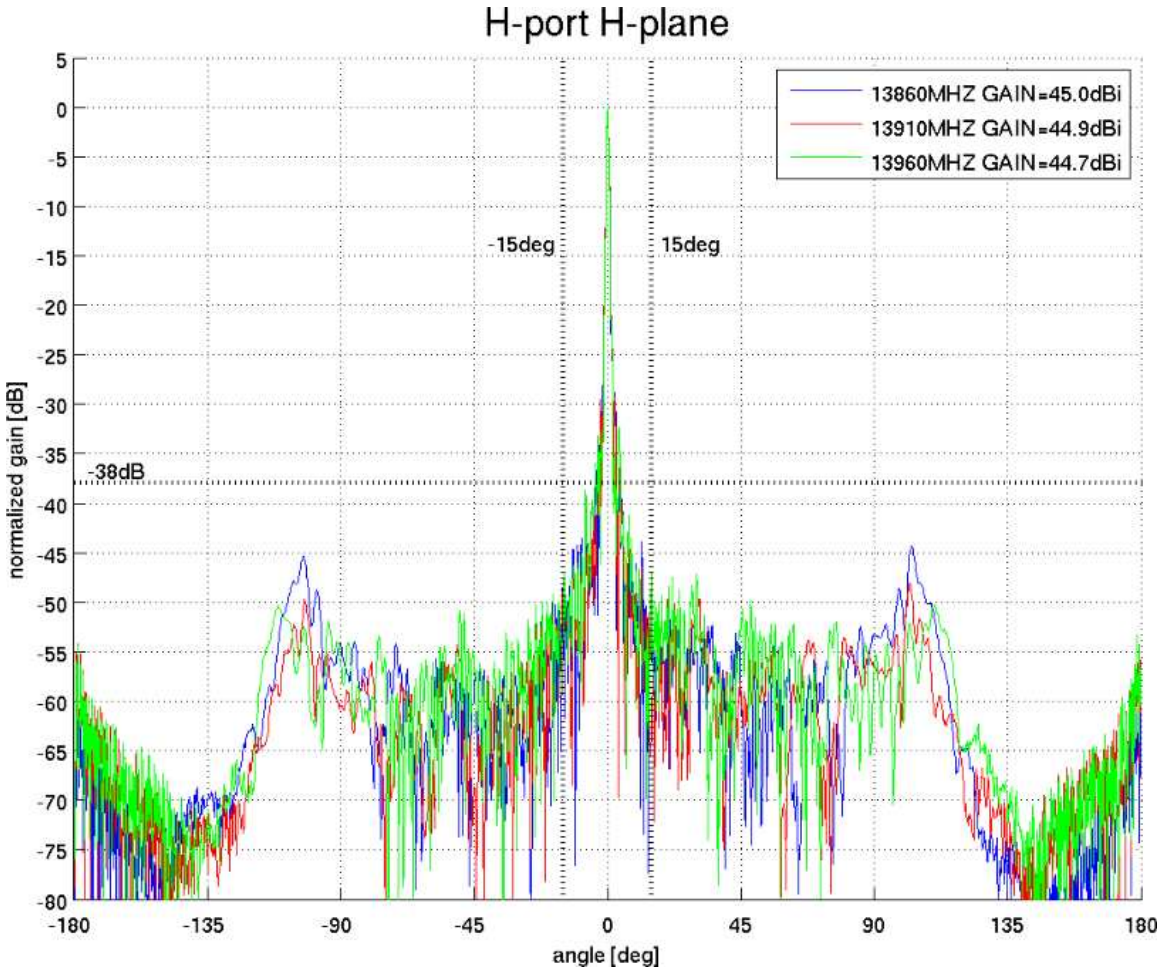

Figure 6.9: The wide-angle copolar plots for the Ku-band antenna for the H-plane of the horizontal polarization port for the center and corner frequencies (±25 MHz) showing the sidelobe levels at all angles (Courtesy: GSFC, Feb 2010).

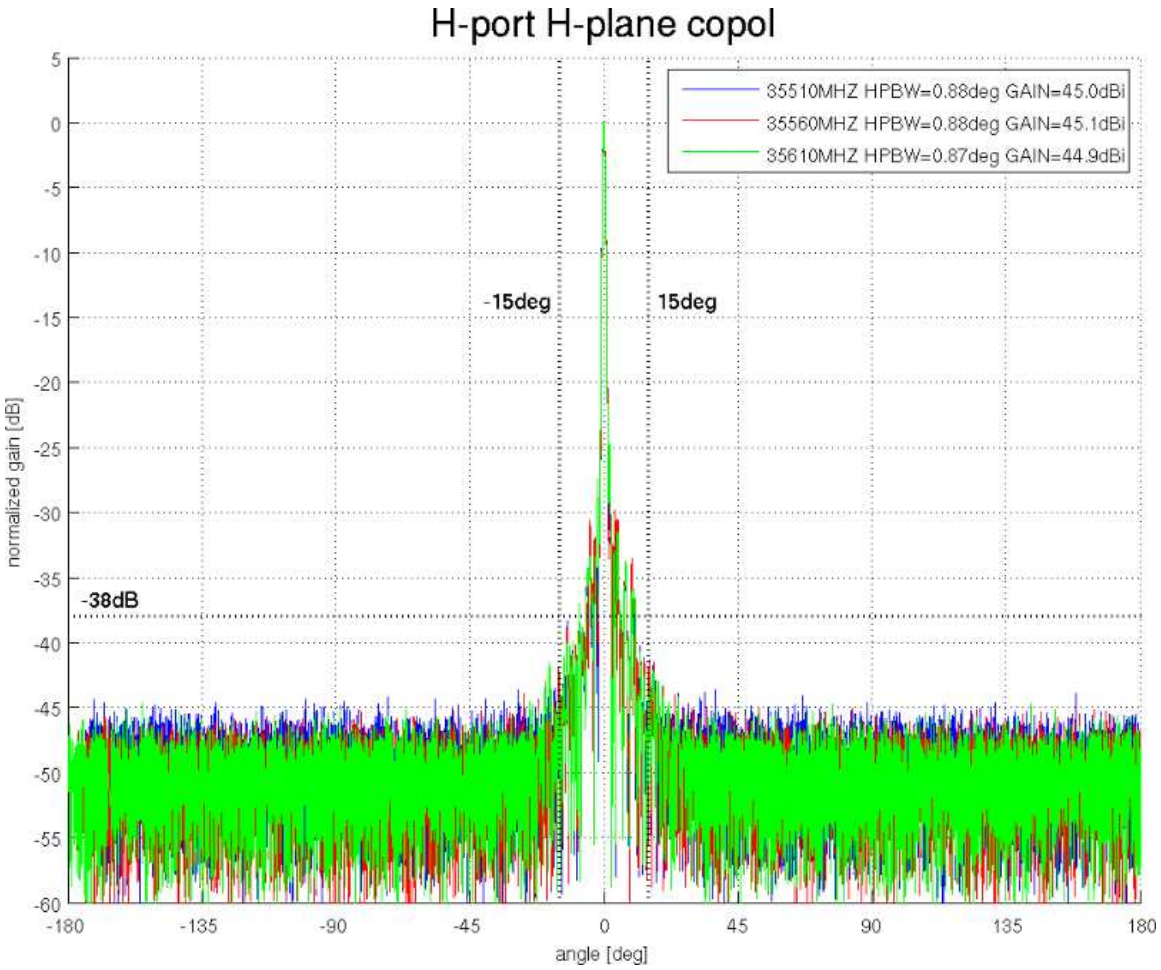

Figure 6.10: The wide-angle copolar plots for the Ka-band antenna for the H-plane of the horizontal polarization port for the center and corner frequencies (±25 MHz) showing the sidelobe levels at all angles (Courtesy: Seavey/ARA, Apr 2010).

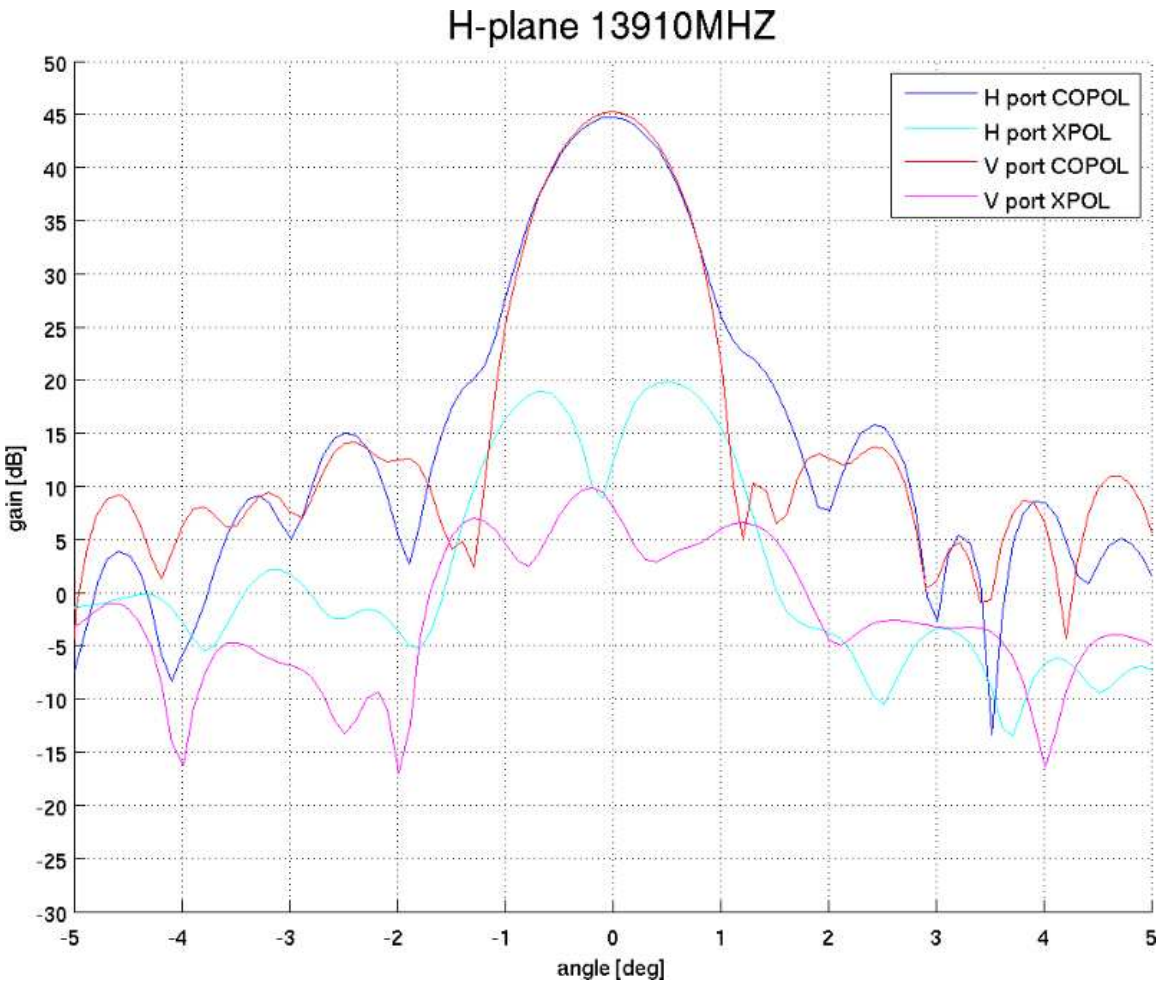

Figure 6.11: The copolar and cross-polar patterns for the Ku-band antenna for the H-plane of the center frequency (Courtesy: GSFC, Feb 2010).

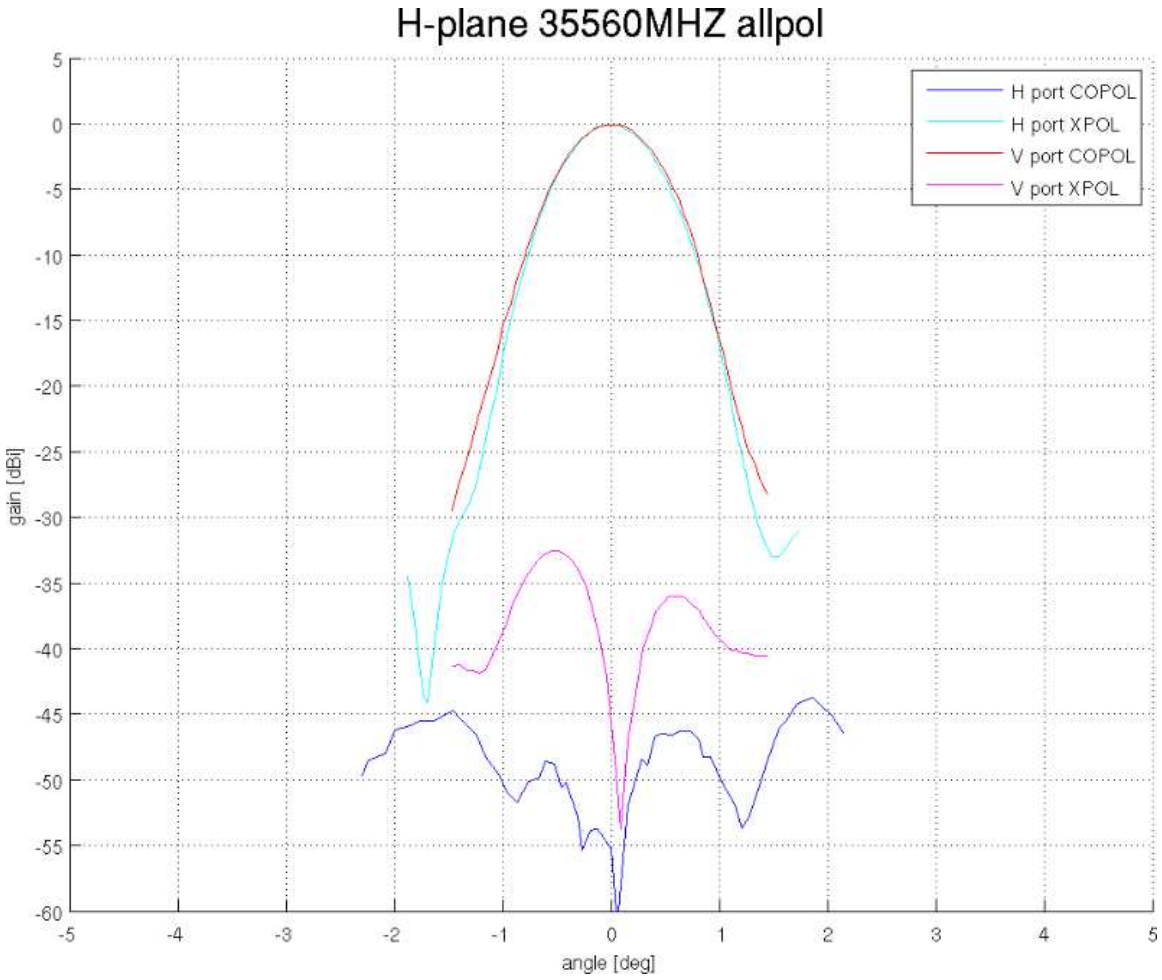

Figure 6.12: The copolar and cross-polar patterns for the Ka-band antenna for the H-plane of the center and corner frequency (Courtesy: Seavey/ARA, Apr 2010).

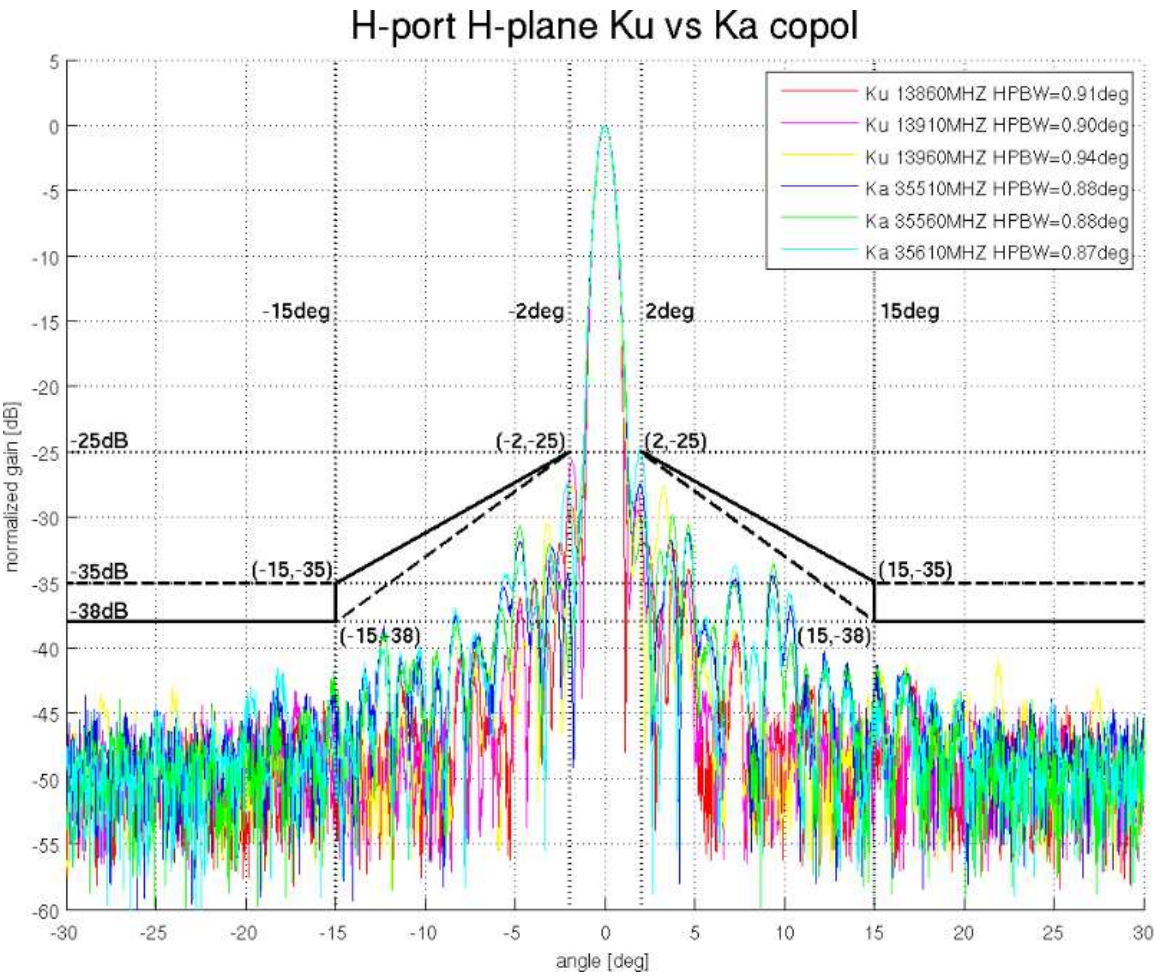

Figure 6.13: The copolar patterns for theKu- and Ka-band antenna for the H-plane of the horizontal polarization port for the center and corner frequencies (±25 MHz). The measured DFR is ∼1 on linear scale. (Courtesy: GSFC, Feb 2010).

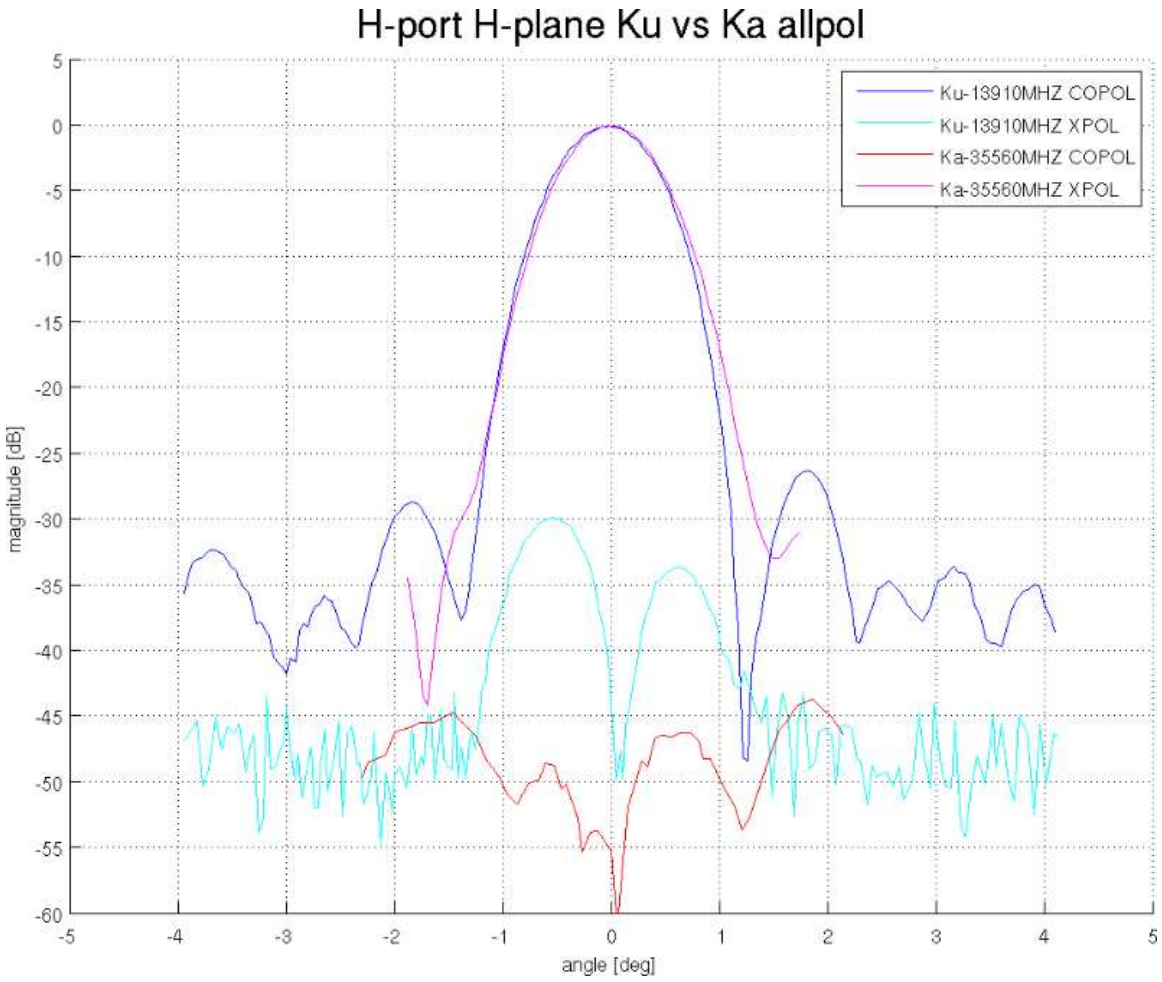

Figure 6.14: The copolar and cross-polar patterns for the Ku- and Ka-band antenna for the H-plane of the horizontal polarization port for the center frequency (Courtesy: Seavey/ARA, Apr 2010).

frequency f_s to achieve the required values of sensitivity at 15 km for the long subpulse channel. A reflectivity profie is used to simulate the performance of the frequency-

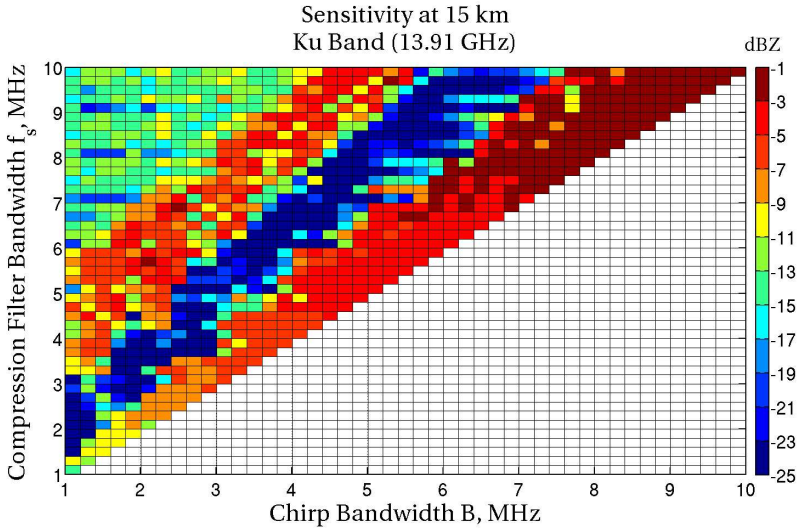

Figure 6.15: Sensitivity of Ku-band system at 15 kms shown as a function of the sampling frequency f_s and chirp B for a 40 μs pulse.

diversity waveform for the Ku-band system, as shown in Figure 6.17. The simulation results show that for a typical reflectivity profie, the frequency-diversity waveform will retrieve the reflectivity at different ranges, including the blind-zone due to the longer pulses.

The other fundamental limitation of D3R requirements is the range velocity ambiguity. A higher pulse repetition time (PRT) causes an increase in maximum unambiguous range but a decrease in the maximum unambiguous velocity (Figure 6.18) as explained by Equation 1.7. The D3R has a maximum unambiguous Doppler requirement of 25 m/s. Figures 6.19-6.20 show the errors in estimating the standard and dual-polarized moments simulated using a uniform PRT of 500 μs for a Ku-band system. For a sample input weather profile, the figures show the errors for increasing clutter-to-signal ratios. It should be noted that the unambiguous Doppler requirement can not be met with the uniform PRT scheme for a sample profile with nominal meteorological products and acceptable clutter filtering performance. The

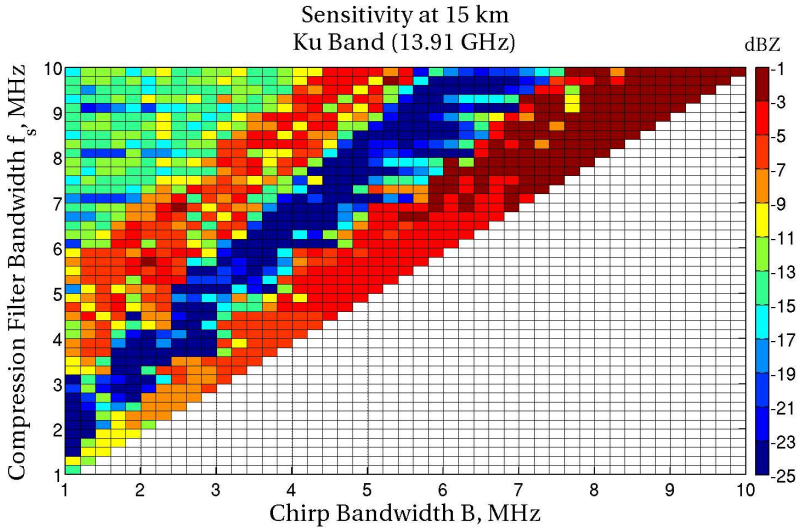

Figure 6.16: Sensitivity of Ka-band system at 15 kms shown as a function of the sampling frequency f_s and chirp B for a 40 μs pulse.

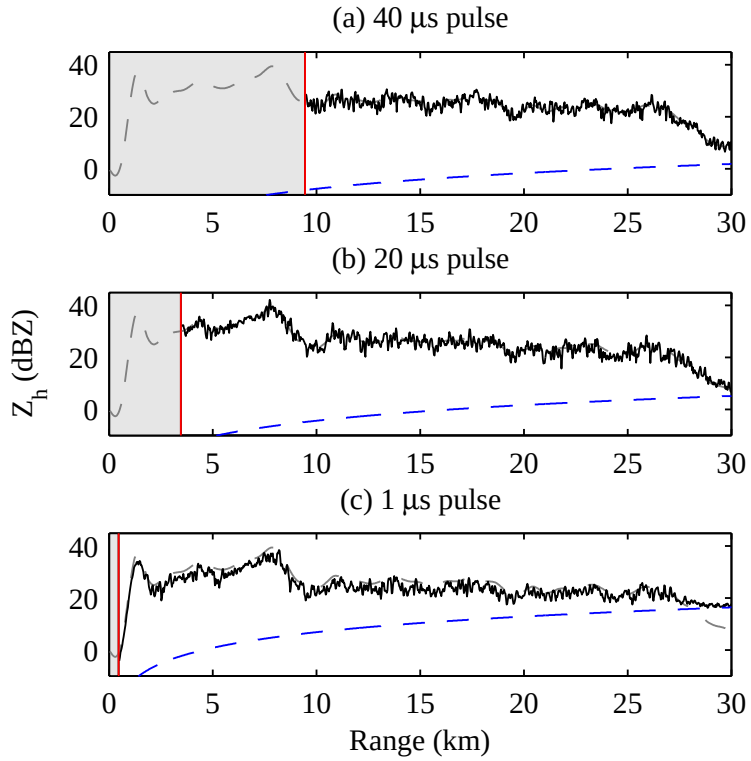

Figure 6.17: Simulation results for frequency-diversity waveform. Solid black line indicates measured reectivity, gray dashed line indicates true reectivity. Blue dashed line is the minimum detectable reectivity for each sub-pulse. Shaded region indicates blind zone. Data is from CSU-CHILL on June 7, 2003 during a bright-band event.

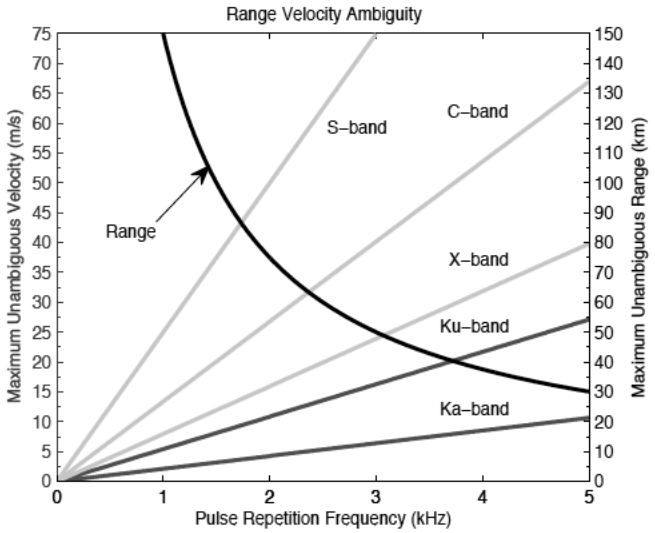

Figure 6.18: Maximum unambiguous range and maximum unambiguous velocity for different operating frequencies.

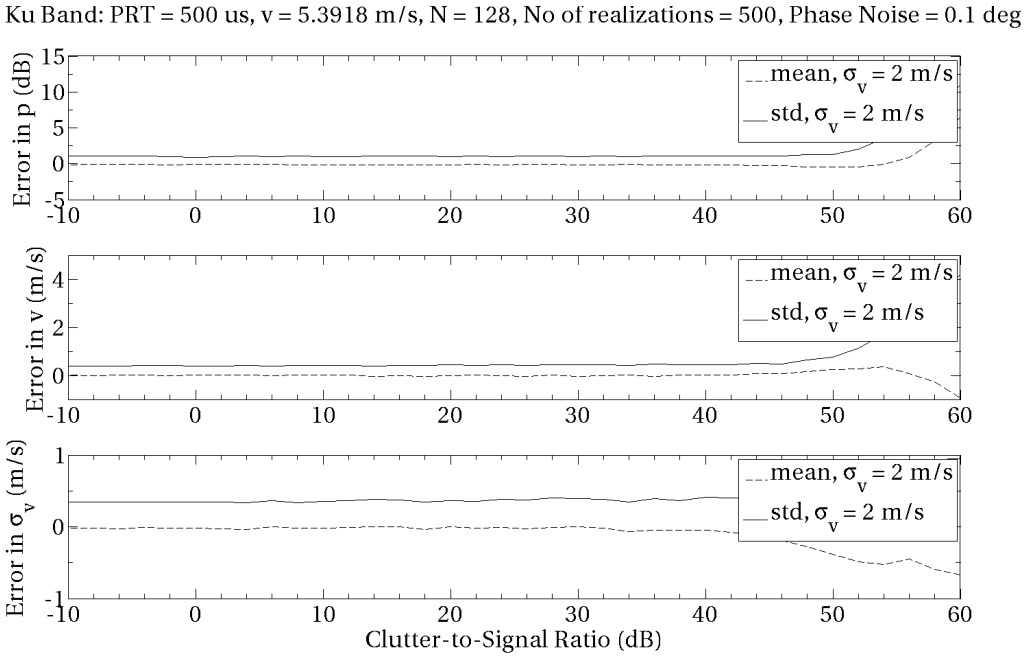

Figure 6.19: Errors in the standard moments for the uniform PRT pulsing for given clutter-to-signal ratio. The GMAP clutter filter was used in this simulation for a sample input weather profile with nominal SNR = 20 dB, spectrum width = 2 m/s, differential reflectivity = 0.75 dB, differential propagation phase = -50 ° and copolar correlation coefficient = 0.99. The number of samples used for integration is N = 128. and the unambiguous Doppler achieved is v.

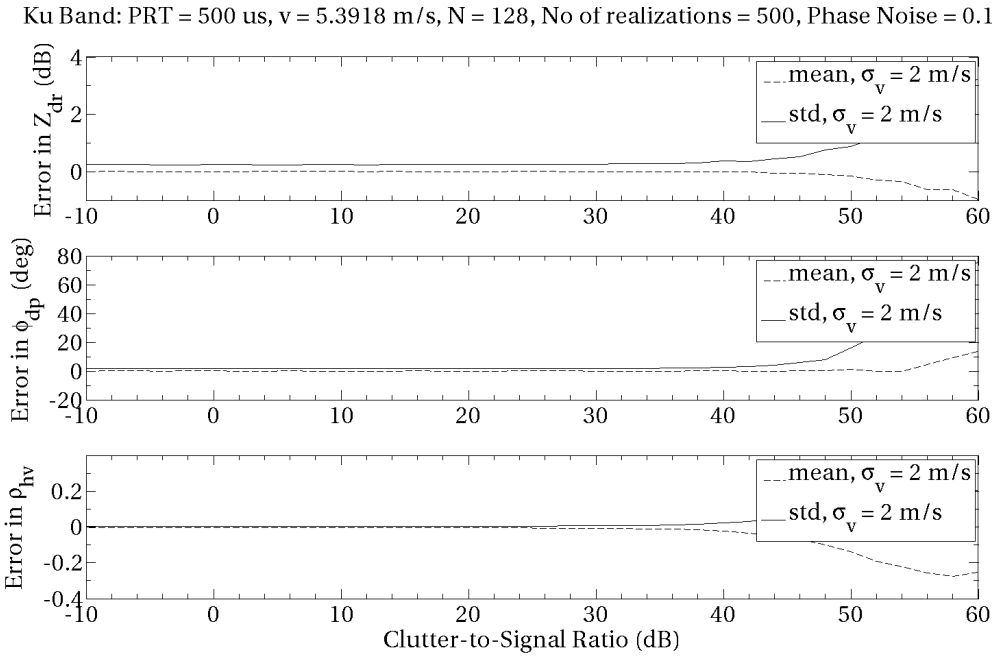

Figure 6.20: Errors in the dual-polarimetric moments for the uniform PRT pulsing for given clutter-to-signal ratio. The other parameters are same as in Figure 6.19.

unambiguous Doppler requirement can be met with the staggered-PRT pulsing which further requires clutter filters like GMAP-TD. Further phase coded waveforms are essential to suppress second-trip around echoes. The D3R employs staggered PRT 2/3 scheme with $T_u = 200$ μs (Figure 2.2) for both Ku and Ka-band in the simultaneous mode of operation. The equivalent PRF of 5 kHz in this case gives an unambiguous Doppler of 26.96 m/s at Ku-band and 10.55 at Ka-band. However, since the radar has the unambiguous Doppler limit of 25 m/s on *either* Ku- or Ka-band, this scheme is acceptable. The unambiguous range for this pulsing scheme is computed as 60 km which exceeds the instrumented limit of 30 km.

6.4 Summary

To meet its GPM science objectives, the D3R system is unique in its requirements, engineering design and algorithmic considerations. The use of the solid-state transmitters and the frequency-diversity digital receiver substantially improves the sensitivity of the radar. The design of the antenna subsystem guarantees improved

dual-polarization measurement. The radar is highly configurable at several processing stages and the entire system can be operated remotely. The results from the field deployment of the radar are now presented in the next chapter.

CHAPTER 7

FIRST FIELD OBSERVATIONS AND RESULTS

Since May 2011, the D3R radar has participated for deployment and data collection at several sites. During May-June 2011, it participated in the Midlatitude Continental Convective Clouds Experiment (MC3E) (Jensen et al., April 2010) at the Southern Great Plains (SGP) site of the U.S. Department of Energy (DOE) Atmospheric Radiation Measurement (ARM) Climate Research Facility at Ponca City, Oklahoma for the assessment of its mechanical deployment. During the Fall of 2011, the radar underwent several technical upgrades, evaluation and characterization at the CSU-CHILL site in Greeley, CO. During Jan-Feb 2012, the radar was successfully deployed at the Environment Canda site in Egbert (Ontario, Canada) to collect data for the GPM Cold-season Precipitation Experiment (GCPEx) (Skofronick-Jackson et al., Sep 2011).

This chapter chronologically presents the example D3R data collected during the above-mentioned campaigns to conclusively evaluate the digital receiver design.

7.1 General system performance

The first deployment of the digital receiver and the signal processor on D3R radar began with the MC3E campaign. The pulse compression filter performance and the capability of the signal processor to seamlessly merge the individual profiles were tested first. As explained in Chapter 4, the pulse compression filters and the corresponding waveforms were subsequently modified before the GCPEx campaign to

facilitate proper calibration. Figure 7.1 shows the pulse compression filter performance for the three subpulses as seen in the sampled transmit pulse of Ku-band digital receiver on Jan 03, 2012. This data was collected on a clear day at the CSU-CHILL site. Since the digital receiver in the Ka-band system is identical to that in the Ku-band, this performance is valid for both frequencies. The peak sidelobe suppression exceeds 45 dB for both the long and the medium subpulses.

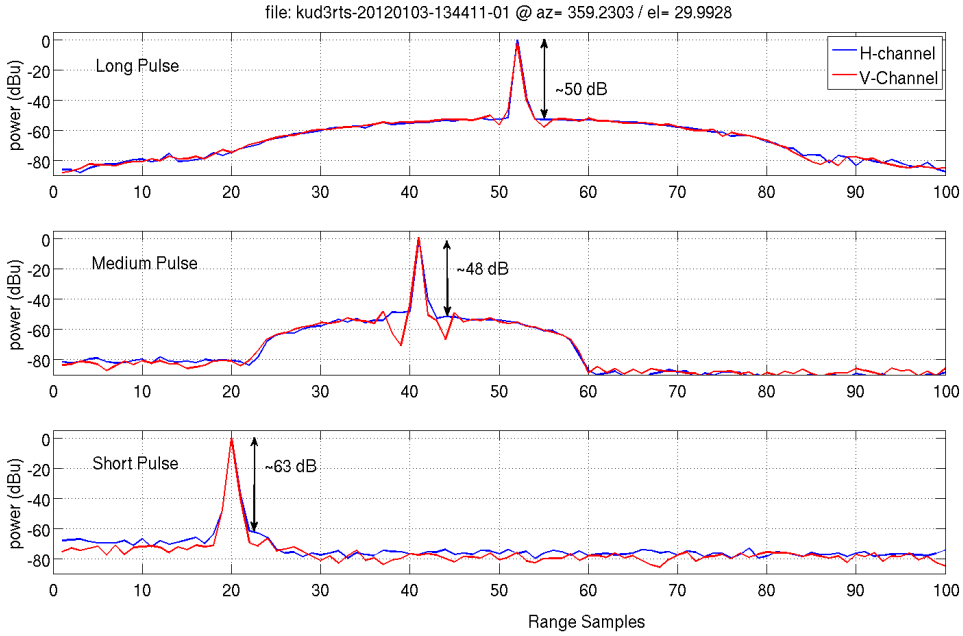

Figure 7.1: Pulse compression filter outputs as observed in the sampled Ku-band transmit pulse (Jan 03, 2012).

If the three subpulses simultaneously record the return signal from the same meteorological event, then for a calibrated radar system these echoes should not vary significantly. This enables the radar to accept all three returns as ground truth and merge the profiles based on a reasonable premise. Figure 7.2 shows the comparison of subpulse Ku reflectivity profiles for two sets of data. The top dataset shows the comparison of the three subpulses for a moderate precipitation event during the MC3E campaign in Oklahoma on May 31, 2011. The three subpulses record closely similar echoes for the precipitation beyond the blind ranges of the respective pulses (∼3 km

and ∼9 km for the medium and long pulses). The bottom dataset shows another comparison for the high signal-to-noise ratio (SNR) regions in the intermediate range of the D3R for the data collected for a moderate rain event at the CSU-CHILL site on Jul 16, 2011.

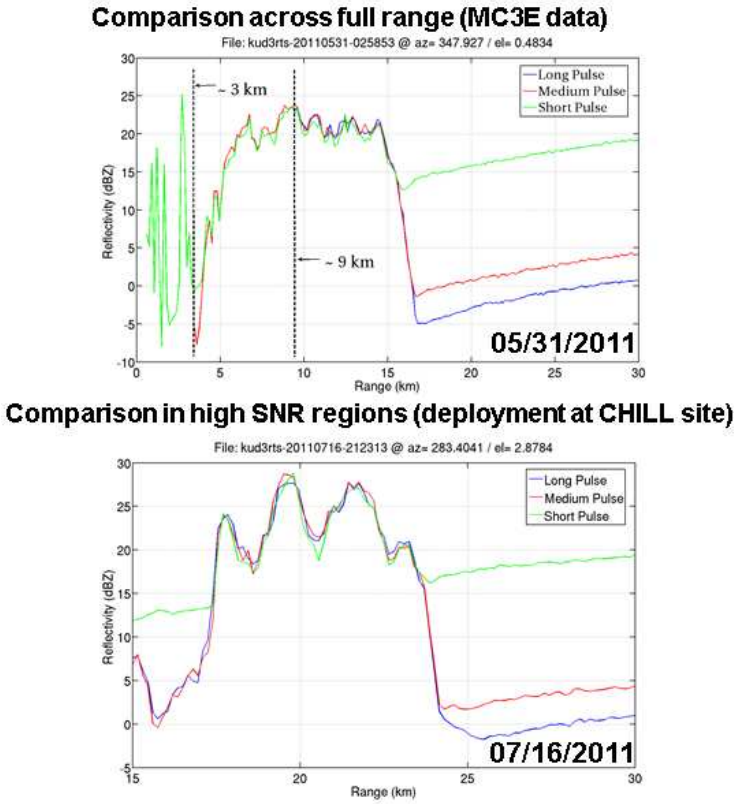

Figure 7.2: Comparison of Ku reflectivity profiles for the three subpulses.

The first observations of standard moments derived from merging the individual range profiles of the three subpulses are shown in Figure 7.3. The data has been thresholded for low SNR values and the estimates are based on pulse-pair method. The merged standard moments are continuous over the subpulse transition regions.

The output of the staggered PRT estimates of the Doppler velocities is shown in Figure 7.4 which compares simultaneous observations by CSU-CHILL S-Band radar and D3R for a rain event on Nov 1, 2011. The Ka-Band system was operating in only H-polarization during this event. The D3R data from different subpulses has

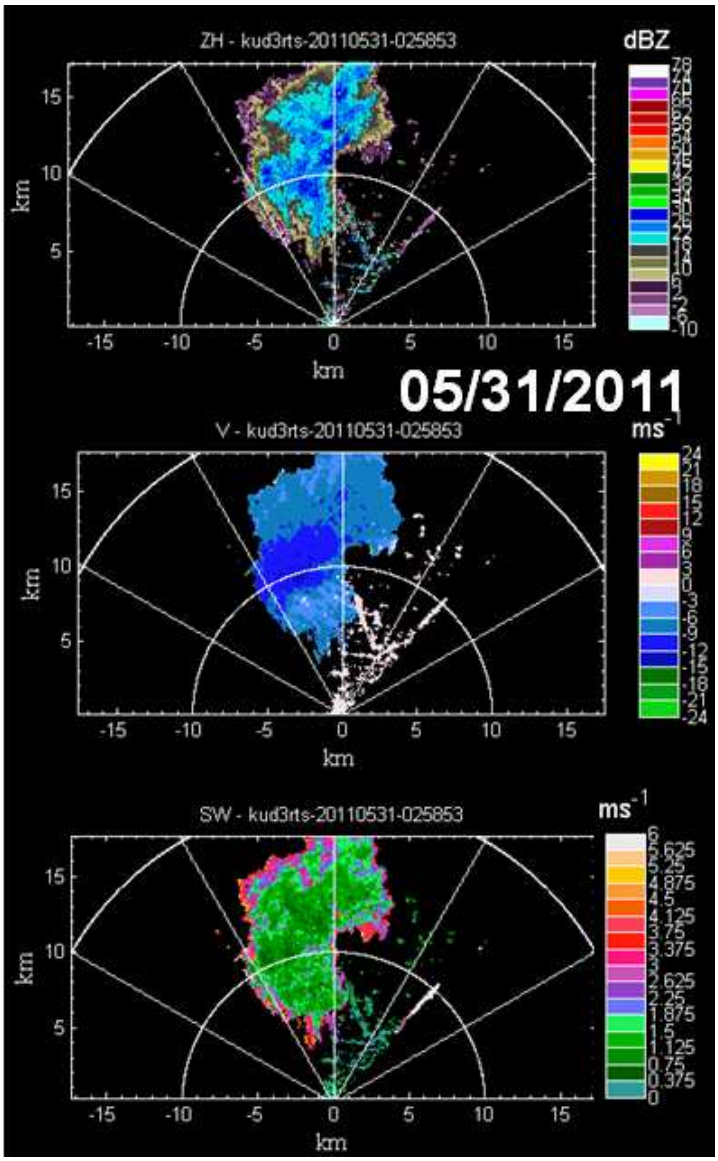

Figure 7.3: Standard moments after merging data from individual subpulses. Data obtained during D3R deployment in MC3E campaign on May 31, 2011. Standard pulse-pair estimates shown here have been thresholded for low SNR values after noise subtraction.

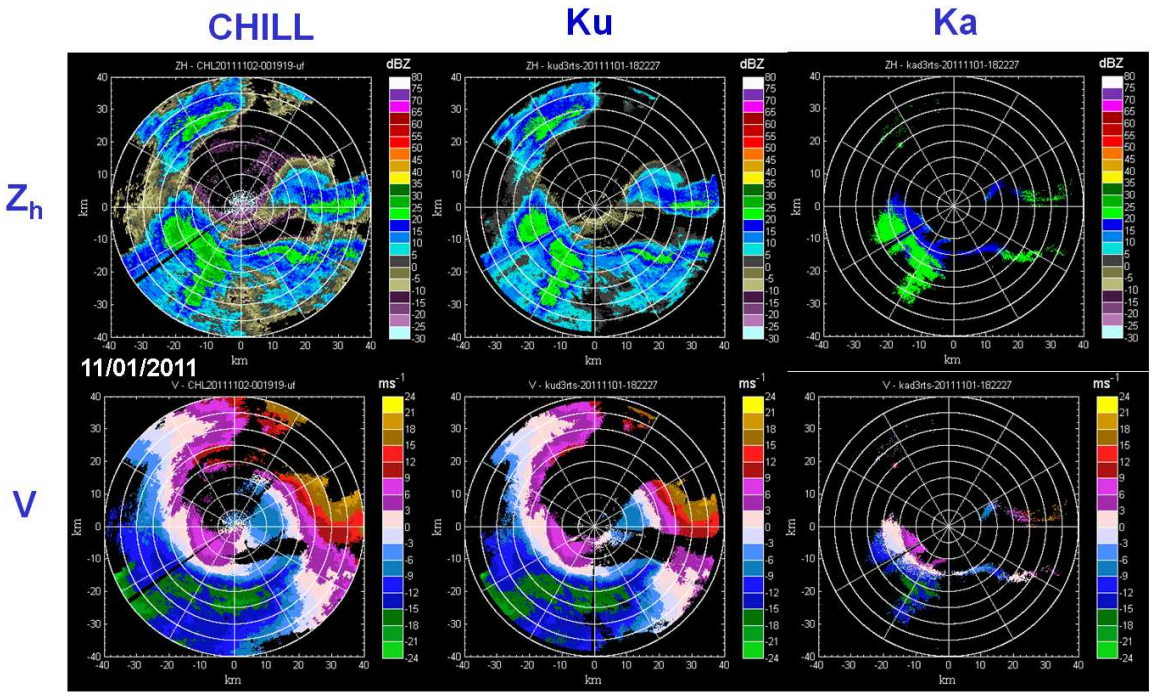

Figure 7.4: Simultaneous observations by CSU-CHILL S-Band radar and D3R for a rain event on Nov 1, 2011. Unfolded velocity estimates for D3R are based on 2/3 staggered PRT.

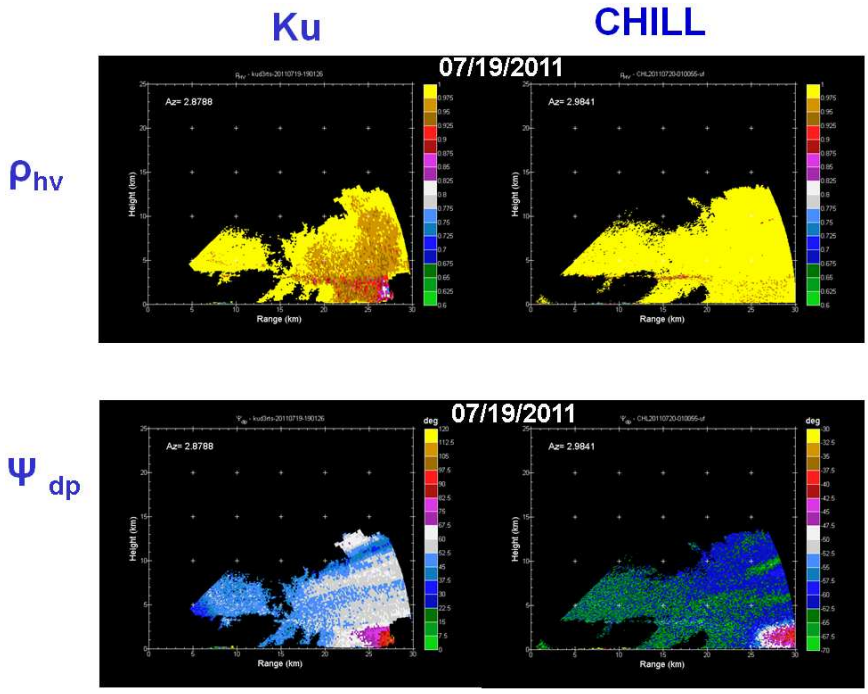

Figure 7.5: Comparison of ρ_{hv} and Ψ_{dp} in simultaneous observations of CSU-CHILL S-Band radar and Ku-Band system during a rain event on Jul 19, 2011.

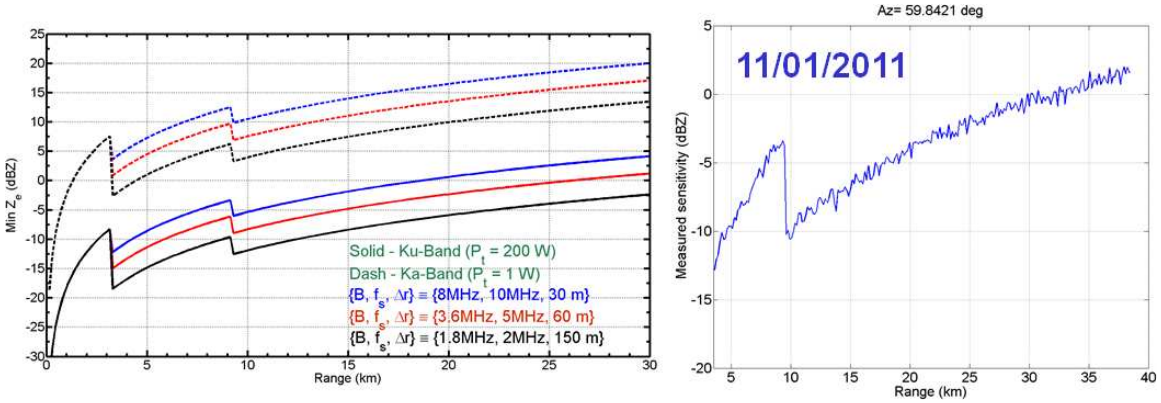

Figure 7.6: Observed Ku-band sensitivity as calibrated with CSU-CHILL S-band radar. Data is obtained during simultaneous operations of D3R and CHILL systems on Nov 1, 2011. This should be compared with the solid black line in the figure on the left.

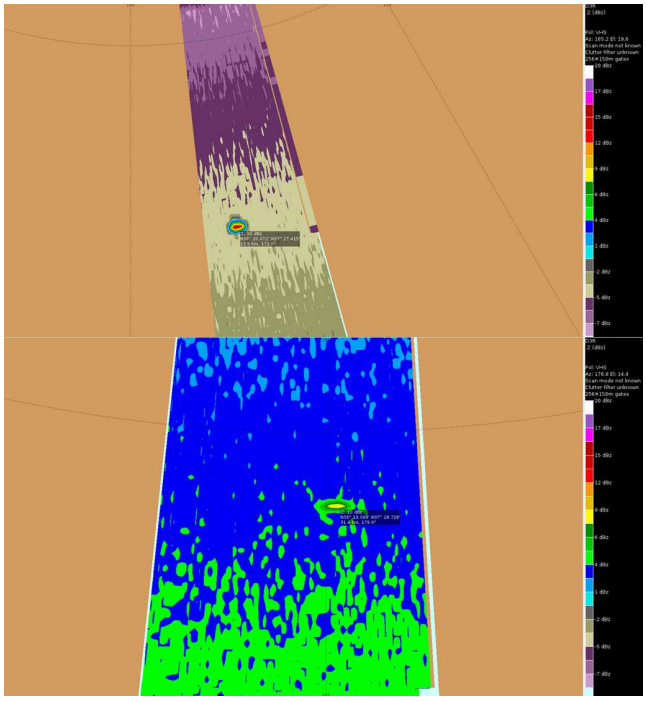

Figure 7.7: Top: Near (13.9 km) range observation on D3R real-time display during sphere calibration experiment at CSU-CHILL radar site on Sept 23, 2011. Bottom: The same observation at the far range (31.4 km).

been merged in range and the unfolded velocity estimates for D3R are based on 2/3 staggered PRT. The D3R data has been thresholded for low SNR values and noise correction has been applied. The Ka-band has the placeholder 1 W transmitter which explains the weaker echoes in this frequency. The reflectivity and velocity estimates of D3R show good match with the CSU-CHILL observations.

Figure 7.5 shows comparison of the estimates of dual-polarized products derived from the long pulse of the Ku-band with the CSU-CHILL observations of the same intense rain storm of Jul 19 2011. The D3R copolar correlation coefficient shown has been processed with the noise correction. The Ψ_{dp} range of D3R is three times larger than that of CHILL but the pattern of the two plots is similar indicating a difference of only the scaling factor.

The measured sensitivity of the radar can be compared with the theoretical or expected sensitivity. Such a comparison is shown in Figure 7.7 which compares the reflectivity estimated from the returns for a clear air case observed on Nov 01, 2011 at CSU-CHILL site with the expected sensitivity. For a high SNR region in the medium and long subpulses of the merged profile, this comparison for 150 m range resolution shows that the clear air measured reflectivity is slightly above -10 dBZ at 15 km (which is the expected sensitivity figure). Further, the Figure 7.7 shows the capability of the system to observe the metallic sphere during the sphere calibration experiment. The observations at the near (13.9 km) and far (31.4 km) ranges are shown and the observed maximum reflectivity for the sphere is 16 dBZ and 10 dBZ respectively.

7.2 Example data from GCPEx campaign

During the period Jan-Feb, 2012, the D3R was deployed at the Environment Canada (EC) Center for Atmospheric Research Experiments (CARE) site in Egbert, Ontario, Canada to participate in the GPM Cold-season Precipitation Experiment (GCPEx) (Figure 7.8). The goal of the GCPEx was to characterize the ability of

multi-frequency active and passive microwave sensors to detect and estimate falling snow through the collection of microphysical property data, associated remote sensing observations, and coordinated model simulations of falling snow. During the GCPEx

Figure 7.8: D3R deployed at Environment Canada (EC) Center for Atmospheric Research Experiments (CARE) site in Egbert, Ontario, Canada to participate in the GPM Cold Season Precipitation Experiment (GCPEx) (Jan 14, 2012).

campaign, the field worthiness of the D3R system was demonstrated through continuous and automated scans at a secure site in an extreme climatic regime. The real time display images of the radar observations were continuously self-archived on the NASA GCPEX portal. The radar was often operated remotely. The radar operation commenced on Jan 17, 2012 and continued uninterrupted until Mar 1, 2012 without any reported case of system breakdown (including at subzero temperatures reaching down to -20 °C). In the period of 45 days of active data collection, the radar archived about 20TB of raw time series data for 175 hrs of critical meteorological events for the field program. The robustness of the D3R to operate in stand-alone mode for ex-

tensive hours, including remote monitoring of system health, was essentially proven during the GCPEx campaign.

The D3R observed a wide range of precipitation types during GCPEx namely: light rain, synoptic snow storm, lake effect snow, freezing rain, freezing drizzle, ice pellets and light snow flurries (Table 7.1). During GCPEX, the radar had a place holder Ka band transmitter while a high power transmitter (40 W), is planned to be installed on the radar during Fall 2012. Some of the important system wide findings of D3R during GCPEx included field verification of the end-to-end system, reconfirmation of system calibration, measurement of echoes weaker than -5 dBZ at Ku band, deployment at extreme climatic conditions and ability to operate in stand-alone mode for extensive hours. The key observations from GCPEx for the Ku-band system are presented as follows.

Before the operations for the GCPEx began, the calibration of the D3R was validated with the King City C-Band radar (WKR). Figure 7.9 shows side-by-side comparisons of the two radars for reflectivity and Doppler velocity products for a rain event on Jan 17, 2012 at Egbert, Ontario. The two radars were scanning in the RHI mode facing each other along their line of sight during this event. The maximum range of the radars is, therefore, set to the distance between the two radars (34.2 km) on these RHIs. Further, the Doppler velocity is reversed for D3R for comparison purposes (since the sign of Doppler is opposite on D3R when compared to the King City Radar, because they are facing each other). The RHIs show a good comparison of D3R with the WKR observations. A light snow event was observed on Jan 26, 2012. The observations of light snow and ice require higher radar sensitivity. Figure 7.10 shows the over-the-head RHI of D3R for this event. It can be seen that the echoes weaker than -5 dBZ were observed in this over-the-head RHI along the King City C-band radar azimuth.

Figure 7.11 shows the D3R observations of the development of a mixed-phase hydrometeor event. The 20-min snapshot of an even faster sampling of the event

Table 7.1: List of diverse meteorological events observed by D3R during GCPEx

Date	**Event**	**Remarks**
Jan 17, 2012	Light rain	Coincident scans with WKR
Jan 19-20, 2012	Lake effect snow storm	Aircraft ops, stronger echoes in Ka band
Jan 23, 2012	Melting layer observations of rain bands	
Jan 24, 2012	Snow flurries and light snow	Ground ops over-night surveillance
Jan 26-27, 2012	Cold rain event: observation of mammatus clouds, brightband formation and freezing rain	Aircraft ops, stronger echoes in Ka band, ice pellets on ground
Jan 28, 2012	Light snow	Over-the-head RHIs
Jan 30, 2012	Light to moderate lake effect snow	Aircraft ops, over-the-head RHIs
Feb 10, 2012	Light synoptic snow with cold front	Convair ops, over-the-head RHIs
Feb 11, 2012	Lake effect snow	Aircraft ops, over-the-head RHIs
Feb 14, 2012	Light snow	Satellite under-flights
Feb 18, 2012	Synoptic snow cyclone	Aircraft ops, over-the-head RHIs, satellite overpasses, stronger echoes in Ka band
Feb 21, 2012	Light to moderate synoptic snow	Aircraft ops, over-the-head RHIs
Feb 24, 2012	Heavy synoptic snow	Aircraft ops, over-the-head RHIs, 14-hour observation of the event covering precipitation types of various phases and rates
Feb 27, 2012	Very light lake effect snow	Coincident scans with WKR in ground ops mode
Feb 29, 2012	Frequent sampling of intense snow bands	Coincident scans with WKR in ground ops mode, stronger echoes in Ka band, freezing drizzle at the end of the event

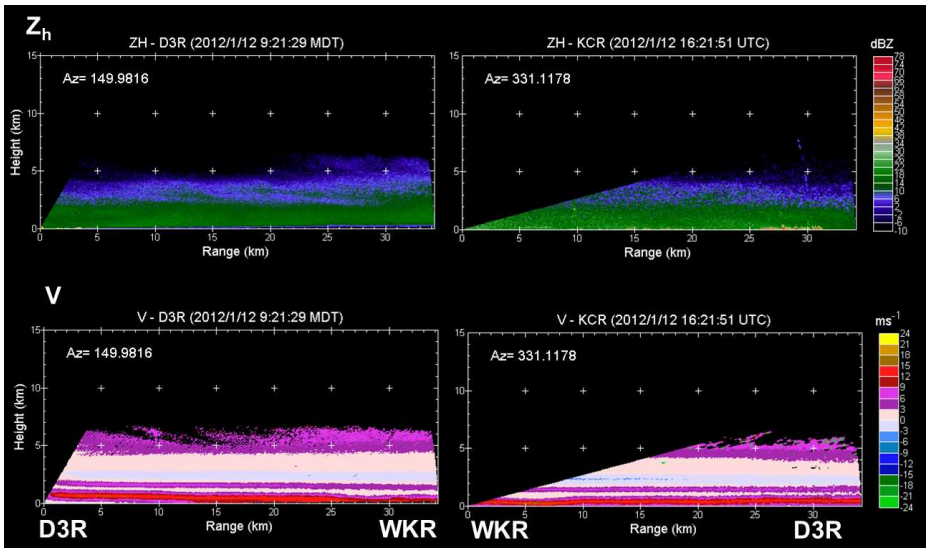

Figure 7.9: D3R observations (left panels) as compared to that of the King City Radar (WKR) (right panels) for a light rain event in Egbert, Ontario (Jan 17, 2012). The top panels are reflectivity and the bottom panels are Doppler velocity. The maximum range in the figures are set to 34.2 km which is equal to the distance between the two radars.

shows the mammatus clouds, the subsequent brightband layer and freezing rain on ground. Figure 7.12 shows low elevation PPI observations of an intense snow band of a synoptic snow cyclone in Egbert on Feb 20, 2012. The radar sampled this event every five minutes as the band approached the radar (Figure 7.13). These observations show the capability of the receiver and signal processor software to detect and compute minute variations of diverse meteorological events.

7.3 Epilogue

The primary purpose of this research was to develop the digital receiver and signal processor for a solid-state transmitter radar to mitigate blind zone and range-velocity ambiguity. The development of the WiBEX and D3R systems was used as an opportunity to develop a general solution and test it in the field deployment of a radar.

The digital receiver was designed for optimizing the on-board resources and imparting high configurability for a research radar. The signal processor for computing

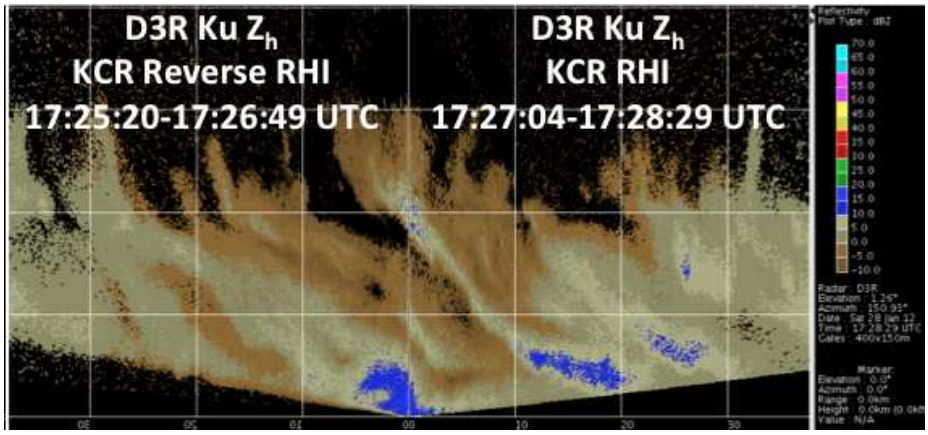

Figure 7.10: Over-the head RHI for a light snow event at Egbert, Ontario (Jan 26 2012) shows echoes as weak as -5 dBZ observed on Ku band.

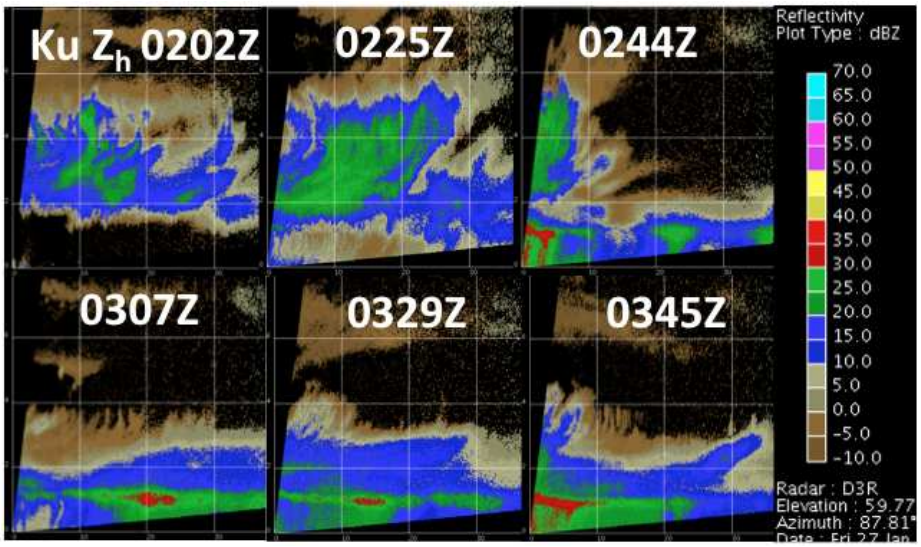

Figure 7.11: Observation of mammatus clouds, brightband formation and freezing rain at the azimuth of 87.8° towards the Skydive site on Jan 26, 2012 at Egbert, Ontario. The snapshots are presented for approximately every 20 minutes from a set of scans at every 10 mins.

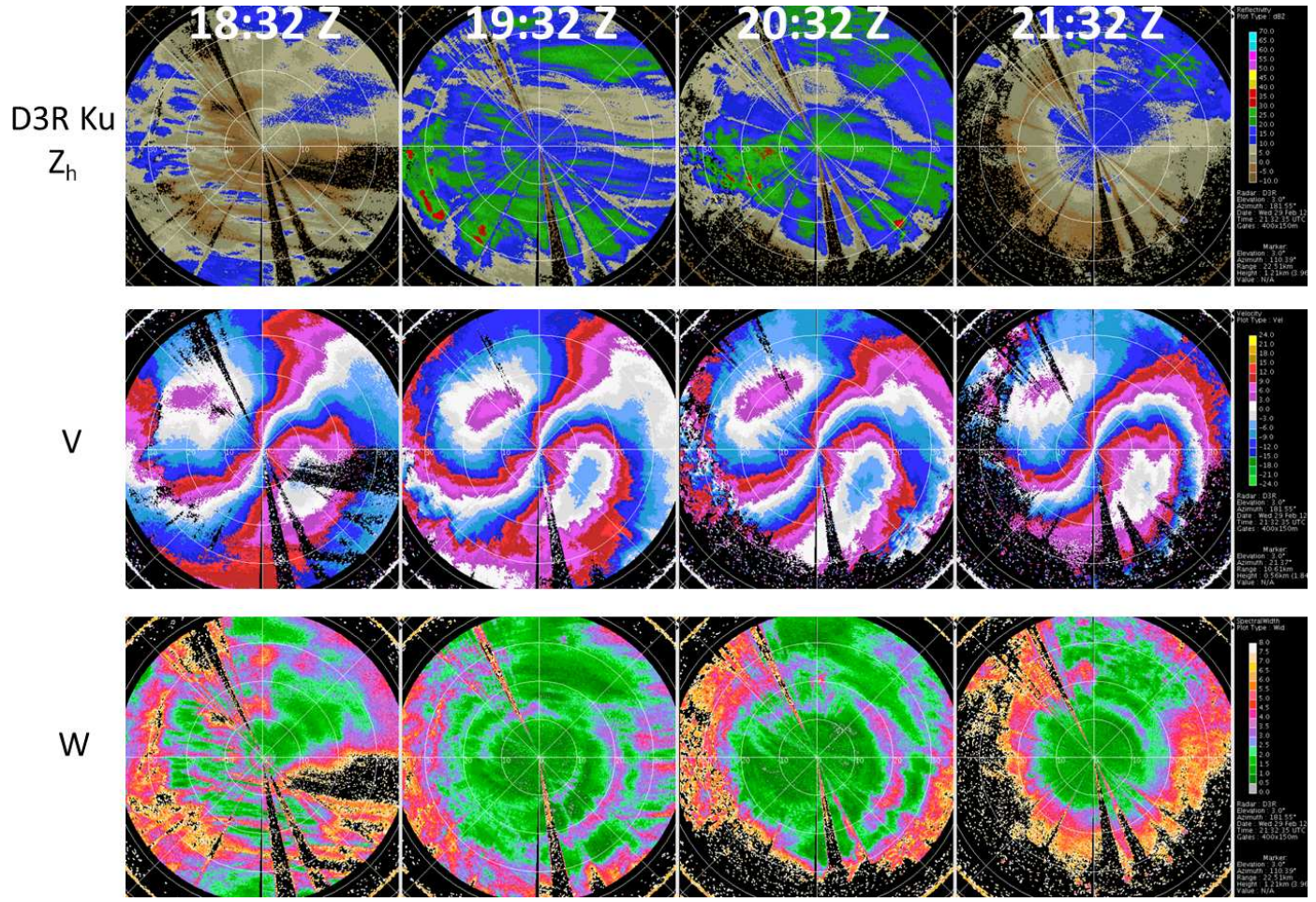

Figure 7.12: The low elevation PPIs of D3R observations of the synoptic snow cylcone in Egbert, Ontario observed on Feb 29, 2012. The one-hour snapshots of the merged profiles of the standard moments show an approaching and receding intense snow band.

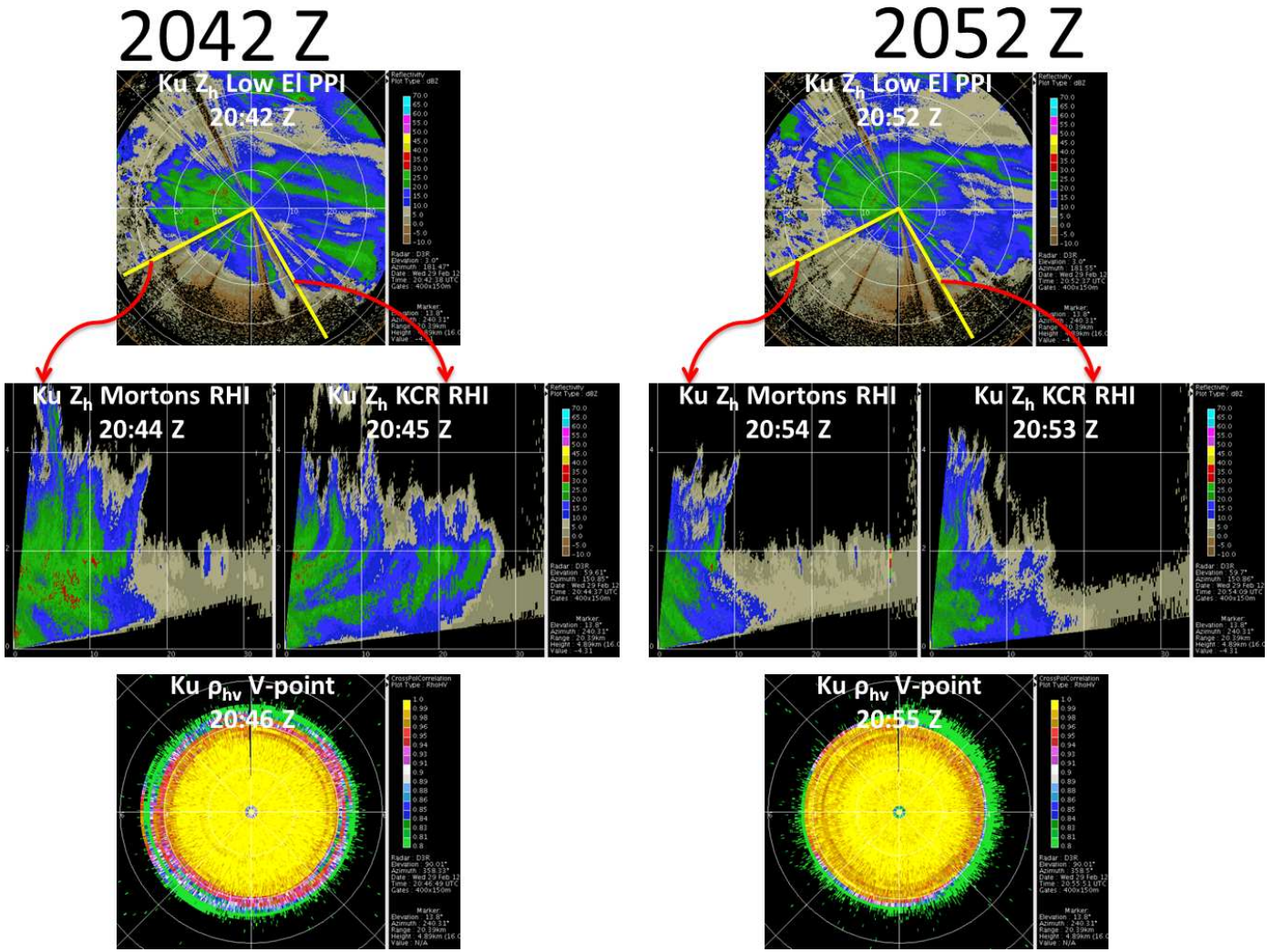

Figure 7.13: The 10-minute snapshots of D3R RHI scans which sampled the intense snow band every five minutes. The copolar correlation coefficient in the vertically pointing scan rises in its range extent as the storm approaches the radar site.

products from the digital receiver outputs was developed and deployed. The digital receiver data has been extensively analyzed and compared with calibrated systems such as CSU-CHILL radar. Several of the programmable options for the receiver were helpful in enhancing the operational and performance benefits of the radar.

Some of the important future work on the signal processor would include development of modules for clutter filter, attenuation correction and computation of science products in real-time. The digital receiver could not be tested for selectable range resolution and real-time change of filter coefficients. The capability of the system to process phase-coded waveforms and compute LDR could not be verified because the corresponding options on the waveform generator software were not yet tested.

This thesis presented a non-commercial option for the frequency-diversity digital receiver which can be tailored for inidividual weather research radars. The development of a complete digital receiver solution for the solid-state transmitter radar would present interesting research opportunities in observing weather events in future.

BIBLIOGRAPHY

Ackerman, T. P. and G. Stokes, 2003: The atmospheric radiation measurement program. *Phys. Today*, **56**, 38–45.

ARA, 2012: Seavey Division Products and Services. http://www.ara-inc.com/1192.xml.

Atlas, D. and C. W. Ulbrich, 1990: Early foundations of the measurement of rainfall by radar. *Radar in Meteorology*, D. Atlas, ed., Amer. Meteor. Soc., 86–97.

Beekhuis, H. and I. Holleman, 2008: From pulse to product, highlights of the digital-IF upgrade of the Dutch national radar network. *Proceedings of the Fifth European Conference on Radar in Meteorology and Hydrology (ERAD 2008)*, Helsinki, Finland.

Bharadwaj, N. and V. Chandrasekar, 2012: Wideband waveform design principles for solid-state weather radars. *J. Atmos. Oceanic Technol.*, **29**, 1431.

Bharadwaj, N., V. Chandrasekar, and F. Junyent, 2010: Signal processing system for the CASA integrated project I. *J. Atmos. Oceanic Technol.*, **27**, 1440–1460.

Bharadwaj, N., K. V. Mishra, and V. Chandrasekar, 2009: Waveform considerations for dual-polarization Doppler weather radar with solid-state transmitters. *Proceedings of IGARSS*, Cape Town, South Africa, III–267 – III–270.

Bidwell, S. W., J. F. Durning, D. F. Everett, M. R. Schwaller, E. A. Smith, and D. B. Wolff, 2004: Preparations for Global Precipitation Measurement (GPM) ground validation. *Proceedings of IGARSS*, Anchorage, Alaska, II–921 – II–924.

Bringi, V. N. and V. Chandrasekar, 2001: *Polarimetric Doppler Weather Radar: Principles and Applications*. Cambridge University Press.

Bringi, V. N. and A. Hendry, 1990: Technology of polarization diversity radars for meteorology. *Radar in Meteorology*, D. Atlas, ed., Amer. Meteor. Soc., 153–190.

Brunkow, D., V. N. Bringi, P. C. Kennedy, S. A. Rutledge, V. Chandrasekar, E. A. Mueller, and R. K. Bowie, 2000: A description of the CSU-CHILL national radar facility. *J. Atmos. Oceanic Technol.*, **17**, 1596–1608.

CCT, 2012: Concurrent Technologies. http://www.gocct.com.

Chandrasekar, V. and N. Bharadwaj, 2009: Orthogonal channel coding for simultaneous co and cross-polarization measurements. *J. Atmos. Oceanic Technol.*, **26**, 45–56.

— 2010: Waveform concepts and design for weather radar network. *Principles of waveform diversity and design*, M. Wicks, E. Mokole, S. Blunt, R. Schneible, and V. Amuso, eds., Scitech Publishing, Inc., 357–393.

Chandrasekar, V., A. Hou, E. Smith, V. N. Bringi, S. A. Rutledge, E. Gorgucci, W. A. Peterson, and G. Skofronick-Jackson, 2008: Use of dual polarization radar in validation of satellite precipitation measurements: Rationale and opportunities. *Bulletin of the American Meteorological Society*, **89**, 1127–1145.

Chandrasekar, V. and A. P. Jayasumana, 2001: Radar design and management in a networked environment. *Proceedings of ITCOMM*, Denver CO, 142–147.

Chandrasekar, V. and R. J. Keeler, 1993: Antenna pattern analysis and measurements for multiparameter radars. *J. Atmos. Oceanic Technol.*, **10**, 674–683.

Chandrasekar, V., C. M. Nguyen, and N. Bharadwaj, October 2010: Sensitivity enhancement system. US Patent 2011/0102250 A1, Colorado State University.

Chandrasekar, V. and B. Philips, 2012: The Dallas Fort Worth urban remote sensing network. *Proceedings of IGARSS*, Munich, Germany, CDROM.

Chandrasekar, V., M. Schwaller, M. Vega, J. Carswell, K. V. Mishra, R. Meneghini, and C. Nguyen, 2010: Scientific and engineering overview of the NASA Dual-frequency Dual-polarized Doppler Radar (D3R) system for GPM ground validation. *Proceedings of IGARSS*, Honolulu, Hawaii, 1308–1311.

Chandrasekar, V., M. Schwaller, M. Vega, J. Carswell, K. V. Mishra, A. Steinberg, N. C., M. Le, J. Hardin, F. Junyent, and J. George, 2012: Dual-frequency Dual-polarized Doppler Radar (D3R) system for GPM ground validation: Update and recent field observations. *Proceedings of IGARSS*, Munich, Germany, CDROM, [To Appear].

Cho, J. and M. Weber, 2010: Terminal Doppler Weather Radar enhancements. *Proceedings of IEEE International Radar Conference*, Washington DC, 1245–1249.

Cifelli, R. and V. Chandrasekar, 2010: Dual-polarization radar rainfall estimation. *Rainfall: State of the science*, F. Y. Testik and M. Gebremichael, eds., American Geophysical Union, 105–126.

Cloude, S. R., 2010: *Polarization: Applications In Remote Sensing*. Oxford University Press.

Doviak, R. J. and D. S. Zrnić, 1993: *Doppler Radar and Weather Observations*. Dover Publications, Inc.

Doyle, Sir A. C., 1986: The sign of four. *Sherlock Holmes: The Complete Novels and Stories, Volume I*, Bantam Classics.

ELDES, 2012: NDRX digital receiver and signal processor brochure. http://www.eldesradar.com/file/brochure%5Fndrx-2.pdf.

Ettus, 2012: Ettus Research - Products. https://www.ettus.com/product.

Fjørtoft, R. and A. Lopès, 2001: Estimation of the mean radar reflectivity from a finite number of correlated samples. *IEEE Trans. Geos.*, **39**, 196–199.

Francesc, J., V. Chandrasekar, D. McLaughlin, E. Insanic, and N. Bharadwaj, 2010: The CASA Integrated Project 1 networked radar system. *J. Atmos. Oceanic Technol.*, **37**, 61–78.

Frush, C., R. Doviak, M. Sachidananda, and D. Zrnić, 2002: Application of the sz phase code to mitigate rangevelocity ambiguities in weather radars. *J. Atmos. Oceanic Technol.*, **19**, 41343.

Galassi, M., J. Davie, J. Theiler, B. Gough, G. Jungman, P. Alken, M. Booth, and F. Rossi, April 29 2011: GNU Scientific Library. Reference Manual 1.15, The GSL Team.

Galati, G., 1993: *Advanced Radar Techniques and Systems (IEE Radar, Sonar, Navigation and Avionics, No 4)*. Peter Peregrines Ltd.

GAMIC, 2012: Welcome to GAMIC. http://www.gamic.com.

GAMIC mbH, July 29 2011: GAMIC services the meteorological weather radar market since 1988. Press Release, GAMIC mbH, Aachen, Germany.

Gematronik, 2012: GDRX digital receiver and signal processor. http://www.gematronik.com/products/radar-components/gdrx/.

George, J., 2007: *Digital transmitter and receiver for CSU-CHILL*. Master's thesis, Colorado State University.

George, J., N. Bharadwaj, and V. Chandrasekar, 2008: Considerations in pulse compression design for weather radars. *Proceedings of IGARSS*, Boston, MA, 109111.

George, J., K. V. Mishra, C. Nguyen, and V. Chandrasekar, 2010: Implementation of blind zone and range-velocity ambiguity mitigation for solid-state weather radar. *Proceedings of IEEE International Radar Conference*, Washington DC, 1097–5659.

GNU Radio, 2012: gnuradio.org. http://gnuradio.org/redmine/.

Gorgucci, E., V. Chandrasekar, V. N. Bringi, and G. Scarchilli, 2002: Estimation of raindrop size distribution parameters from polarimetric radar measurements. *J. Atmos. Sci.*, **59**, 2373–2384.

GTK Display, 2012: Real-time Display. http://www.chill.colostate.edu/w/Real-time%5FDisplay.

Hendry, A. and Y. M. M. Antar, 1984: Precipitation particle identification with centimeter wavelength dual-polarization radars. *Radio Sci.*, **19**, 115–122.

Heymsfield, G. M., J. R. Carswell, L. Li, D. Schaubert, and J. Creticos, 2006: Development of the High-altitude Imaging Wind and Rain Airborne Profiler (HIWRAP). *Eos Trans. AGU, 87(52), Fall Meet. Suppl., Abstract IN21A-1202*, San Francisco, CA.

Hogenauer, E., 1981: An economical class of digital filters for decimation and interpolation. *IEEE Transactions on Acoustics, Speech, and Signal Processing*, **ASSP-29**, 155–162.

Hubbert, J. C., M. Dixon, and S. M. Ellis, 2009: Weather radar ground clutter. part ii: Real-time identification and filtering. *J. Atmos. Oceanic Technol.*, **26**, 11811197.

Iguchi, T., H. Hanado, N. Takahashi, S. Kobayashi, and S. Satoh, 2003: The Dual frequency Precipitation radar for the GPM core satellite. *Proceedings of IGARSS*, Toulouse, France, III–1698 – III–1700.

Iguchi, T., T. Kozu, R. Meneghini, J. Awaka, and K. Okamoto, 2010: Rain-profiling algorithm for the trmm precipitation radar. *J. App. Met.*, **39**, 2038–2052.

Jarrott, K., C. Barnes, R. Jones, F. Cummings, L. McBean, M. Whitehead, R. Webb, T. Keenan, P. May, C. Brown, and B. J., 2007: Implementation of the RNDSUP S-band Doppler radar systems for use in the Australian weather radar network. *33rd Conf. on Radar Meteorology*, Amer. Meteor. Soc., Cairns, Queensland.

Jensen, M. P., W. A. Petersen, A. D. Del Genio, S. E. Giangrande, A. Heymsfield, G. Heymsfield, A. Y. Hou, P. Kollias, B. Orr, S. A. Rutledge, M. R. Schwaller, and E. Zipser, April 2010: Midlatitude Continental Convective Clouds Experiment (MC3E). DOE/SC-ARM/10-004, US Department of Energy ARM Climate Research Facility.

Junyent, F., V. Chandrasekar, and N. Bharadwaj, 2009: Uncertainties in phase and frequency estimation with a magnetron radar: implication for clear air measurements. *Proceedings of IGARSS*, Capetown, South Africa, III–613–616.

Keeler, R. J. and R. E. Passarelli, May 1989: Signal processing for atmospheric radars. NCAR Technical Note-331, National Center for Atmospheric Research, Boulder, Colorado.

Khasgiwale, R., 2005: *Reconfigurable Data Acquisition System For Weather Radar Applications*. Master's thesis, University of Massachusetts Amherst.

Klazura, G. E. and D. E. Imy, 1993: A description of the initial set of analysis products available from the NEXRAD WSR-88D system. *Bull. Amer. Meteorol. Soc.*, **74**, 1292–1311.

Kollias, P., E. E. Clothiaux, M. A. Miller, B. A. Albrecht, G. L. Stephens, T. P. Ackerman, and D. E. Imy, 2007: Millimeter-wavelength radars: New frontier in atmospheric cloud and precipitation research. *Bull. Amer. Meteorol. Soc.*, **88**, 16081624.

Kraus, J. D. and R. J. Marhefka, 2002: *Antennas for All Applications*. McGraw-Hill, third edition.

Kummerow, C., J. Simpson, O. Thiele, W. Barnes, A. T. C. Chang, E. Stocker, R. F. Adler, A. Hou, R. Kakar, F. Wentz, P. Ashcroft, T. Kozu, Y. Hong, K. Okamoto, T. Iguchi, H. Kuroiwa, E. Im, Z. Haddad, G. Huffman, B. Ferrier, W. S. Olson, E. Zipser, E. A. Smith, T. T. Wilheit, G. North, T. Krishnamurti, and K. Nakamura, 2000: The status of the tropical rainfall measuring mission (trmm) after two years in orbit. *J. App. Met.*, **39**, 1965–1982.

Le, M., V. Chandrasekar, and S. Lim, 2009: Combined Ku and Ka band observations of precipitation and retrievals for GPM ground validation. *Proceedings of IGARSS*, Cape Town, South Africa, I–208 – I–211.

Lee, J.-S. and E. Pottier, 2009: *Polarimetric Radar Imaging: From Basics to Applications*. CRC Press, first edition.

Lewis, B. L., F. F. Kretschmer, Jr., and W. W. Shelton, 1986: *Aspects of Radar SIgnal Processing*. Artech House, Inc.

Lhermitte, R., 1987: A 94 GHz Doppler radar for clouds observations. *J. Atmos. Oceanic Technol.*, **4**, 36–48.

Malkomes, M., M. Toussaint, and D. Veerkamp, 2008: Limiting factors of magnetron radar stability, how to improve clutter suppression by improved receiver phase stability and precise burst measurement, a transmitter coherent Klystron is really the only way? *Proceedings of the Fifth European Conference on Radar in Meteorology and Hydrology (ERAD 2008)*, Helsinki, Finland.

Mishra, K. V., V. Chandrasekar, N. C., and M. Vega, 2012: The signal processor system for the solid-state NASA Dual-frequency Dual-polarized Doppler Radar. *Proceedings of IGARSS*, Munich, Germany, CDROM, [To Appear].

Mishra, K. V., V. Chandrasekar, C. Nguyen, and M. Vega, 2011: Waveform design and implementation for the solid-state NASA Dual-frequency Dual-polarized Doppler Radar. *Proceedings of IGARSS*, Vancouver, Canada, CDROM.

Mudukutore, A. S., V. Chandrasekar, and R. J. Keeler, 1998: Pulse compression for weather radars. *IEEE Trans. Geoscience and Remote Sensing.*, **36**, 125–142.

Mueller, E. A. and E. J. Silha, 1978: Uniques features of the CHILL radar system. *18th Conf. on Radar Meteorology*, Amer. Meteor. Soc., Atlanta, Georgia, 381–382.

Munin, 2012: Munin - Trac. http://munin-monitoring.org/.

Nathanson, F. E., 1969: *Radar Design Principles*. McGraw-Hill.

Nguyen, C., V. Chandrasekar, K. V. Mishra, and J. George, 2011: Sensitivity enhancement system for pulse compression weather radar. *35th Conf. on Radar Meteorology*, Amer. Meteor. Soc., Pittsburgh, Pennsylvania.

Nguyen, C. M. and V. Chandrasekar, 2009: Time domain GMAP clutter filter for weather radars. *34th Conf. on Radar Meteorology*, Amer. Meteor. Soc., Williamsburg, Virginia.

Nguyen, C. M., D. N. Moisseev, and V. Chandrasekar, 2008: A parametric time domain method for spectral moment estimation and clutter mitigation for weather radars. *J. Atmos. Oceanic Technol.*, **25**, 83–92.

Oliver, C. J., 1979: Pulse compression in optical radar. *IEEE Trans. Aerosp. Electron. Syst.*, **15**, 306–324.

Orbital Systems, 2012: Antenna Positioners. http://www.orbitalsystems.com/antenna%5Fpositioners.

Pace, P. E., 2000: *Advanced Techniques For Digital Receivers*. Artech House.

Papoulis, A. and S. U. Pillai, 2002: *Probability, Random Variables and Stochastic Processes*. McGraw-Hill, fourth edition.

Patton, L. K., 2007: *A GNU Radio Based Software-Dened Radar*. Master's thesis, Wright State University.

Peebles, P. Z., 1998: *Radar Principles*. Wiley-Interscience.

Pentek, 2012: Pentek, Inc. - Pentek Home. http://www.pentek.com/.

Prabaswara, A., A. Munir, and A. B. Suksmono, 2011: GNU radio based software-defined FMCW radar for weather surveillance application. *Proceedings of the Sixth International Conference on Telecommunication Systems, Services, and Applications 2011*, Bali, Indonesia, 227–230.

Probert-Jones, J. R., 1962: The radar equation in meteorology. *Quart. J. Roy. Meteor. Soc.*, **88**, 485–495.

Radtec, 2012: Radtec Engineering.

Raymond, E. S., 2012: GPSd - Put your GPS on the net! http://catb.org/gpsd/.

Rew, R., G. Davis, S. Emmerson, H. Davies, E. Hartnett, and D. Heimbigner, June 2011: The NetCDF Users Guide. NetCDF Version 4.1.3, University Corporation for Atmospheric Research, Boulder, CO.

RSS, 2012: Welcome. http://www.remotesensingsolutions.com/.

Scherier, P. J. and L. L. Scharf, 2010: *Statistical Signal Processing of Complex-Valued Data: The Theory of Improper and Noncircular Signals*. Cambridge University Press.

Schwaller, M., Oct 21, 2009: Ground validation system level-3 requirements for a deployable ka-ku-band radar. Technical report, NASA Goddard Space Flight Center, Greenbelt, MD.

Seliga, T. A. and V. N. Bringi, 1976: Potential use of radar differential reflectivity measurements at orthogonal polarizations for measuring precipitation. *J. App. Meteorol.*, **15**, 69–76.

— 1978: Preliminary results of differential reflectivity measurements in rain. *18th Conf. on Radar Meteorology*, Amer. Meteor. Soc., Atlanta, Georgia, 134–138.

Seliga, T. A., V. N. Bringi, and H. H. Al-Khatib, 1979: Differential reflectivity measurements in rain: First experiments. *IEEE Trans. Geosci. Electron.*, **17**, 240–244.

Seliga, T. A., R. G. Humphries, and J. I. Metcalf, 1990: Polarization diversity in radar meteorology: Early developments. *Radar in Meteorology*, D. Atlas, ed., Amer. Meteor. Soc., 109–121.

Siggia, A. and J. Passarelli, 2004: Gaussian model adaptive processing (GMAP) for improved ground clutter cancellation and moment calculation. *European Conference on Radar in Meteorology and Hydrology*, ERAD., 67–73.

Skofronick-Jackson, G., W. A. Petersen, D. Hudak, and M. R. Schwaller, Sep 2011: GPM Cold-season Precipitation Experiment (GCPEx) Science Plan. http://pmm.nasa.gov/sites/default/files/document%5Ffiles/GCPEx%5Fscience%5Fplan%5FCURRENT.pdf.

Skolnik, M. I., 1990: *Radar Handbook*. McGraw-Hill Professional, second edition.

Stephens, G. L., 2003: The useful pursuit of shadows. *American Scientist*, **91**, 442–449.

Technobox, 2012: PMC, XMC, PCI Express, PCIe, adapter, PCI-e, carrier, FPGA, FPGA-based, configurable, programmable, modular, custom, Ethernet, SCSI, Serial, PMC Module, embedded io, VME, cPCI, Development Tools, I_ O, IEEE 1386.1, VITA 42, Technobox PMC Cards, PCI Mezzanine Card products. http://www.technobox.com/.

TI, Oct 2008: ADS5485 16-Bit, 170/200-MSPS Analog-to-Digital Converters. Product datasheet, Texas Instruments, Inc.

Torres, S. M. and D. S. Zrnic, 1999: Ground clutter canceling with a regression filter. *J. Atmos. Oceanic Technol.*, **16**, 1364–1372.

Tragl, K., 1990: Polarimetric radar backscattering from reciprocal random targets. *IEEE Trans. Geoscience and Remote Sensing.*, **8**, 856–864.

Tsui, J., 2001: *Digital Techniques for Wideband Receivers*. Artech House Publishers, second edition.

Tsui, J. B. Y., 2009: *Special Design Topics in Digital Wideband Receivers*. Artech House Publishers, first edition.

Ulbrich, C. W. and D. Atlas, 1975: The use of radar reflectivity and microwave attenuation to obtain improved measurements of precipitation parameters. *16th Conf. on Radar Meteorology*, Amer. Meteor. Soc., Houston, Texas, 496–503.

Vaidyanathan, P. P., 1993: *Multirate Systems and Filter Banks*. Prentice-Hall.

Vaisala Inc., Sept 2009: RVP900 digital receiver and signal processor user's manual. Technical report, Vaisala Oyj, Helsinki, Finland.

Vierinen, J., L. Zhou, M. S. Lehtinen, and I. Virtanen, 3-7 August 2009: USRP2 based software defined radar receiver. *14th EISCAT International Workshop*, Tromso, Norway.

Xilinx Inc., Feb 6, 2009: Virtex-5 family overview. DS100 (v5.0) product specification datasheet, Xilinx Inc.

Yoshikawa, E., T. Ushio, Z. Kawasaki, T. Mega, S. Yoshida, T. Morimoto, K. Imai, and S. Nagayama, 2010: Development and initial observation of high-resolution volume-scanning radar for meteorological application. *IEEE Trans. Geoscience and Remote Sensing.*, **48**, 3225–3235.

Zrnić, D. and P. Mahapatra, 1985: Two methods of ambiguity resolution in pulsed Doppler weather radars. *IEEE Trans. Aerosp. Electr. Syst.*, **21**, 470–483.